A Laboratory Study of the Friction Behavior of Granular Materials

by

Kevin M. Frye

M.S. Geophysics
Boston College, 1997

S.B. Earth Atmospheric and Planetary Sciences
Massachusetts Institute of Technology, 1995

Submitted to the Department of Earth, Atmospheric and Planetary Sciences

in partial fulfillment of the requirements for the degree of

Doctor of Philosophy in Geophysics

at the

MASSACHUSETTS INSTITUTE OF TECHNOLOGY

September 2002

Author:_____
Department of Earth, Atmospheric, and Planetary Sciences
August 5, 2002

Certified by:_____
Chris Marone
Visiting Professor of Geophysics
Thesis Supervisor

Accepted by:_____
Ronald Prinn
Department Head

A Laboratory Study of the Friction Behavior of Granular Materials
by
Kevin M. Frye

Submitted to the Department of Earth, Atmospheric and Planetary Sciences
in partial fulfillment of the requirements for the degree of
Doctor of Philosophy

Professor Chris Marone, Thesis Supervisor

Abstract

I report on laboratory experiments designed to investigate the microphysical processes that result in rate- and state-dependent friction behavior and experiments designed to match the boundary conditions used by numerical models of granular friction. The effect of relative humidity (RH from <5% to 100%) is investigated with velocity stepping tests (10-20 μm/s) and slide-hold-slide (SHS) tests (3-1000 s) on 3 mm thick layers of quartz powder, alumina powder, Westerly granite powder, and Westerly granite blocks sheared at 25 MPa normal stress. Powders are conditioned in situ under controlled RH to create new surface area before shearing. A transition from velocity-strengthening to velocity-weakening frictional behavior occurs as RH increases. Frictional healing is negligible at low humidity and increases with increasing RH for both materials. While the coefficient of sliding friction for powders is independent of humidity, bare surface data indicate that sliding friction decreases with increased RH. Normal stress vibrations in SHS tests can add compaction induced granular strengthening, but for constant normal force tests, chemically assisted healing mechanisms control the friction behavior. The chemically assisted contact junction processes can be reduced or turned off at low humidity at room temperature in quartz and alumina. Velocity stepping tests and SHS tests are also performed at different values of applied normal stress (5 to 45 MPa) after pre-conditioning at high normal stress (40 and 35 MPa) for powders and no pre-conditioning for bare surfaces. Time-dependent frictional healing decreases with increasing normal stress. For the powders, velocity stepping tests require the use of a 2 state variable model to accurately retrieve rate- and state-friction parameters. The complex velocity dependent behavior may be a result of over-compaction in the granular layers during preconditioning.

Numerical models of granular shear show lower friction and a greater tendency for stick slip than laboratory studies designed to investigate fault mechanics. Chapters 4 and 5 detail laboratory experiments designed to reproduce the conditions of numerical models and test the role that grain characteristics play in controlling frictional behavior. Friction and microstructural data are compared for direct shear experiments on thin layers (2-3 mm) of angular quartz sand and spherical glass beads. We study the effect of grain shape, roughness, size distribution, comminution, and particle dimensionality. In a non-fracture loading regime, sliding friction for smooth spherical particles ($\mu \sim 0.45$) is measurably lower than for angular particles ($\mu \sim 0.6$). A narrow particle size distribution (PSD) of spherical beads (105-149 μm) exhibits unstable stick-slip behavior, whereas a wide PSD of spheres (1-800 μm) and the angular gouge display stable sliding. At higher stress, where grain fracture is promoted, initially spherical particles become stable with accumulated slip and friction increases to the level observed for angular gouge. Quartz glass rods are sheared in 1-D and 2-D configurations and I compare the results to previously published numerical models and to the friction behavior of angular gouge. The

laboratory 2-D data and numerical model results agree well: both exhibit a coefficient of friction of ~0.3 and changes in sliding friction that correlate with layer thickness change. Friction fluctuates over displacements on the order of particle diameter, and these fluctuations are much greater than the strengthening observed after slide-hold-slide tests. The data indicate that friction scales with dimensionality for smooth particles that do not break. Frictional strength and stability of a granular shear zone are sensitive to grain shape, dimensionality, PSD, and the evolution of shear localization. The results show that the first order disparities between laboratory and numerical studies of granular shear can be explained by differences in grain characteristics and loading conditions. Since natural faults predominantly contain angular gouge we find no evidence for a fault weakening mechanism associated with the presence of gouge.

Biographical Note

Kevin Michael Frye was born in Portsmouth, NH on March 11, 1972. After graduating from Marshwood High School in Eliot, ME, he attended MIT where he graduated with an S.B. in Earth, Atmospheric, and Planetary Sciences in 1995. Kevin received a M.S. degree from Boston College in 1997 with a thesis titled: "The effect of pore fluid chemistry on the spectral induced polarization response of Berea sandstone." He is currently a geoscientist for Shell Exploration and Production in New Orleans, LA.

Publications include:

Lesmes, D.P., and **K. M. Frye**, Influence of pore fluid chemistry on the complex conductivity and induced polarization responses of Berea Sandstone, *Journal of Geophysical Research*, 106, 4079-4090, 2001.

Built and calibrated test device; performed experiments; paper based on Master's thesis.

Saffer, D.M., **K.M. Frye**, C. Marone, and K. Mair, Laboratory results indicating complex and potentially unstable frictional behavior of smectite clay, *Geophysical Research Letters*, 28, 2297-2300, 2001.

Assisted Dr. Saffer in performing pilot tests; performed the suite of experiments whose data were used in the paper; reduced data and assisted in interpretation.

Mair, K., **K.M. Frye**, and C. Marone, Influence of grain characteristics on the friction of granular shear zones, *Journal of Geophysical Research,* in press, 2002.

Appears in this dissertation as chapter 4. Performed pilot tests with glass beads for "2.800—Tribology" term project. Carried out further experiments with Dr. Mair; reduced and interpreted data with Dr. Mair; mixed wide particle size distribution bead samples; took photomicrographs of bead samples; assisted in writing and editing of text.

Frye, K. M., and C. Marone, The effect of humidity on granular friction at room temperature, *Journal of Geophysical Research*, in press, 2002.

Appears in this dissertation (C. Marone, advisor) as chapter 2.

Frye, K. M., and C. Marone, The effect of particle dimensionality on granular friction, *Geophysical Research Letters*, in press, 2002.

Appears in this dissertation as chapter 5.

Acknowledgments

The acknowledgment section of a dissertation is too short to contain all the praise and thanks deserved by all the people who have helped me in my graduate career. I hope that the people listed here with a few lines following realize how much they have meant to me.

I owe a lot to my advisor, Chris Marone—he has been patient, encouraging, and insightful. I feel fortunate to have worked in his labs and I'm grateful he gave me the chance to work with him.

I also offer my sincere thanks to the MIT members of my thesis committee, Brian Evans, Dale Morgan, and Wiki Royden. I've taken classes taught by all three, roped Dale and Brian into being on my general exam committee, and worked with Wiki as a teaching assistant for an Introductory Geophysics class, so they've all put their mark on me and my work. I appreciate their time and effort.

I'd like to thank David Lesmes for honing my laboratory skills at Boston College. David always has relevant comments, regardless of the research topic, and I've enjoyed our conversations greatly. Julia Morgan (Rice University) has also been a great source of insight, especially in the subject matter presented in Chapters 3 and 4. I am pleased to be able to include her numerical simulations for comparison to my data. Jim Rice (Harvard University) and Terry Tullis (Brown University) greatly improved the manuscript of chapter 1 (specifically) through the publication review process and other chapters (generally) through conversations at conferences. I was especially pleased to have Terry Tullis as a member of my thesis committee.

Karen Mair and Steve Karner served as mentors, coworkers, and friends during my early years in the lab. Thanks for all of your help, advice, and know-how. I also received help and fellowship from the people in the high-temperature rock mechanics lab and visitors to our lab: Margaret Boettcher, Brian Evans, Jock Hirst, Greg Hirth, Tiancong Hong, Uli Mok, Joerg Renner, Eliza Richarson, Demian Saffer, and Xiaohui Xiao. Thanks for making the lab a fun place to work.

I would like to recognize the assistance and friendship of my fellow graduate students in the department, from floor 12 down: Lindy Elkins Tanton, Jim Van Orman, Steve Singletary, Steve Parman, Karen Viskupic, Julie Baldwin, Jenny and Eric Matzel, Marin Clark, Simon Brocklehurst, Brian deMartin, Brendan Meade, Eric Hetland, Jeff Maguire, Frederik Simons and Hrafnkell Karason.

I've had the good fortune of being a part of a supportive family. I received a lot of free meals and moral support from David and Joanne Frye as well as Jeff and Robin Pitcairn. I'd also like to thank a group of friends who have made living in the Boston area a fun experience for the last few years: Jay and Laura Coulson, Christian and Kate Hamer, MIT rugby football club, and my roommates—Mike Braun, Oscar Pizarro, Jerry Hughes, Bryan Morrissey, and Ed Sprague (despite his piscicidal tendencies). Finally, meeting Maureen Long and her family has been one of the most rewarding experiences of my years at MIT.

Table of Contents

List of Figures

List of Tables

1. Introduction

Active faults exhibit a variety of behaviors from stable creep to stick-slip motion. How shearing is accommodated along a fault is determined by the velocity-, slip-, and time-dependence of the frictional strength, which can be described by rate- and state-dependent friction laws. Although the empirical rate- and state-dependent laws have been applied successfully to many types of laboratory data and field observations [see *Marone*, 1998, and *Scholz*, 1998 for reviews], the physical mechanisms responsible for the friction behaviors they describe remain poorly understood.

Static friction, the ratio of shear stress to normal stress necessary for two surfaces to begin sliding, generally increases linearly with the logarithm of time that the surfaces are in stationary contact (hold time). On bare surfaces, normal and shear loads are supported by a population of asperities [*Rabinowicz*, 1951], such that the real area of contact between two surfaces is only a small fraction of the apparent area of contact. Frictional interfaces strengthen with time, as contact junctions either increase in area through asperity deformation [e.g., *Dieterich and Kilgore*, 1994; 1996] or undergo an increase in bond strength between the surfaces [*Rice*, 1976; *Hirth and Rice*, 1980; *Michalske and Fuller*, 1985].

What are the contact junction strengthening mechanisms operative in laboratory friction studies? Many studies have documented the dramatic effect the presence of water has on the mechanical properties of quartz [*Blacic and Christie,* 1984; *Jaoul et al.,* 1984; *Mainprice and Paterson,* 1984; *Kronenberg and Tullis,* 1984; *Evans and Kohlstedt,* 1995], and the work of *Dieterich and Conrad* [1984] demonstrates the importance of water in determining friction behavior of quartzite blocks. I build on this previous work by documenting the effect of humidity on the friction behavior of granular quartz, alumina, and Westerly granite (chapters 2

and 3). I focus on the fundamental observations on which rate- and state-dependent friction laws are based: velocity dependence of steady-state sliding friction and time dependence of static friction [*Dieterich*, 1972, 1978, 1979; *Ruina*, 1983; *Tullis and Weeks*, 1986; *Chester*, 1994; *Beeler et al.*, 1994; *Marone*, 1998]. By documenting the chemically assisted strengthening and its normal stress dependence, I better characterize the contact junction healing mechanisms.

Although faults are often thought of as two bare surfaces, natural and laboratory faults develop a zone of granular material, or fault gouge, with displacement [*Sammis et al.*, 1986; *Wong et al.*, 1992]. Friction behavior of granular shear zones is influenced by the development of shear fabric and the localization of strain rate onto these shear planes [*Logan et al.*, 1979, *Yund et al.*, 1990, *Mair and Marone*, 1999]. Further, in response to loading perturbations, granular layers compact and dilate much more than bare surfaces, and the density changes within the layer may affect the frictional strength of the material [*Mead*, 1925; *Bishop*, 1954; *Marone and Kilgore*, 1993; *Segall and Rice*, 1995; *Mair and Marone*, 1999; *Losert et al.*, 2000].

The time- and velocity-dependent frictional strength of granular shear zones is likely controlled by both asperity-scale contact junction strengthening and layer compaction/dilation. Do these mechanisms operate independently? What is the relative importance of each in determining the friction behavior of granular materials at room temperature? By controlling humidity and using normal force vibrations, I manipulate the relative contributions of contact junction mechanisms and granular layer densification to the healing signal. In this manner, the relative contribution of each healing mechanism can be assessed (chapter 2).

Ideally, laboratory experiments would identify the fundamental, crystal lattice-scale and meso-scale mechanisms of friction under the range of geological conditions relevant to the seismic cycle. However, our present understanding of fault material properties together with

technical limitations in the laboratory do not allow that level of generality. Thus, an important tool in scaling laboratory friction behavior to natural fault zones is the numerical model. Models that use rate- and state-dependent friction are effective at reproducing the behavior of earthquake faults [e.g., *Rice et al.*, 2001; see *Marone*, 1998 for other examples]. However, discrete element and finite element models of granular friction behavior produce data quite different from laboratory observations of friction [*Mora and Place*, 1998; 1999; *Aharonov and Sparks*, 1999; *Morgan and Boettcher*, 1999; *Morgan*, 1999]. While laboratory measurements of sliding friction for sand are ~0.6, sliding friction is as low as 0.3 in numerical models. The low friction values from numerical models are sometimes used to attribute the inferred weakness of some crustal faults to the presence of fault gouge [*Mora and Place*, 1998; 1999]. The discrepancy between numerical model and laboratory observations may be attributable to the different initial and boundary conditions. Because of computational limitations, numerical models of granular friction often rely on several simplifying boundary conditions, such as smooth, round, 2-dimensional, non-breaking particles. To investigate the effect of these conditions on friction, I study the friction of smooth, round, non-breaking spheres (chapter 4) and investigate the effect of particle dimensionality by simulating 2D conditions with glass and pasta rods (chapter 5).

This dissertation is not meant to be a study of friction under geologic conditions. Relative humidity is likely 100% in the seismogenic zone; fault gouge consists of rough, 3D particles. By performing these experiments, I hope to provide insight into the behavior of crustal faults by isolating healing mechanisms operative at room temperature and analyzing boundary conditions used by modelers of granular shear. For example, observations that have led to debate over the strength of the San Andreas fault zone [*Lachenbruch and Sass*, 1980; *Scholz*, 1996; *Zoback*, 2000] suggest that there may be a mechanism by which friction is lowered and the fault is

weakened. The results documented in this dissertation suggest that rather than some weakening intrinsic to the presence of gouge, researchers should investigate contact junction processes, specifically the surface/interface chemistry of silicates at geologically relevant temperatures and pressures. [e.g., *Goldsby and Tullis*, 1999].

References for chapter 1

Beeler, N. M., T. E. Tullis, and J. D. Weeks, The roles of time and displacement in evolution effect in rock friction, *Geophys. Res. Lett.*, *21*, 1987-1990, 1994.

Bishop, A.W., Correspondence, *Geotech. 4*, 43-45, 1954.

Blacic, J. D., and J. M. Christie, Plasticity and hydrolytic weakening of quartz single crystals, *J. Geophys. Res.*, *89*, 4223-4240, 1984.

Chester, FM. Effects of temperature on friction: constitutive equations and experiments with quartz gouge, *J. Geophys. Res.* 99:7247-61, 1994.

Dieterich, J. H., Time-dependent friction in rocks, *J. Geophys. Res.*, *77*, 3690-3697, 1972.

Dieterich, J. H., Time-dependent friction and the mechanics of stick-slip, *Pure Appl. Geophys.*, *116*, 790-805, 1978.

Dieterich, J. H., Modeling of rock friction: 1. Experimental results and constitutive equations, *J. Geophys. Res.*, *84,* 2161-2168, 1979.

Dieterich, J. H., and G. Conrad, Effect of humidity on time and velocity-dependent friction in rocks, *J. Geophys. Res., 89,* 4196-4202, 1984.

Dieterich, J. H., and B. Kilgore, Direct observation of frictional contacts: new insights for state-dependent properties, *Pure Appl. Geophys., 143*, 283-302, 1994.

Dieterich, J. H., and B. Kilgore, Imaging surface contacts: power law contact distributions and stresses in quartz, calcite, glass and acrylic plastic, *Tectonophys., 256*, 219-239, 1996.

Evans, B., and D. L. Kohlstedt, Rheology of rocks, *in Rock Physics and Phase Relations, A Handbook of Physical Constants, AGU Reference Shelf 3*, edited by T. J. Ahrens, 148-165, AGU, Washington, D.C., 1995.

Goldsby, D.L., and T.E. Tullis, Dramatic reduction in friction of quartz at rapid but subseismic slip rates, *Seis. Res. Lett., 70*, 247, abstract for SSA meeting, Seattle, WA, 1999.

Hirth, J.P. and J.R. Rice, On the thermodynamics of adsorption at interfaces as it influences decohesion, *Metallurgical Trans. A 11*, 1501-1511, 1980.

Jaoul, O., J. Tullis, and A. K. Kronenberg, The effect of varying water contents on creep behavior of Heavitree quartzite, *J. Geophys. Res., 89*, 4298-4312, 1984.

Kronenberg, A. K., and J. Tullis, Flow strengths of quartz aggregates: Grain size and pressure effects due to hydrolytic weakening, *J. Geophys. Res., 89*, 4281-4297, 1984.

Lachenbruch, A.H., and J.H. Sass, Heat flow and energetics of the San Andreas fault zone, *J. Geophys. Res., 85*, 6185-6222, 1980.

Logan, J.M., M. Friedman, N. Higgs, C. Dengo, and T. Shimamoto, Experimental studies of simulated gouge and their application to studies of natural fault zones, *Proc. Conf. VIII, Analysis of Actual Fault Zones in Bedrock, National Earthquake Hazards Reduction Program, April 1-5, Menlo Park, Ca.*, pp. 305-343, 1979.

Losert, W, J.-C. Geminard, S. Nasuno, and J.P. Gollub, Mechanisms for slow strengthening in granular materials, *Phys. Rev. E, 61*, 4060, 2000.

Mainprice, D. H., and M. S. Paterson, Experimental studies of the role of water in the plasticity of quartzites, *J. Geophys. Res., 89*, 4257-4270, 1984.

Mair, K., and C. Marone, Friction of simulated fault gouge for a wide variety of velocities and normal stresses, *J. Geophys. Res., 104*, 28899-28914, 1999.

Marone, C., Laboratory-derived friction laws and their application to seismic faulting, *Annu. Rev., Earth Planet. Sci.*, *26*, 696, 1998.

Mead, W.J., The geologic role of dilatancy, *J. Geol. 33*, 685-698, 1925.

Michalske, T. A., and E. R. Fuller, Jr., Closure and repropagation of healed cracks in silicate glass, *J. Amer. Ceramic Soc.*, *68*, 5586-5590, 1985.

Mora, P., and D. Place, Numerical simulation of earthquake faults with gouge: toward a comprehensive explanation for the heat flow paradox, *J. Geophys. Res.*, *103*, 21067-21089, 1998.

Mora, P., and D. Place, The weakness of earthquake faults, *Geophys. Res. Lett., 26,* 123-126, 1999.

Morgan, J. K., Numerical simulations of granular shear zones using the distinct element method, 2: Effects of particle size distribution and interparticle friction on mechanical behavior, *J. Geophys. Res.*, *104*, 2721-2732, 1999.

Morgan, J. K., and M. S. Boettcher, Numerical simulations of granular shear zones using the distinct element method, 1: Shear zone kinematics and the micromechanics of localization, *J. Geophys. Res., 104*, 2703-2719, 1999.

Rabinowicz, E., The nature of static and kinetic coefficients of friction, *J. Appl. Phys. 22*, 1373-1379, 1951.

Rice, J.R., Hydrogen and interfacial cohesion, in *Effect of Hydrogen on Behavior of Materials*, ed. A.W. Thompson and I.M. Berstein, Metallurgical Society of AIME, New York, 455-466, 1976.

Ruina, A., Slip instability and state variable friction laws, *J. Geophys. Res.*, *88*, 10359-10370, 1983.

Sammis, C.G., R.H. Osborne, J.L. Anderson, M. Banerdt and P. White, Self-similar cataclasis in the formation of fault gouge, *Pure Appl. Geophys., 124*, 51-77, 1986.

Scholz, C.H., Earthquakes; faults without friction?, *Nature, 381*, 556-557, 1996.

Scholz, C.H., Earthquakes and friction laws, *Nature*, *391*, 37-42, 1998.

Segall, P., and J. R. Rice, Dilatancy, compaction, and slip instability of a fluid-infiltrated fault, *J. Geophys. Res., 100*, 22155-22171, 1995.

Tullis, T.E., and J. D. Weeks, Constitutive behavior and stability of frictional sliding of granite, *Pure Appl. Geophys., 124*, 383-414, 1986.

Wong, T. -f., Y. Gu, T. Yanagidani, and Y. Zhao, Stabilization of faulting by cumulative slip, in *Fault mechanics and transport properties of rocks; a festschrift in honor of W. F. Brace*, Evans, B. and T. -f. Wong (editors), 119-143, 1992.

Yund, R. A., M.L. Blanpied, J.D. Weeks, and T.E. Tullis, Observation and interpretation of microstructures in experimental fault gouges, *J. Geophys. Res., 95*,15589-15602, 1990.

Zoback, M.D., Strength of the San Andreas, *Nature, 405*, 31-32, 2000.

2. The effect of humidity on granular friction at room temperature[1]

Synopsis. We report on laboratory experiments designed to investigate the microphysical processes that result in rate- and state-dependent friction behavior. We study the effect of relative humidity, RH, (<5% to 100%) in velocity stepping tests (10-20 μm/s) and slide-hold-slide (SHS) tests (3-1000 s) on 3 mm thick layers of quartz and alumina powders sheared at 25 MPa normal stress. Granular powders are conditioned in situ under controlled RH to create new surface area before shearing. We find a transition from velocity-strengthening to velocity-weakening frictional behavior as RH increases. The transition occurs at 30-35% RH for quartz and 55-60% RH for alumina. Frictional healing is negligible at low humidity and increases with increasing RH for both materials. The coefficient of sliding friction is independent of humidity. We use normal stress vibrations in SHS tests to isolate chemically assisted healing mechanisms operative within contact junctions from compaction induced granular strengthening. We find that reorganization of granular particles influences friction but that chemically assisted mechanisms dominate. Our data show that rate- and state-dependent friction behavior for granular materials, including time-dependent healing and steady-state velocity dependence, is the result of chemically assisted mechanisms that can be reduced or turned off at low humidity at room temperature in quartz and alumina.

[1] This chapter is *in press* as Frye, K.M. and C. Marone, The effect of humidity on granular friction at room temperature, *J. Geophys. Res.*, 2002.

2.1. Introduction

Active faults exhibit a variety of behaviors from stable creep to stick-slip motion. How shearing is accommodated along a fault is determined by the velocity-, slip-, and time-dependence of the frictional strength, which can be described by rate- and state-dependent friction laws. Laboratory studies have led to an understanding that an asperity contact population evolves during shear [*Rabinowicz*, 1951]. Contact junctions strengthen with age [*Rabinowicz*, 1951], possibly through thermally activated mechanisms that increase the contact area [*Dieterich and Kilgore*, 1994; 1996; *Heslot et al.*, 1994] or the contact bonding quality [*Rice* 1976; *Hirth and Rice*, 1980]. Additionally, the friction behavior of granular materials is a function of shear localization and density changes. Although the empirical rate- and state-dependent laws have been applied successfully to many types of laboratory data and field observations [see *Marone*, 1998a, and *Scholz*, 1998 for reviews] the precise physical mechanisms responsible for the friction behaviors they describe remain poorly understood. Ideally, laboratory experiments would identify the fundamental, crystal lattice-scale and meso-scale mechanisms of friction under the range of geological conditions relevant to the seismic cycle [*Tullis*, 1988; *Evans and Chester*, 1995]. However, our present understanding of fault material properties together with technical limitations in the laboratory do not allow that level of generality. Instead, in this paper we address the physico-chemical mechanisms responsible for rate- and state-dependent friction effects in quartz and alumina at room temperature. We focus on the fundamental observations on which rate and state friction laws are based: velocity-dependence of steady-state sliding friction and time-dependent healing [*Dieterich*, 1972, 1978, 1979; *Ruina*, 1983; *Tullis and Weeks*, 1986; *Chester*, 1994; *Beeler et al.*, 1994; *Marone*, 1998a].

We investigate the influence of water on friction by varying humidity and attempt to separate water-assisted healing from the effects of consolidation and porosity changes in granular layers.

2.1.1. The Influence of Water

Contact junction strengthening can be achieved through increasing either the quantity of contact area or quality of contact. If asperities on surfaces in brittle frictional contact are assumed to be in a state of incipient plastic flow [*Bowden and Tabor,* 1964], then time-dependent contact deformation is one possible cause of time- and velocity-dependent friction behaviors. Water is observed to enhance both point defect and dislocation migration in single-crystal quartz, quartz-aggregate, and quartzite systems [*Blacic and Christie,* 1984; *Jaoul et al.,* 1984; *Mainprice and Paterson,* 1984; *Kronenberg and Tullis,* 1984; *Evans and Kohlstedt,* 1995]. Thus, water-assisted plastic deformation, commonly known as hydrolytic weakening, could be a mechanism by which the real area of contact grows and the frictional strength of two surfaces increases. If asperities are in purely elastic contact, then time-dependent strengthening can be accomplished through Hydrogen bonding [*Rice*, 1976; *Michalske and Fuller*, 1985] or water adsorption/desorption at contact points [*Hirth and Rice*, 1980]. Other possible water-assisted mechanisms of frictional healing are capillary bridging [*Crassous et al.,* 1994; *Iwamatsu and Horii,* 1996], pressure solution [*Dove and Elston,* 1992; *Dove,* 1994; *Bos et al.*, 2000], and subcritical crack growth [*Martin and Durham,* 1975; *Costin,* 1987].

Dieterich and Conrad [1984] studied bare quartzite surfaces and found that low humidity conditions resulted in higher values of sliding friction, a lack of time-dependent healing, a switch to velocity strengthening, and greater tendency for stable sliding. Their results imply that hydrolytic weakening influences the friction evolution effect; however the experimental database

was small and it was not clear whether water had an effect on steady-state velocity-dependence of friction or the friction direct effect. Similar data are not available for granular materials. Thus, we study the friction behavior of quartz sand at different humidity levels and examine the relative importance of contact junction processes in determining granular friction behavior.

Alumina serves as a useful comparison since its properties are well documented in engineering literature. In experiments performed with alumina ceramic, *Gates et al.* [1989] found that a weak surface layer was formed in the presence of water during sliding. They interpret the layer as the result of a tribochemical reaction that produces aluminum oxide hydroxide.

2.1.2. Shear Localization and Granular Reorganization

While the friction behavior of bare surfaces can be thought of in terms of asperity interaction, friction of granular materials is more complex. Grains rotate, break and undergo contact slip, and networks of grains in shear localization fabrics and stress chains influence the frictional properties of granular layers [*Sammis et al.*, 1987; *Wong et al.*, 1992; *Jaeger et al.*, 1996; *deGennes*, 1999; *Geminard et al.*, 1999]. Slip localizes within granular layers (Figure 2.1), and at normal stresses above the particle strength, localization evolves with displacement. These textural effects and the role of dilation and porosity changes are well documented [*Marone et al.*, 1990; *Segall and Rice,* 1995; *Sleep,* 1997; *Mair and Marone*, 1999]. Yet the role of contact junction processes versus granular reorganization and shear fabric is poorly understood. Theoretical studies of granular friction often employ a strategy where intergranular friction is constant, and the distribution of stress throughout the granular layers is studied [*Mora and Place*, 1998; *Morgan*, 1999; *Morgan and Boettcher,* 1999]. These models indicate that stress is

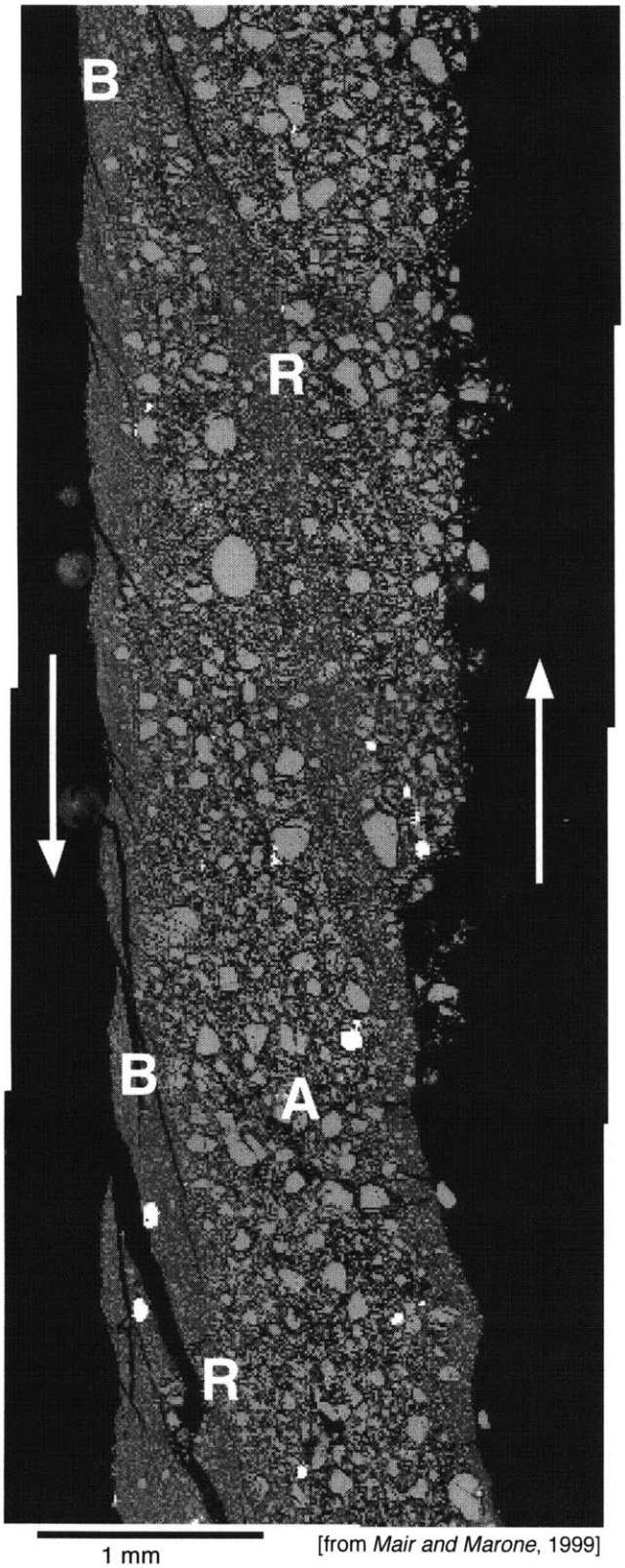

Figure 2.1. Back-scattered electron micrograph of a granular layer after 20 mm of left-lateral shear at σ_n=50 MPa [from *Mair and Marone*, 1999]. Areas of intense comminution are interpreted as boundary (B) and Riedel (R) shears. These zones are surrounded by relatively undisturbed regions (A) where little slip occurs.

distributed unevenly throughout the granular layer, and that the formation and destruction of load bearing "stress-chains" play an important role in friction of granular materials.

In the context of earthquake physics, the above issues bring out an important question. Is the frictional behavior of gouge-filled fault zones controlled by contact junction processes, the consolidation state of the granular material, or both? Granular materials exhibit much more compaction and dilation during loading perturbations than bare surfaces. *Marone and Kilgore* [1993] and *Sleep et al.* [2000] suggest that the stability and time-dependence of gouge friction is influenced by changes in the thickness of the localized shear zone. Reorganization of the fault gouge during compaction results in more widely distributed shear and smaller strain rates, and may be modeled with the rate- and state-dependent constitutive laws if velocity is expressed in terms of strain rate.

We propose that frictional healing between slip events under ambient laboratory conditions is a function of both granular consolidation and water-assisted, time-dependent strengthening of contact junctions. We perform experiments as a function of relative humidity (RH) to alter the kinetics of contact junction strengthening processes. We find that healing behavior varies significantly as a function of RH for both quartz and alumina powders, while compaction and dilation show less variation, and thus we infer that rate and state friction behavior is due to chemically assisted contact junctions processes.

2.2. Experiment Procedure

All laboratory experiments in this study were performed in a double-direct shear apparatus [for details see *Marone,* 1998a; *Karner and Marone*, 2000]. In this configuration, two frictional surfaces are sheared simultaneously (Figure 2.2, inset). Shear load was applied as a

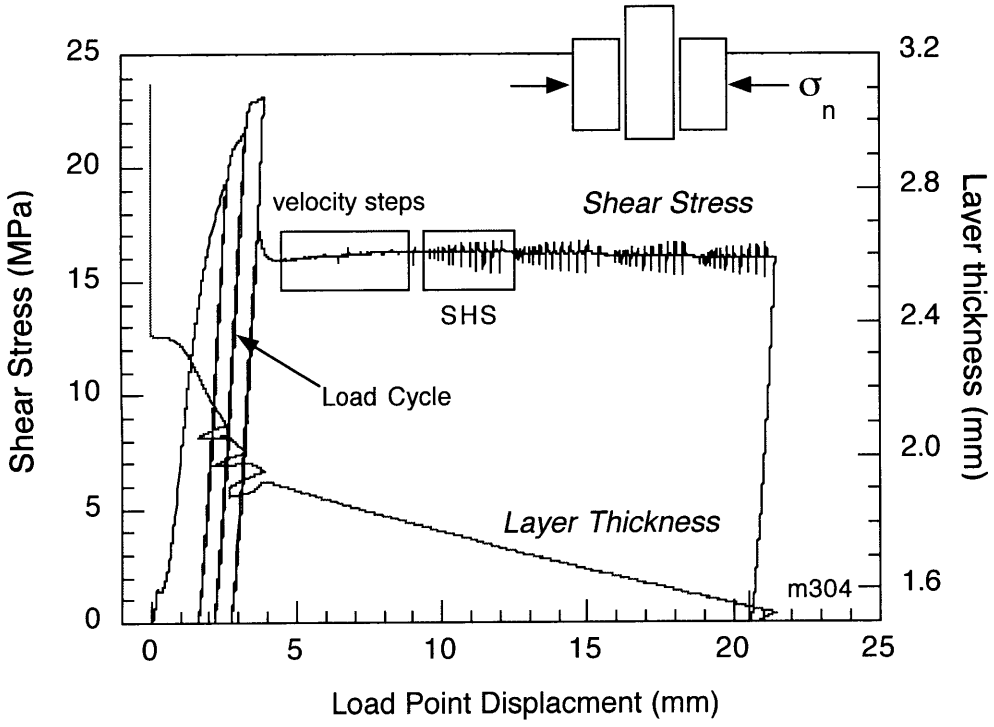

Figure 2.2. Shear stress and layer thickness history for an entire experiment. Gouge layers are subject to three shear load cycles at high normal stress (40 MPa) to create fresh surface area before velocity stepping tests and SHS tests are carried out at normal stress 25 MPa. Layer thickness decreases throughout the experiment due to comminution and geometric thinning. Superimposed upon this thinning trend are layer thickness perturbations associated with velocity steps and SHS.

vertical displacement or rate boundary condition by servo-control with 0.1 μm resolution. The horizontal ram applied normal force in load-feedback mode with 0.1 kN resolution. Position and applied force are measured at each load point at a sampling rate of 1 to 10 kHz. The raw data is averaged and recorded at 1 to 10 samples/s.

2.2.1. Apparatus and Materials

Test samples consisted of 3 mm-thick layers of quartz or alumina powder sheared between rough steel forcing blocks. Grooves were machined perpendicular to the shear direction to eliminate slip at the layer boundaries and confine shear within the granular layers. The nominal area of contact was constant at 10 cm x 10 cm during tests.

The quartz-powder was subangular Ottawa sand, which is > 99% SiO_2 as supplied by the US Silica Co. We used Natural Grain product F-110, which has an initial median particle size of 110 μm and a size range of 50-150 μm. The quartz powder was heated in a vacuum oven to 110° C to remove excess surface water. The alumina was 95% purity, with an initial mean particle size of 122 μm, a size range of 100-150 μm, and was not oven dried. Significant crushing occurs during shear, such that the mean particle size is <10 μm during steady state frictional shear.

Gouge layers were constructed in a leveling jig to ensure that layers were uniform and reproducibly 3.0 mm thick. Cellophane tape was used to confine layer edges during construction, which was carried out on the side (sample) blocks. The 3-block sample (see inset to Figure 2.2) was assembled by placing the center block on top of one gouge layer and side block, securing this with tape, and then positioning these two blocks on the second side block. When this configuration was secured with tape, steel plates were fastened to the side blocks to cover the

front and rear layer edges and thin copper shims were added below each layer to reduce gouge loss during shear. The steel plates made a zero-load sliding contact with the center forcing block, which was coated with MoS_2 lubricant to reduce friction. The base of the copper shims and side blocks and the top of the center block were also lubricated to allow lateral motion during shear.

2.2.2. Experiment Technique

The test sample and loading system were isolated from room atmosphere with a flexible membrane and RH was varied from <5% to 100% (Table 2.1, end of chapter). Depending on the desired experiment humidity, a desiccator or a humidifier was placed in the test chamber with the sample and a hygrometer. To allow the granular layer to equilibrate at a given humidity, unsaturated samples were held in the controlled humidity environment for 12 hours before normal load was applied. Saturated experiments were performed by wrapping the sample assembly in latex, applying a small normal force, and adding water or brine until the jacket was filled. Thus, the granular layers were fully submerged in these experiments.

After samples equilibrated in the controlled humidity chamber, normal stress σ_n was raised to 40 MPa and three shear load cycles were performed to enhance grain crushing and produce new surface area *in situ* (Figure 2.2). Normal stress was then reduced to 25 MPa and shearing was carried out at a rate of 10 μm/s. To further condition the gouge layers and establish a steady-state friction level, we performed velocity stepping experiments for the displacement range 5 to 9 mm. SHS tests were performed for the displacement interval 9 to 13 mm.

2.2.3. Gouge Preconditioning and Surface Area

Since it is not possible to reliably vary RH within a given experiment, different experiments must be compared. In order to resolve the effect of humidity on second-order friction behavior, we found that gouge layers had to be ground *in situ* under controlled RH and that initial layer thickness, displacement history, and normal stress history had to be identical in all experiments. Comminution was enhanced by the load cycles at high normal stress (Figure 2.2). This also helped localize shear and resulted in steady state friction being reached in less net displacement than without the load cycles.

2.3. Data and Observations

We use slide-hold-slide (SHS) tests to assess the effect of humidity on static friction and time dependent frictional restrengthening. Following the methods of *Dieterich* [1972], *Beeler et al.* [1994], and *Marone* [1998b] the load point is stopped for periods of 3-1000 s after which loading resumes and 'static' friction is measured (Figure 2.3). Because of the frictional rheology and finite stiffness of the testing apparatus, frictional creep occurs during holds (Figure 2.3a). When the vertical ram is restarted at the initial driving velocity, hardening occurs until a frictional yield strength is overcome and then friction returns to steady-state sliding. The difference between the peak and steady-state sliding friction is defined as healing ($\Delta\mu$). We focus on SHS tests in the shear displacement range of 9 to 13 mm (shear strains of 4 to 7) for this study.

2.3.1. Effect of Humidity on Frictional Healing

Figures 2.3a and 2.3b show SHS data for an experiment conducted at 55% RH. SHS tests conducted at lower humidity are qualitatively different (Figure 2.3c). Frictional creep ($\Delta\mu_c$)

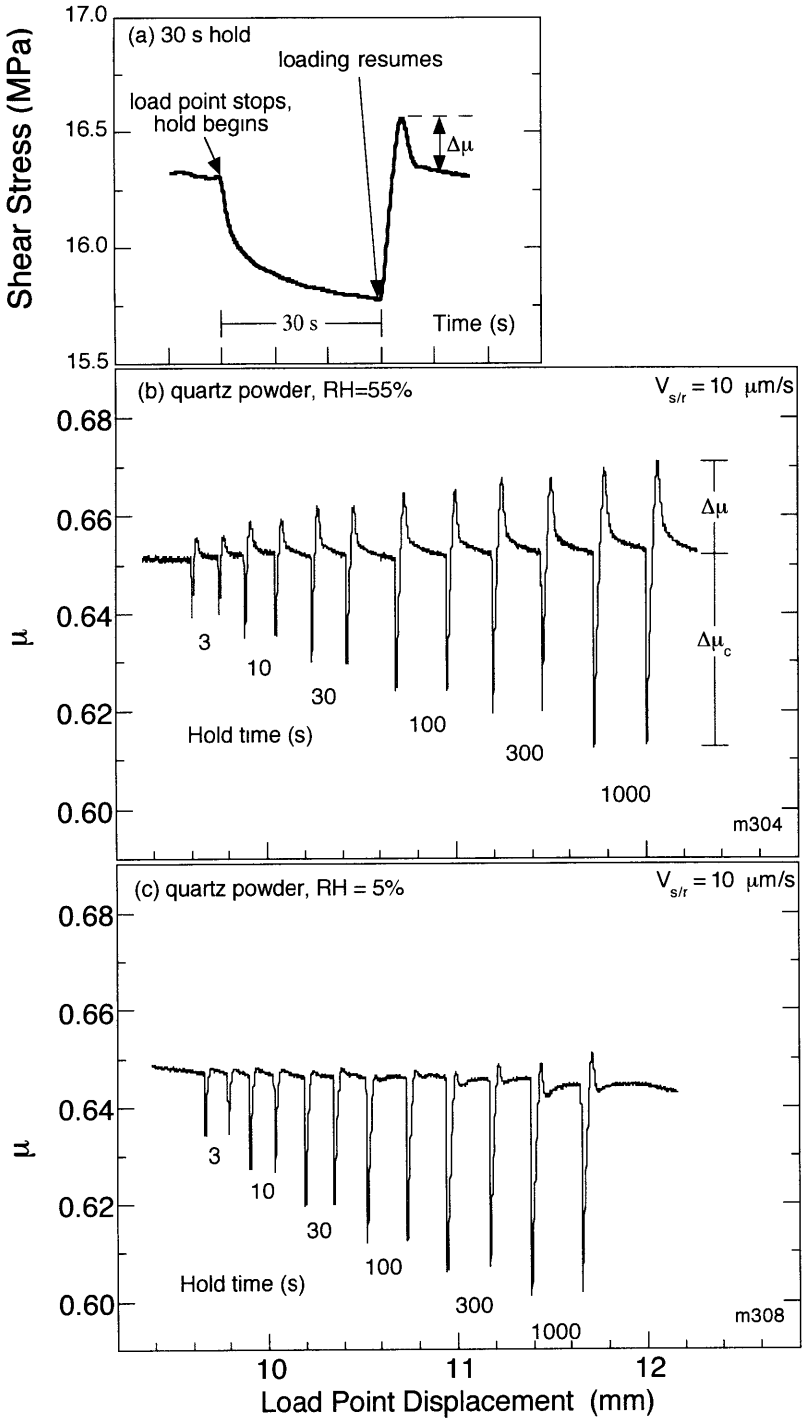

Figure 2.3. SHS tests for quartz powder. (a) Typical 30 s hold shows frictional creep when load point stops and stress peak when loading resumes. (b) Typical set of SHS tests performed at 55% RH illustrate frictional creep ($\Delta\mu_c$) and frictional healing ($\Delta\mu$). (c) Under dry conditions, with the same displacement history shown for panel b, healing is negligible.

is greater during low humidity holds, and peak friction is smaller than corresponding tests at higher humidity. The low humidity experiments exhibit negligible healing and little to no time dependence of $\Delta\mu$.

Humidity step tests [*Dieterich and Conrad*, 1984] were performed to check that humidity effects are independent of net shear strain or other minor effects that may vary between experiments (Figure 2.4). For these tests we began with the procedure for a low humidity run and then opened the test chamber and added water directly to the granular layers, raising RH to 100%. Figure 2.4 shows that SHS tests performed immediately after adding water demonstrate high-humidity behavior; thus humidity effects are not coupled with net displacement or other factors related to gouge zone microstructure.

2.3.1.1. Quartz powder

Figure 2.5 shows the systematic friction behavior for quartz-powder at four values of RH. At low humidity, frictional peaks are very small after holds, and there is little time dependence. At 25% RH, frictional peaks are observable after holds, and they evolve over a finite displacement back to steady-state sliding friction. As RH increases, healing rates and the evolution distance increase.

2.3.1.2. Alumina powder

While quartz powder begins to display some time-dependent healing at RH > 5%, alumina powder does not exhibit significant healing for RH up to 50% (Figure 2.6). Both the qualitative and quantitative character of frictional healing of alumina varies with RH. At low humidity, SHS tests do not exhibit a clear friction peak, instead evolving gradually back to steady sliding. The friction behavior at 5% RH indicates negligible strengthening during quasi-

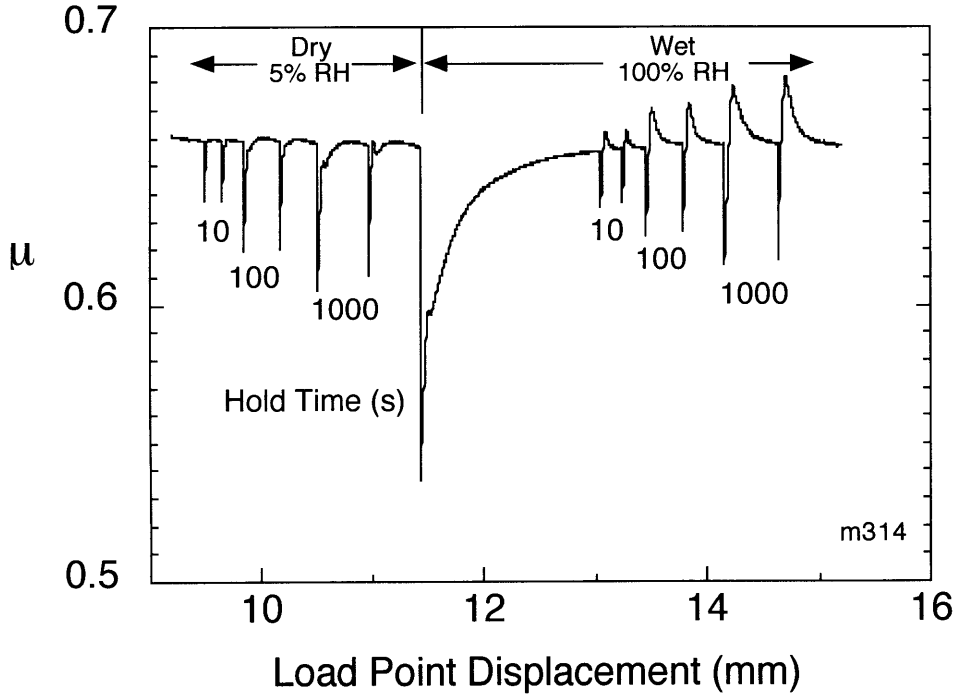

Figure 2.4. Humidity step test showing the effect of adding water to a low RH experiment. Healing is negligible under dry conditions, but after water is added distinct frictional peaks and time dependent healing are observed.

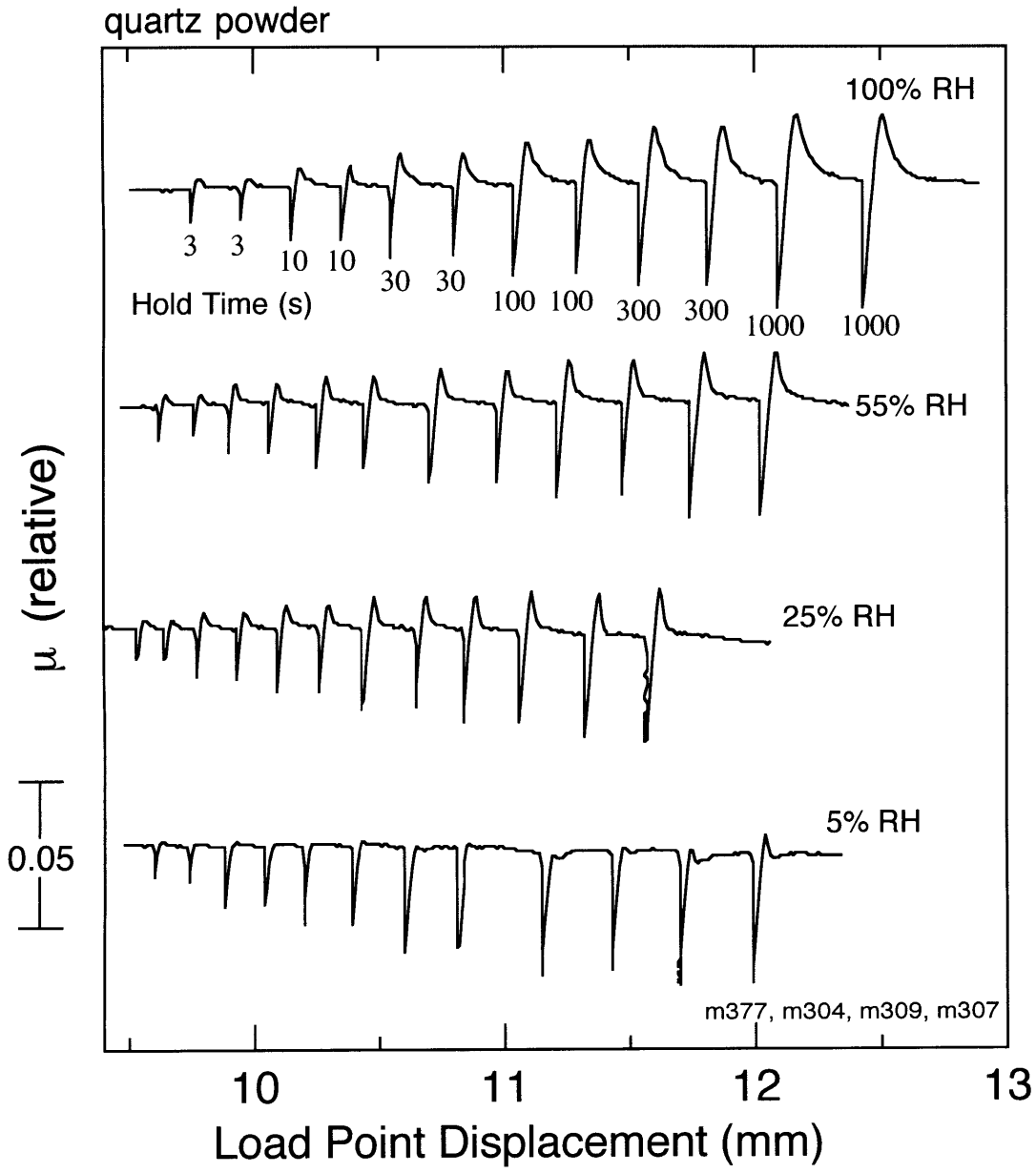

Figure 2.5. Data from four experiments on quartz powder performed at different values of RH. The same sequence of hold times, labeled on the 100% RH test, were used in each experiment. Friction is offset vertically for clarity. The low humidity tests exhibit little healing. Healing rates increase with humidity and approach a constant value above 55%. The evolution distance needed to reach steady-state sliding after a hold increases with RH.

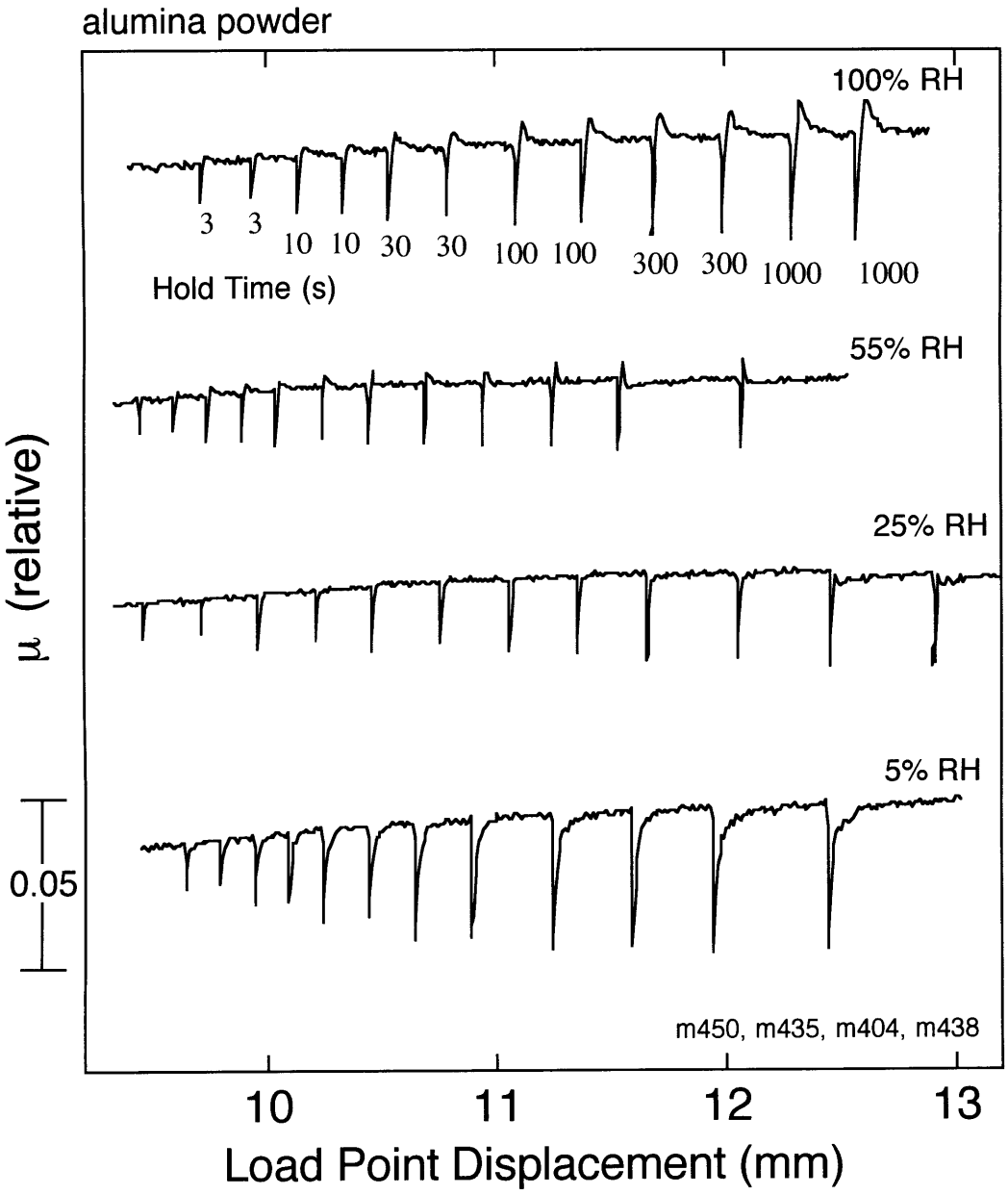

Figure 2.6. Data from four experiments on alumina powder performed at different values of RH. The same sequence of hold times, labeled on the 100% RH test, were used in each experiment. Friction is offset vertically for clarity. The low humidity tests exhibit little healing. Frictional peaks become measurable above 50% RH. The evolution distance needed to reach steady-state sliding after a hold is negligible for the intermediate RH cases.

static holds, allowing sample slip earlier during reloading. Net healing is zero at 25% RH (Figure 2.6) and data resemble quartz powder at 5% RH: both healing rate and evolution distance are near zero. With increasing RH, peak friction increases and the evolution distance decreases. For both alumina and quartz, creep relaxation during holds is independent of humidity.

SHS tests show that several aspects of frictional restrengthening vary systematically with humidity. We show healing data for a given hold time as a function of RH in Figure 2.7. For quartz, $\Delta\mu$ increases rapidly at low humidity and saturates at roughly 50% RH. Alumina-powder exhibits no observable healing until 45-50% RH. Healing increases with humidity from 50-100%. Four data points from two alumina experiments overlap at 100% RH. Although healing varies with humidity, the steady-state coefficient of friction is remarkably consistent, independent of RH. This result differs from the findings of *Dieterich and Conrad*, [1984], who observed a strong humidity dependence of μ_{ss} in their work on bare quartzite surfaces without gouge. The RH-dependence observed by *Dieterich and Conrad* [1984] could be due to lower experimental humidity in their "dry" case, or bare surfaces could be fundamentally different from powders. Numerical studies of granular friction [e.g. *Morgan*, 1999; *Thornton*, 2000] indicate that sliding friction of granular systems is nearly independent of inter-particle friction, thus we favor the latter interpretation.

2.3.2. Layer Thickness Changes

We made high-resolution measurements of layer thickness changes during SHS tests in order to assess the role of compaction and granular densification in healing. Figure 2.8 shows an example of the relationship between frictional strength and layer thickness during a 30 s SHS test. A linear trend has been removed from the thickness data to account for geometric layer

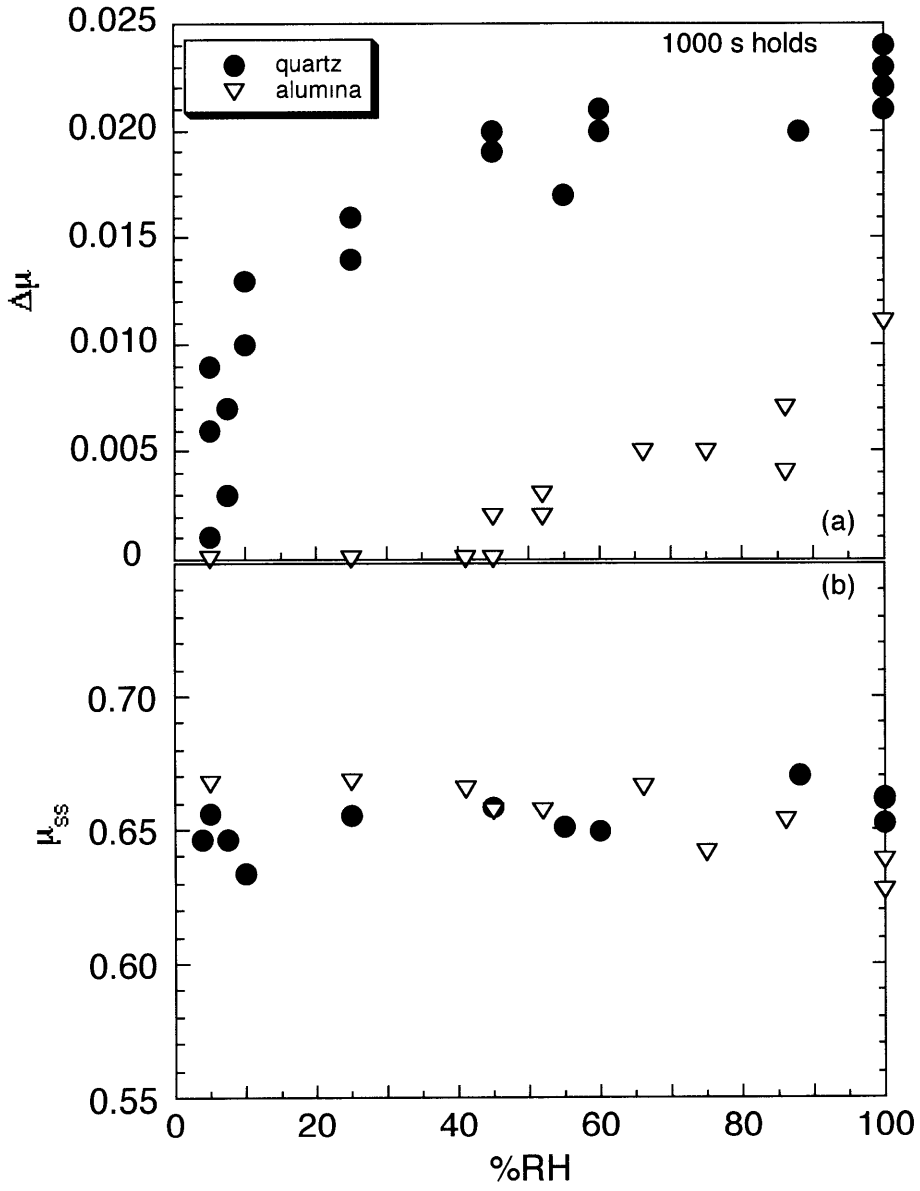

Figure 2.7. (a) Comparison of healing ($\Delta\mu$) measured after 1000 s holds for both quartz and alumina powders as a function of RH. Healing increases dramatically for quartz from 5-25% RH and then approaches a constant value above 55% RH. Alumina exhibits negligible healing for RH < 50% and much less healing than quartz for all humidities. Data points from three saturated (100% RH) alumina powder experiments have the same value and plot over one another. (b) The steady-state coefficient of sliding friction measured at 9.5 mm (μ_{ss}) is remarkably consistent through the entire range of measured RH. Experimental reproducibility for a given humidity is high because great care is taken to prepare identical samples and each experiment is run with identical shear displacement and normal stress history.

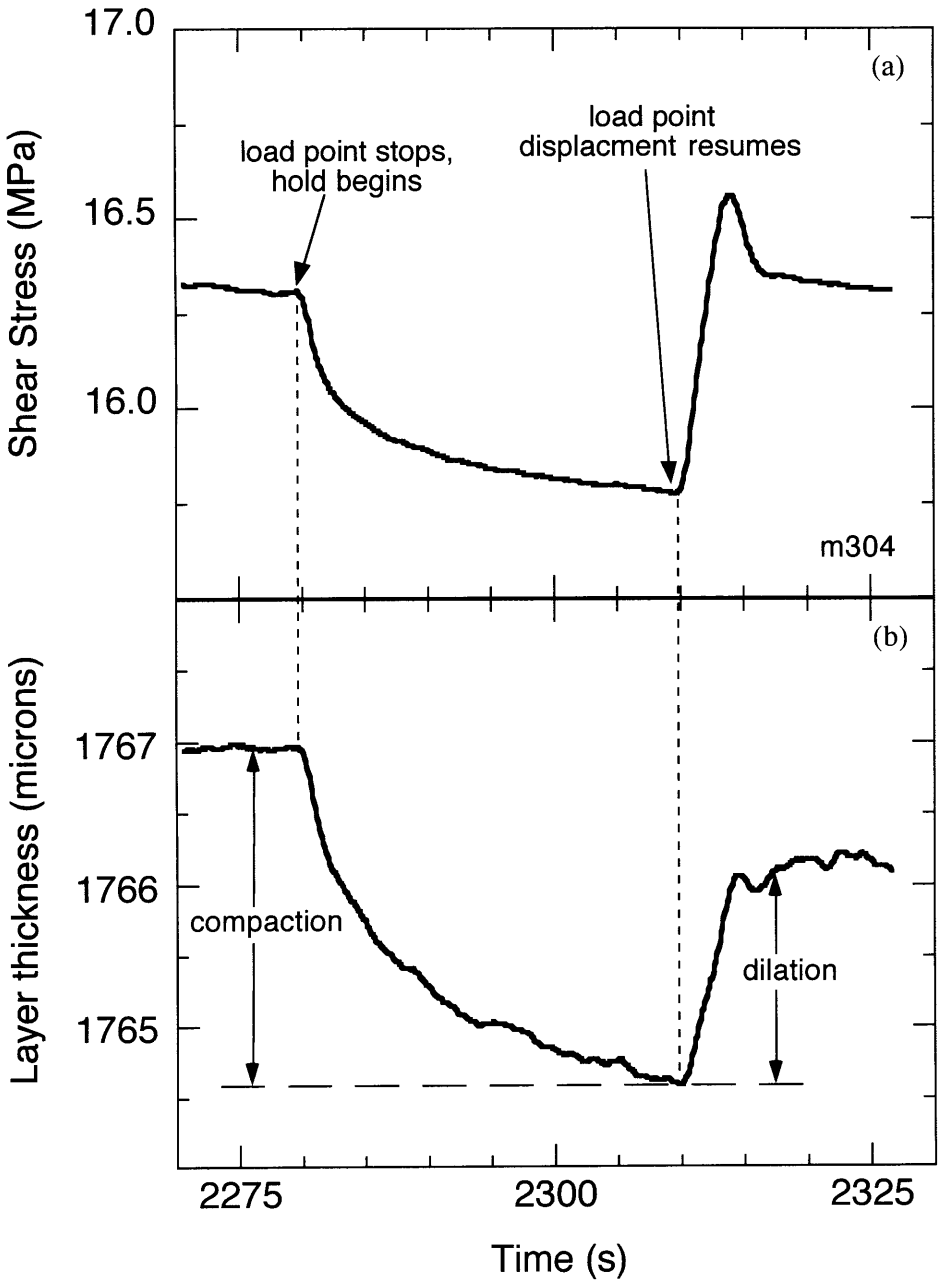

Figure 2.8. (a) The 30 s SHS test from figure 3a is shown with (b) corresponding layer thickness change. Compaction occurs during the hold as shear stress relaxation occurs. When loading resumes, the layer dilates to accommodate displacement.

thinning (e.g. see Figure 2.2). Layer thickness decreases during the hold until loading resumes. At that point, dilation occurs until peak static strength is reached. The magnitude of dilation is less than compaction, indicating that SHS tests result in an increment of irrecoverable compaction. Previous work on quartz powders by *Karner and Marone* [2001] suggests that this net compaction occurs outside of zones of localized shear.

Figure 2.9 shows a comparison of healing and compaction data from a suite of tests on quartz. Healing rate $\beta=\Delta\mu/log_{10}t_h$ increases systematically with increasing humidity. Compaction increases linearly with log hold time, even when healing is negligible (Figure 2.9b). A similar response occurs for alumina (Figure 2.10). We find that healing rate increases systematically with increasing humidity, while compaction in alumina powders does not vary greatly with humidity. Systematic variations in creep ($\Delta\mu_c$), compaction, and dilation are evident in both quartz and alumina experiments (Figure 2.11), but these variations do not correlate with the healing data. SHS dilation is consistently less than SHS compaction and thus net compaction (Figure 2.8) occurs for the entire range of conditions studied.

2.3.3. Normal Stress Oscillations

Although we are able to eliminate frictional healing at low humidity without changing the compaction signal (Figures 2.9 and 2.10), the work of *Richardson and Marone* [1999] shows a correlation between compaction and frictional healing. Their tests were performed at room temperature and humidity, and compaction was varied by applying normal stress oscillations during quasistatic holds. To investigate these observations further, we perform similar normal stress oscillations during SHS tests (Figure 2.12) at low and high RH, using the technique of *Richardson and Marone* [1999]. When the shear load point was stopped, a 1 Hz periodic

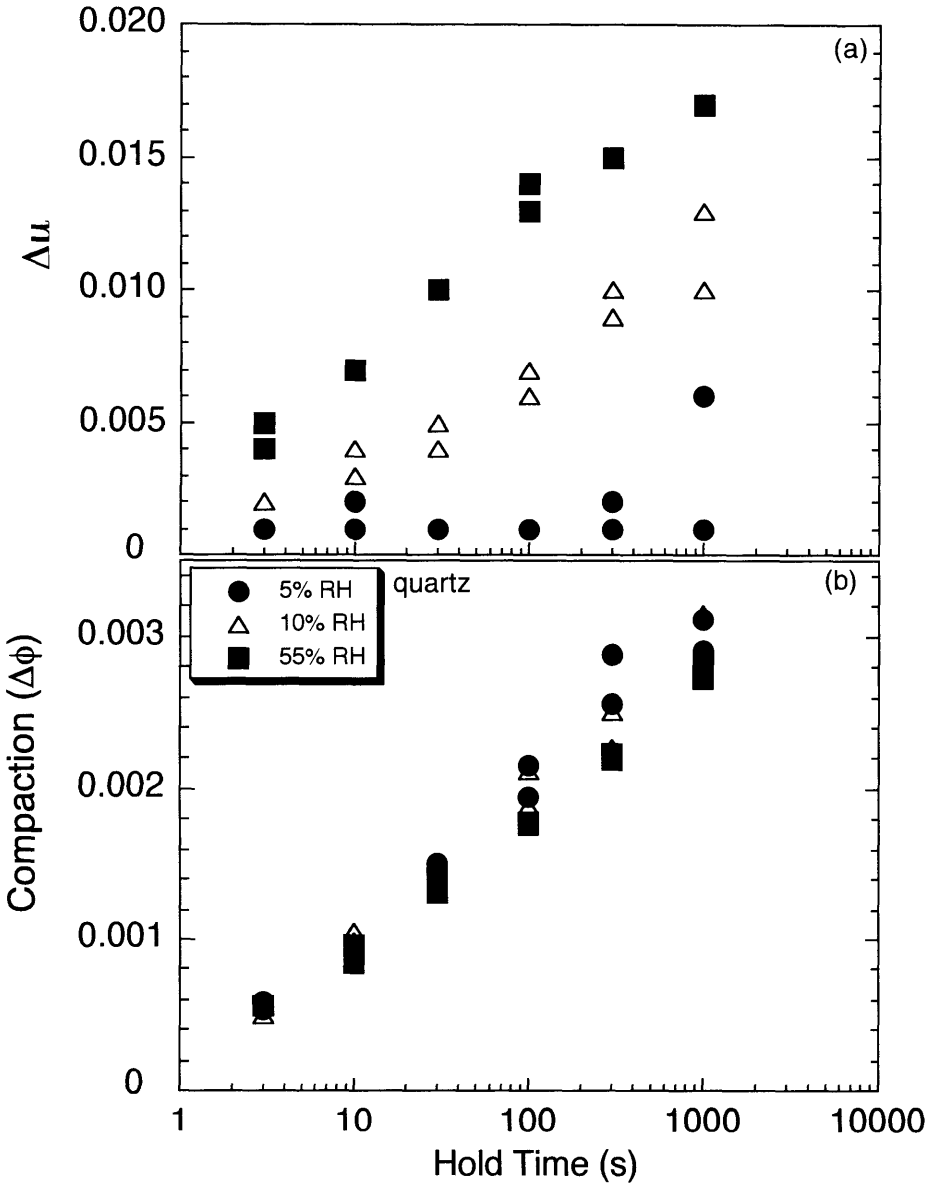

Figure 2.9. (a) Three representative sets of healing data for quartz powder. Healing is negligible at 5% RH, and increases with increasing RH. Healing rate also increases with RH. (b) Compaction proceeds linearly with log hold time and is independent of RH. Compaction is defined as change in layer thickness during the hold divided by layer thickness before the hold.

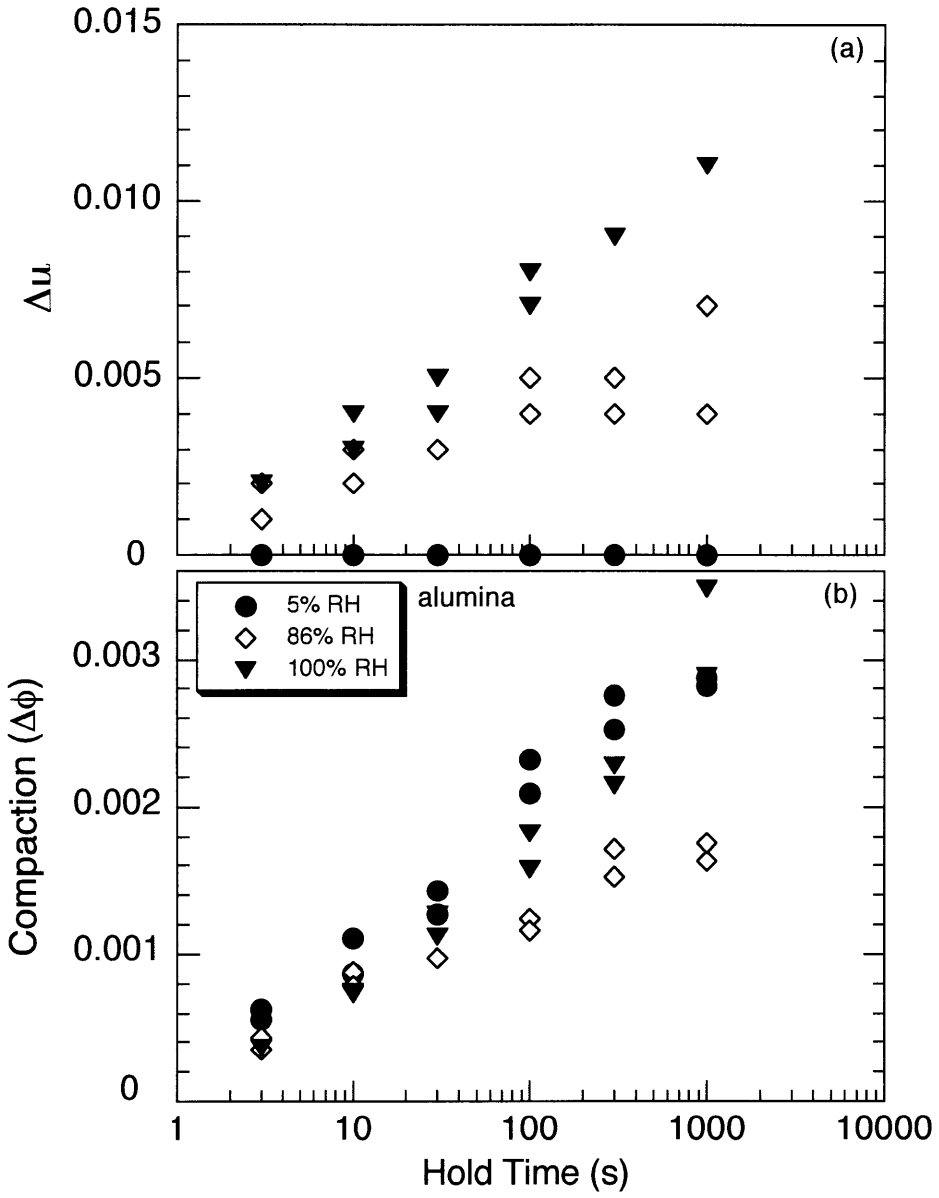

Figure 2.10. (a) Three representative sets of healing data for alumina powder. Healing is negligible at 5% RH, and increases with increasing RH. Healing rate also increases with RH. (b) Compaction proceeds linearly with log hold time and is independent of RH. Compaction is defined as change in layer thickness during the hold divided by layer thickness before the hold.

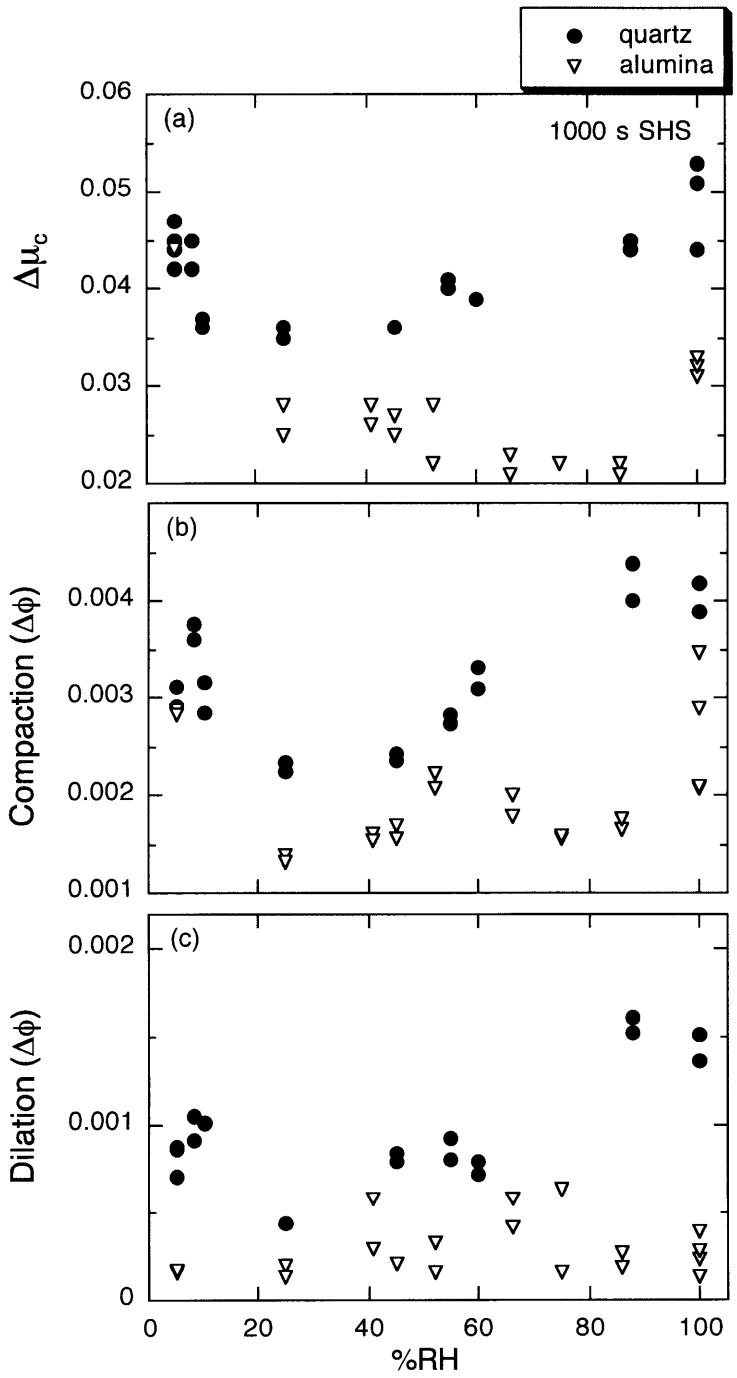

Figure 2.11. (a) $\Delta\mu_c$, (b) compaction, and (c) dilation all vary with RH for both alumina and quartz. The largest values for creep, compaction and dilation occur at very low and very high RH.

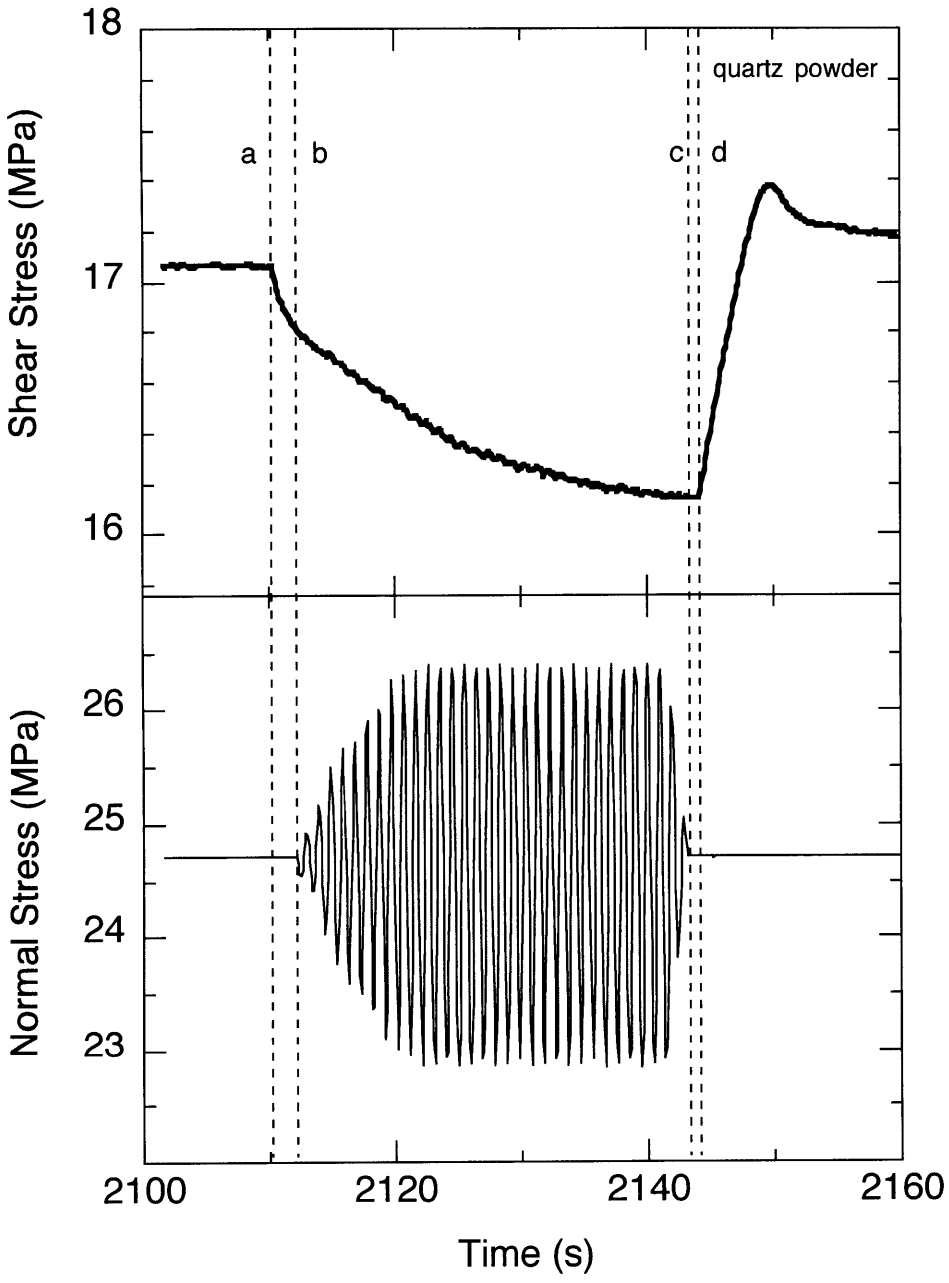

Figure 2.12. Shear stress and normal stress vs. time for a quartz powder SHS test with normal stress oscillations. Fiducial lines mark where (a) the load point stops, (b) oscillations begin, (c) oscillations stop, and (d) shear loading resumes. Note that oscillation amplitude increases gradually over roughly a 5 second interval.

oscillation signal was summed with the normal load servo-control signal. The signal was ramped to its peak amplitude (3.53-3.55 MPa) at the beginning of the hold and rapidly ramped down at the end of the hold. The ramps were employed to reduce instabilities that are common to fluctuating normal stress experiments [*Richardson and Marone*, 1999; *Boettcher and Marone,* 2001].

Normal stress vibrations resulted in greater healing relative to constant normal stress experiments at both low and high humidity (Figure 2.13). For a given hold time, vibration increased compaction by a factor of 2 relative to constant normal stress tests. Low humidity healing is non-zero but less than 45% RH healing in vibrated SHS tests. At low humidity, there is a change in healing rate at about 100 s, suggesting that the healing mechanism saturates at relatively short time scales for dry conditions.

2.3.4. Velocity Stepping Tests

Velocity stepping experiments were performed from 5 to 10 mm displacement in all experiments and again from 13 to 15 mm displacement in alumina experiments. Load point velocity was alternated from 10 to 20 μm/s and sliding occurred at each velocity until a new steady-state value of friction was reached. In general, the friction response we observed was similar to previous work [e.g., *Dieterich*, 1979, *Marone*, 1998a].

For quartz powder under dry conditions (≤25% RH), μ_{ss} increased with increasing velocity, indicating velocity-strengthening behavior (Figure 2.14). There is a transition to velocity weakening behavior with increasing humidity. The behavior of alumina powder is similar to that of quartz (Figure 2.15), but the degree of velocity strengthening at low RH is much greater for alumina than for quartz.

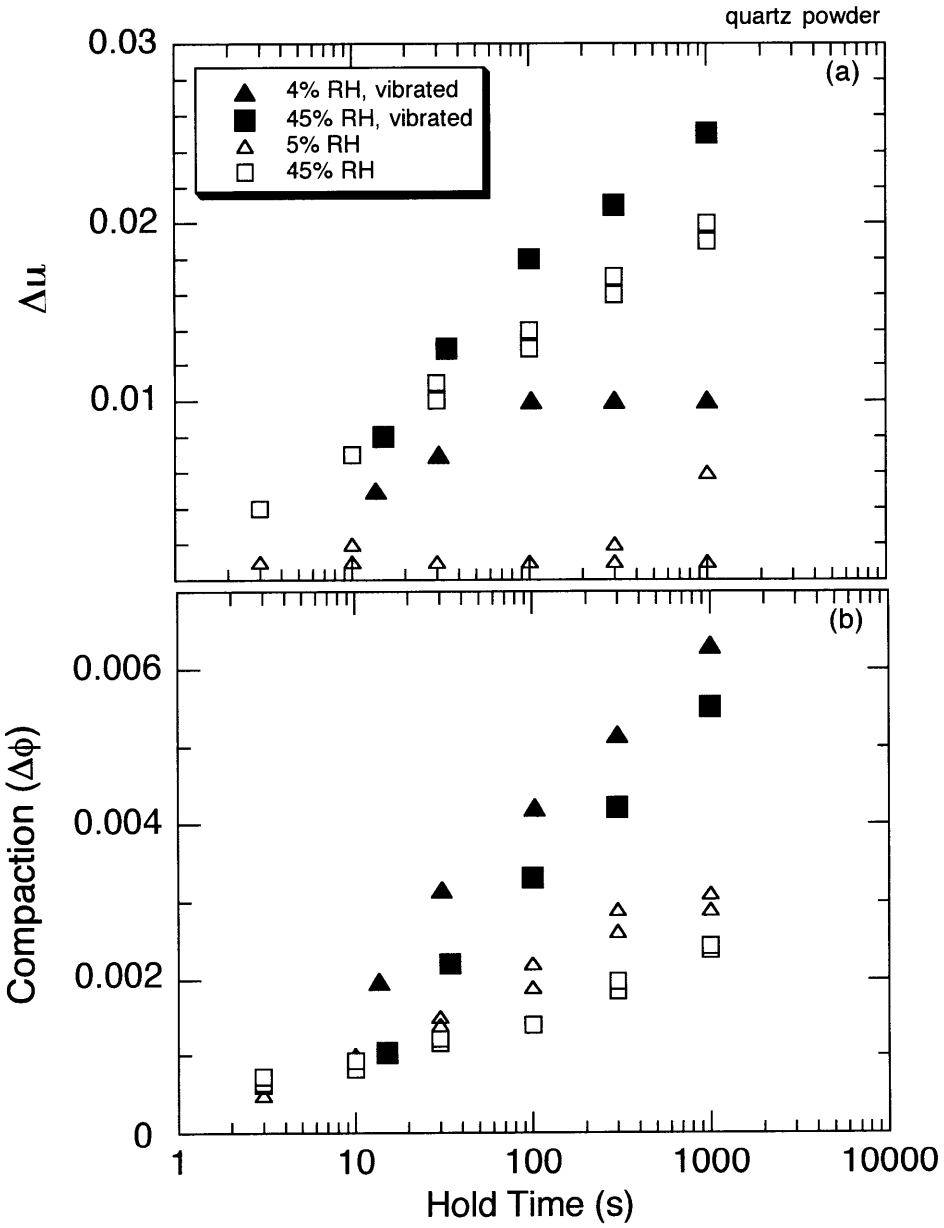

Figure 2.13. (a) Healing vs. hold time for vibrated and constant normal stress SHS tests (quartz powder). Data from vibrated tests show greater healing than constant normal stress tests at a given humidity. In the dry tests, vibration enhanced healing becomes constant for hold times greater than 100 s. (b) Compaction during normal stress vibration tests are approximately double those of constant normal stress tests.

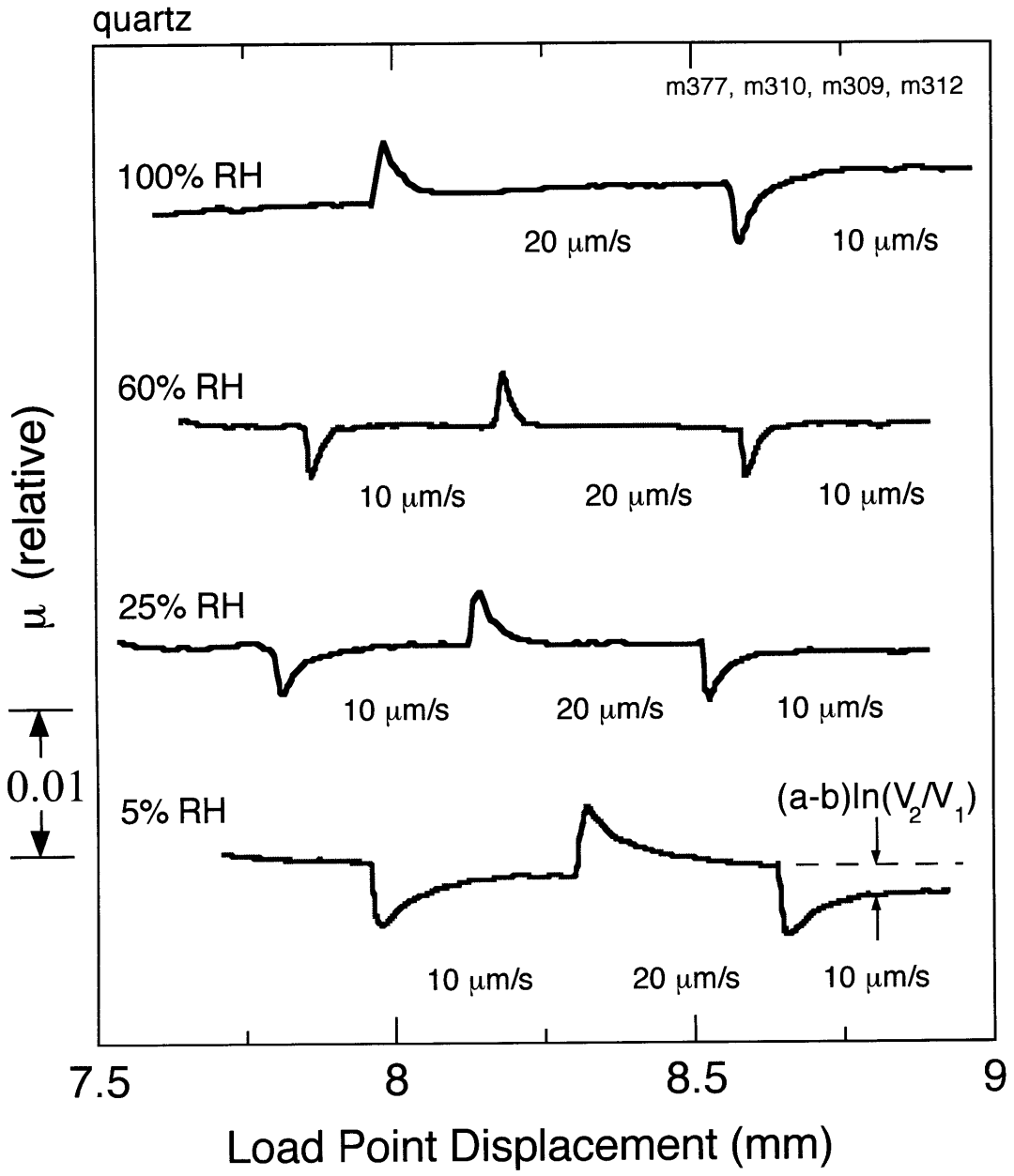

Figure 2.14. Four sets of quartz powder velocity-stepping tests performed at different values of RH. Friction data are offset vertically for clarity. The low humidity tests demonstrate velocity strengthening. At 8.5-9 mm displacement, quartz powder becomes velocity neutral at 60% RH and velocity weakening at 100 % RH.

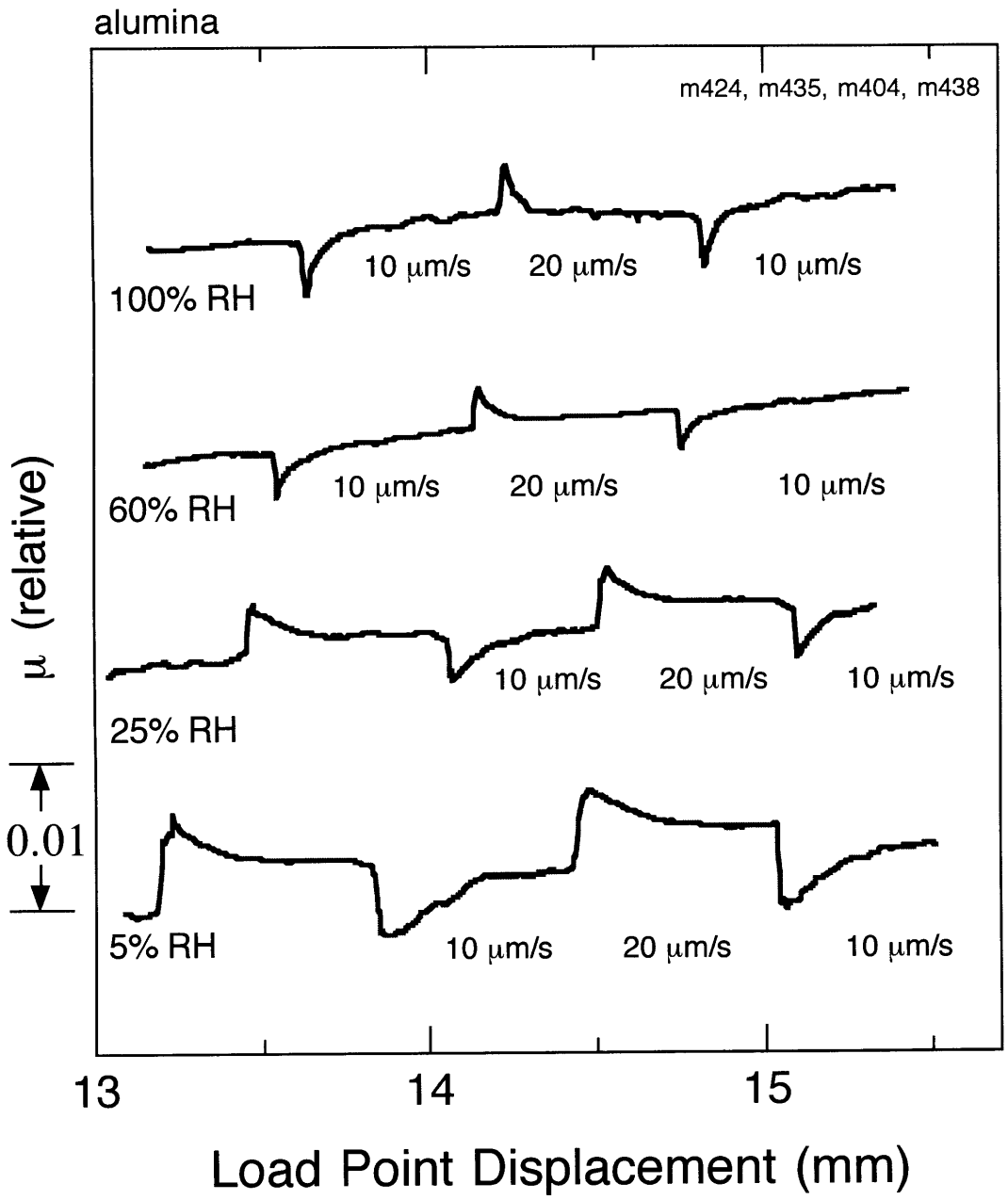

Figure 2.15. Four sets of alumina powder velocity-stepping tests performed at different values of RH. Friction data are offset vertically for clarity. The low humidity tests demonstrate velocity strengthening. At 14-15 mm displacement, alumina powder becomes velocity neutral at RH > 60% and velocity weakening at 100 % RH.

The velocity dependence of steady state friction, *(a-b)* [*Dieterich*, 1978, 1979; and *Ruina*, 1983], is taken directly from velocity stepping data (Figure 2.14). *(a-b)* changes from velocity strengthening to velocity weakening at ~35% RH for quartz-powder and ~65% RH for alumina-powder (Figure 2.16). The variation of velocity dependence with humidity is much greater for the alumina-powder than for quartz. Figure 2.17 shows representative constitutive parameters for our range of experimental conditions. The velocity stepping data were modeled using the *Dieterich* formulation for rate- and state-dependent friction:

$$\mu = \mu_0 + a\ln\left(\frac{V}{V_0}\right) + b\ln\left(\frac{V_0\theta}{D_c}\right), \tag{2.1}$$

$$\frac{d\theta}{dt} = 1 - \frac{V\theta}{D_c}, \tag{2.2}$$

where μ is friction at sliding velocity V, μ_0 is friction at reference velocity V_0, θ is the state parameter, D_c is the evolution distance, and a and b are empirical constants. We use an iterative, non-linear, least-squares inversion. For quartz, we find that the friction parameter a (direct effect) decreases with increasing humidity, approaching a constant value after 25% RH. The evolution term b increases with increasing RH, and D_c decreases as RH increases. For alumina, the parameters a and b decrease with increasing RH to minimum values at 86% RH, but are dramatically larger at 100% RH. D_c decreases with increasing RH from very large values at low RH (Figure 2.17). The measured values of a and b are comparable to those measured by *Tullis and Weeks* [1986] for granite bare surfaces, while D_c is larger for our granular samples.

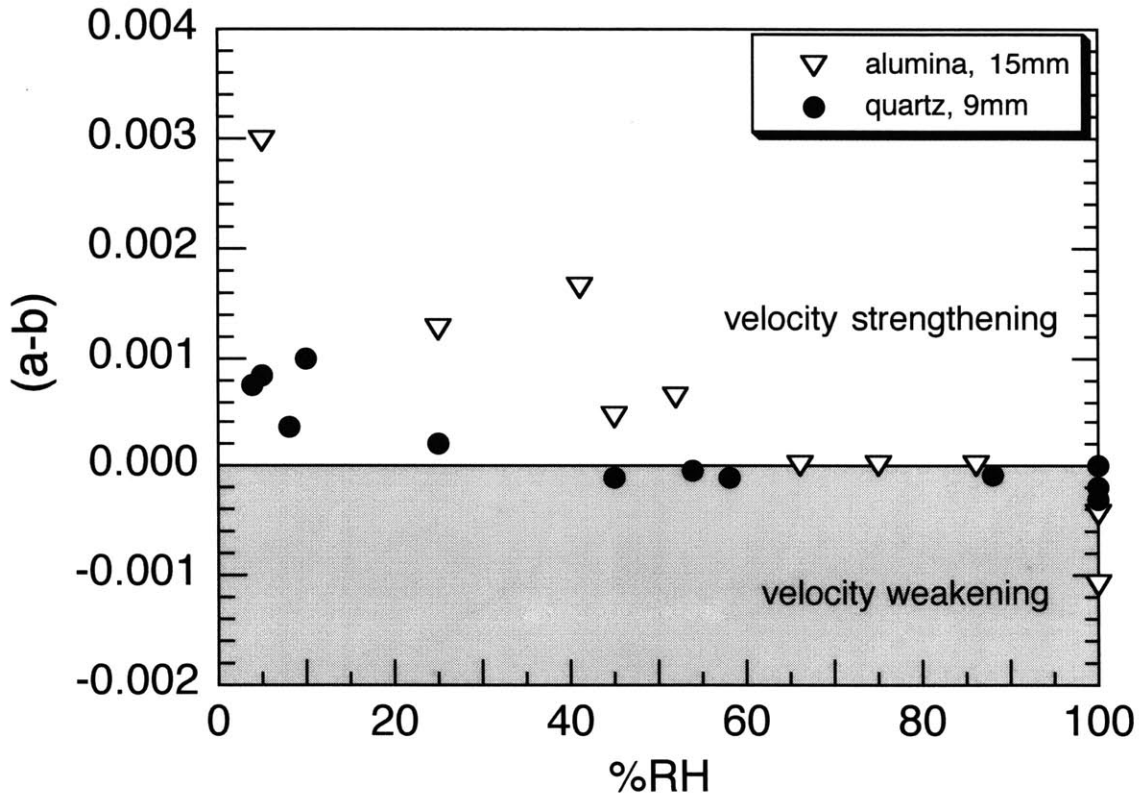

Figure 2.16. Friction exhibits velocity strengthening behavior at low humidity for both quartz and alumina powders. A transition to velocity neutral or velocity weakening behavior occurs at ~35% RH for quartz and ~65% RH for alumina. Alumina exhibits a greater humidity dependence of (a-b) than quartz.

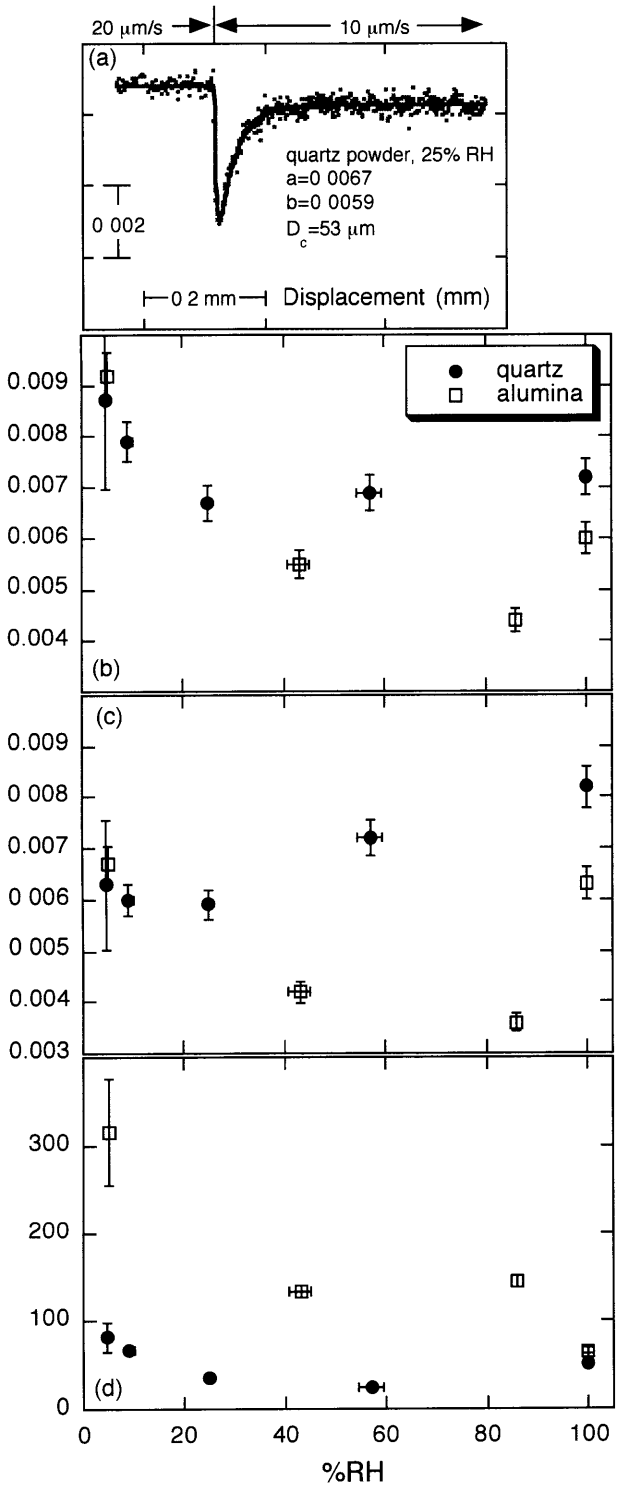

Figure 2.17. The velocity dependence of quartz and alumina powder was modeled using the Dieterich [1978, 1979] formulation of the rate- and state- friction law. (a) Raw data and model fit for a 20 μm/s to 10 μm/s velocity step shown for quartz powder at 55% RH. (b) The model parameter a is plotted vs. RH for alumina and quartz samples. (c) The model parameter b is plotted vs. RH at the same scale as 17b. (d) The parameter D_c, the critical slip distance, is plotted vs. RH.

2.4. Discussion

2.4.1. Mechanisms of Frictional Aging

Compaction and dilation of granular layers are greatest at very low and very high RH (Figure 2.11). Reduced time-dependent strengthening may increase compaction at low RH; the mechanism responsible for enhanced compaction at high RH is unclear. The RH-dependence of compaction and dilation does not appear to be related to frictional healing (Figures 2.9 and 2.10), precluding the use of entirely mechanical packing arguments to explain the observed healing data and its RH dependence.

Our observations show that time-dependent frictional healing can be reduced or eliminated at low RH. Healing rates for quartz powder approach a constant value above 50% RH, while frictional healing rates in alumina are at a maximum under saturated conditions. These observations suggest a water-assisted, time-dependent healing mechanism that can effectively be turned off at low RH. Possible water-dependent mechanisms include capillary bridging, pressure solution, hydrolytic weakening of contacts, elastic weakening due to subcritical crack growth, desorption of water at contacts, and hydrogen bonding between adsorbed water.

2.4.1.1. Quartz powder

Capillary bridging, a process through which surface water connects and adheres solids, enhances frictional aging in low normal stress applications. Bridging is a time-dependent, thermally activated process [*Bocquet et al.*, 1998] and is important in systems such as sandpiles [*Hornbaker et al.*, 1997; *Halsey and Levine*, 1998]. However, the strength of capillary bridges is small compared to the expected contact stresses for quartz of 1-10 GPa [*Scholz and Engelder*,

1976; *Teufel and Logan*, 1978; *Boitnott et al.*, 1992; *Dieterich and Kilgore*, 1996]. Moreover, if capillary bridging were important, we would expect to see a discontinuity in healing rate at 100% RH because bridges do not form under saturated conditions on quartz. Instead, we observe that frictional aging is continuous as a function of RH through saturated conditions.

We varied the salinity of the saturating solution from distilled water to 1 M NaCl in a suite of 100% RH experiments. Even at room temperature, that variation should be enough to change the dissolution rate for quartz by orders of magnitude [*Dove and Elston,* 1992; *Dove,* 1994]. However, there was little healing variation observed in the 100% RH experiments. Therefore, it is unlikely that dissolution-controlled processes such as pressure solution are responsible for increasing the real area of contact at grain-grain contact junctions.

Reduction of elastic stiffness due to subcritical crack growth is a possible means through which real area of contact could grow. However, it is unclear that large changes in stiffness could be attained in the very localized regions about asperities. Further, with displacement and comminution, shear zones contain smaller grains with smaller flaws. Therefore, subcritical crack growth should become less effective as a healing mechanism with reduction of average grain size. This is inconsistent with observations that healing rate increases with net shear displacement [*Richardson and Marone*, 1999].

We propose that the humidity dependence observed in our experiments is due to adsorption of water onto the surfaces of quartz particles. The water could enable hydrolytic weakening and contact area growth, or time-dependent contact strengthening through either hydrogen bonding or desorption mechanisms [e.g., *Rice and Hirth*, 1980; *Dieterich and Conrad*, 1984; *Michalske and Fuller,* 1985]. The frictional healing rate of quartz becomes nearly

constant at RH>50%, which is the humidity at which quartz surfaces become completely covered with a water monolayer [*Whalen*, 1981; *Michalske and Fuller,* 1985].

2.4.1.2. Alumina powder

Gates et al. [1989] found layers of weak aluminum oxide hydroxide on blocks of aluminum oxide after sliding tests. At high stresses, temperature fluctuations at contact points become high enough to form γ-Al_2O_3 from α-Al_2O_3. We do not know the RH at which a monolayer of water covers α-Al_2O_3 or γ-Al_2O_3, but in the presence of water, γ-Al_2O_3 is more easily hydroxylated than α-Al_2O_3, and a weak surface layer is created. This surface layer could deform plastically at contact junctions in the manner described by *Dieterich and Kilgore* [1994]. Thus, we propose that the frictional behavior of alumina powder is dependent on contact area growth at water-weakened contact junctions. In both quartz and alumina powder experiments, the role of RH in sample consolidation appears minor compared to its role in contact junction strengthening processes.

2.4.2. Normal stress vibrations

Compaction rates during vibrated SHS tests were approximately doubled and frictional healing was greater than in constant normal stress tests performed at the same RH. Thus, there is either an additional healing mechanism associated with vibration or a single healing mechanism is enhanced by the normal stress vibrations. We propose that there are two healing mechanisms present, one that is water-assisted and one that is strictly microstructural, perhaps due to consolidation and redistribution of localized shear (Figure 2.18). If true, then the healing present at 5% RH represents the effect of the normal stress vibrations, as there was negligible water-

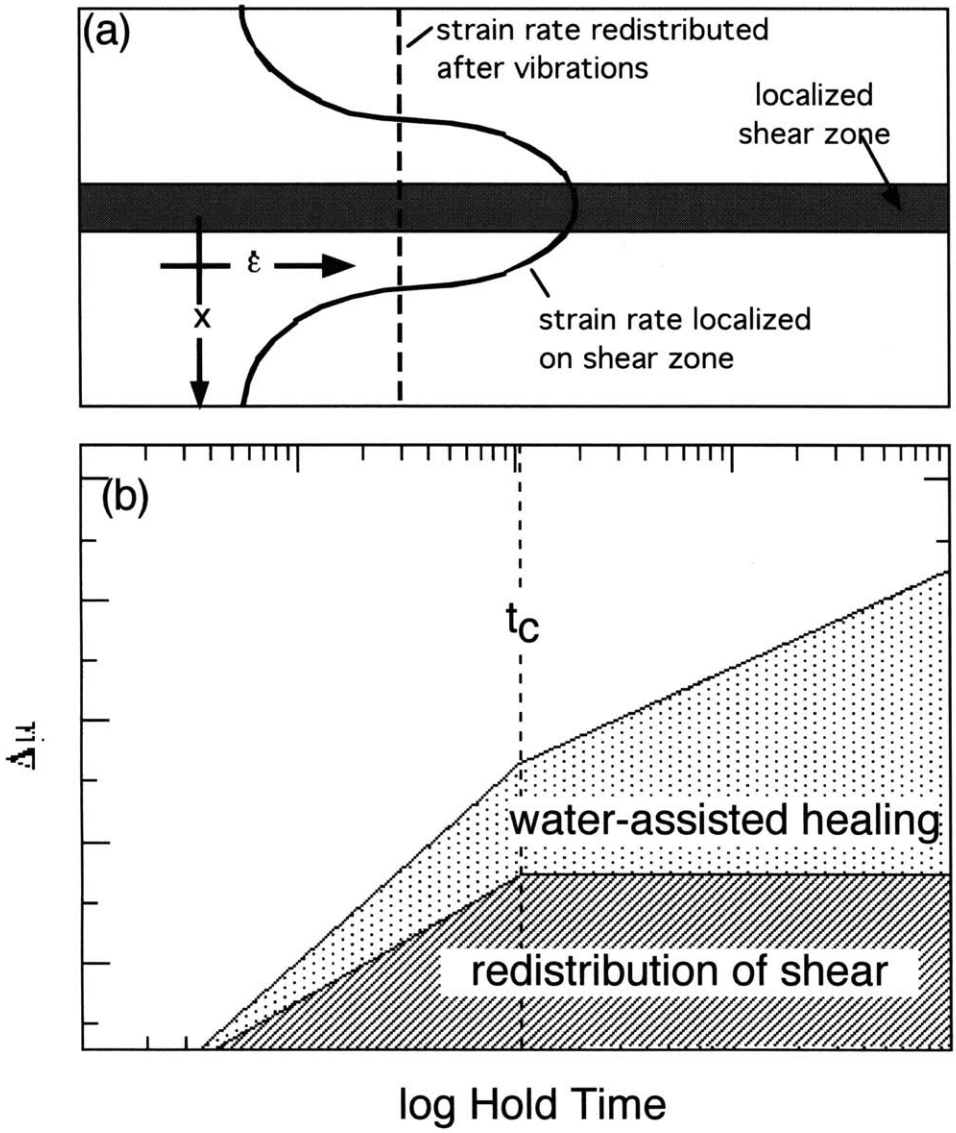

Figure 2.18. (a) Schematic diagram showing an idealized granular layer with a region of localized shear [after Sleep et al., 2000]. Strain rate is highest within the localized zone. Normal stress vibration during holds disrupts strain rate localization and effectively delocalizes shear. This cartoon shows the idealized case of complete strain rate delocalization during a vibrated SHS test. (b) A schematic interpretation of humidity-dependent healing in SHS tests (e.g., Figure 12). For a granular layer of finite thickness, a critical time (t_c) is needed to redistribute shear at a given vibration amplitude and frequency. Therefore, for dry conditions, healing due to shear redistribution saturates for hold times greater than t_c. At moderate humidity, an additional water-assisted healing mechanism produces increased healing.

assisted healing observed for dry conditions under constant normal stress. We suggest that the microstructural healing is due to the redistribution of localized strain rate [*Sleep et al.*, 2000]. Because our layers have finite overall width, there is a practical limit to possible redistribution of strain rate. Therefore, healing rate would be expected to change when that limit is reached, in this case after 100 s vibration of double amplitude ~3.5 MPa (Figure 2.12).

If healing measured at RH<5% is due exclusively to the redistribution of strain rate, then it may be subtracted from higher humidity healing to yield the purely water-assisted component of healing. We perform this operation on both constant normal stress and normal stress oscillation data at 45% RH and plot the double-difference data versus hold time (Figure 2.19). The slopes of the best-fit lines are identical to within 1%, yielding the same water assisted healing rates. Further, after subtracting out the 5% RH data, there is no slope change in the normal stress oscillation healing. We suggest that an offset on the log time axis occurs because the average contact junction lifetime is reduced by the enhanced consolidation (and particle movement) associated with normal stress vibration. Thus, we favor the interpretation that two separate mechanisms cause healing in granular gouge: water-assisted strengthening of contact junctions and redistribution of strain rate throughout the granular layer, with the first being dominant in cases of negligible alteration of normal stress.

2.4.3. Friction Velocity Dependence

We observe a transition from velocity strengthening to velocity weakening with increasing humidity for both quartz and alumina (Figure 2.15). Velocity dependence is in part a function of displacement: at 5 mm the layers exhibit velocity-strengthening behavior at all RH and there is a transition to velocity-weakening as shear becomes localized [*Marone*, 1998a, *Mair*

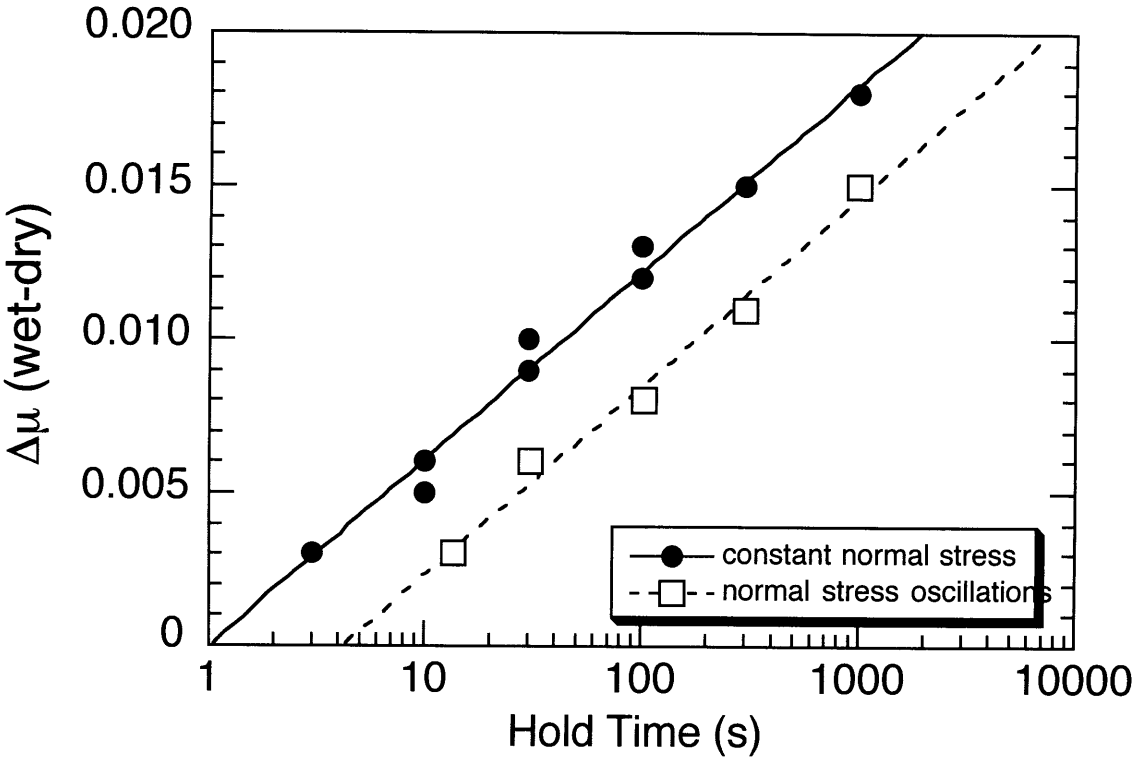

Figure 2.19. Frictional healing for the water-assisted mechanism. $\Delta\mu$ (wet-dry) is determined by subtracting dry healing data (representing microstructural effects) from humid data (representing microstructural plus contact junction strengthening). Data are shown for constant normal stress and vibrated SHS tests. Lines are best-fit log-linear healing rates and the slopes are the same to within 1%. We proposed that constant normal stress data are stronger and time shifted due to the shorter average contact lifetimes in vibrated tests where granular reorganization is greater.

and Marone, 1999]. After shear localization, rate-dependent behavior is strongly influenced by RH.

SHS tests demonstrate that healing rate, and hence the empirical parameter b, increases with RH. This would be consistent with a transition in velocity dependence $(a\text{-}b)$ from positive to negative values with increasing RH. However, it is important to note that examination of the raw velocity stepping data (Figures 2.14 and 2.15) and modeling (Figure 2.17) suggest that both the direct effect (parameter a) and evolution effect, b, change as a function of RH.

The evolution distance, D_c, generally decreases with increasing RH for both quartz and alumina (Figure 2.17). The values of D_c at low humidity are of the same order as the mean grain size, indicating that the mechanisms controlling velocity-dependence at low RH are acting at a scale larger than expected for contact junction processes. Thus, we posit that in the absence of water, rate-dependency of friction is likely a function of reorganization mechanisms rather than contact junction processes. The width of the localized shear zone could be changing with RH, thus affecting D_c, however our layer thickness data are such that we cannot resolve this issue at present. The dilation term α, an indicator of shear band thickness [*Marone and Kilgore*, 1993], is greatest during velocity step tests at very low humidity. This is consistent with the view that shear localization is less developed at low RH, but the variation is comparable to calculated uncertainty.

2.5. Conclusions

We have shown that humidity has a significant effect on frictional healing and velocity dependence for quartz and alumina powders at room temperature. We find a transition from velocity-strengthening to velocity-weakening frictional behavior as RH increases. The transition

occurs at 30-35% RH for quartz and 55-60% RH for alumina. Frictional healing is negligible at low humidity and increases with increasing RH for both materials. The coefficient of sliding friction is independent of humidity.

We observe that healing rate increases with increasing RH, consistent with *Dieterich and Conrad* [1984]. However, layer thickness change measured during SHS does not appear to correlate with the RH-dependence of healing data. We propose that dry SHS tests represent strictly microstructural healing and that comparing tests with and without normal stress oscillation can isolate water-assisted healing operative at high stress contact junctions.

We interpret the dependence of healing on RH to be the result of chemically-assisted mechanisms that strengthen contact junctions. Alumina forms a weak surface layer under high RH [*Gates et al.*, 1985] that may undergo time-dependent deformation. In quartz powder, if contact junctions are at the plastic yield stress, hydrolytic weakening would lead to greater asperity deformation and increased real area of contact. If asperities are in elastic contact, Hydrogen bonding and desorption of water at the contact junction are two mechanisms that would provide an RH dependent increase in quality of contact. Our observations are consistent with the view that rate and state friction effects in quartz derive from a thermally activated mechanism that operates at room temperature.

2.6. References for chapter 2

Beeler, N. M., T. E. Tullis, and J. D. Weeks, The roles of time and displacement in evolution effect in rock friction, *Geophys. Res. Lett.*, *21*, 1987-1990, 1994.

Blacic, J. D., and J. M. Christie, Plasticity and hydrolytic weakening of quartz single crystals, *J. Geophys. Res.*, *89*, 4223-4240, 1984.

Bocquet, L., E. Charlaix, S. Ciliberto, and J. Crassous, Moisture-induced ageing in granular media and the kinetics of capillary condensation, *Nature*, *396*, 735-737, 1998.

Boettcher, M., and C. Marone, Stability and strength of a laboratory shear zone under normal stress vibrations, *Eos. Trans. AGU, Spring Meet. Suppl.*, Abstract #T61A-01, 2001.

Boitnott, G. N., R. L. Biegel, C.H. Scholz, N. Yoshioka, and W. Wang, Micromechanics of rock friction 2: Quantitative modeling of initial friction with contact theory, *J. Geophys. Res.*, *97*, 8965-8978, 1992.

Bos, B., C.J. Peach and C.J. Spiers, Frictional-viscous flow of simulated fault gouge caused by combined effects of phyllosilicates and pressure solution, *Tectonophys.*, *327*, 173-194, 2000.

Bowden, F. P. and D. Tabor, The friction and lubrication of solids. Part II. Oxford: Clarenden Press, 1964.

Chester F.M. Effects of temperature on friction: constitutive equations and experiments with quartz gouge, *J. Geophys. Res.* 99, 7247-61, 1994.

Costin, L. S., Time-dependent deformation and failure, *in Fracture Mechanics of Rock,* edited by B. K. Atkinson, Academic Press, Inc., London, 167-215, 1987.

Crassous, J., E. Charlaix, and J. –L. Loubet, Capillary condensation between high-energy surfaces. An experimental study with a surface force apparatus, *Europhysics Letters*, *28*(1), 37-42, 1994.

deGennes, P. G., Granular matter: a tentative view, *Reviews of Modern Physics*, *71* (2), 374-382, 1999.

Dieterich, J. H., Time-dependent friction in rocks, *J. Geophys. Res.*, *77*, 3690-3697, 1972.

Dieterich, J. H., Time-dependent friction and the mechanics of stick-slip, *Pure Appl. Geophys., 116*, 790-805, 1978.

Dieterich, J. H., Modeling of rock friction: 1. Experimental results and constitutive equations, *J. Geophys. Res., 84,* 2161-2168, 1979.

Dieterich, J. H., and G. Conrad, Effect of humidity on time and velocity-dependent friction in rocks, *J. Geophys. Res., 89,* 4196-4202, 1984.

Dieterich, J. H., and B. Kilgore, Direct observation of frictional contacts: new insights for state-dependent properties, *Pure Appl. Geophys., 143*, 283-302, 1994.

Dieterich, J. H., and B. Kilgore, Imaging surface contacts: power law contact distributions and stresses in quartz, calcite, glass and acrylic plastic, *Tectonophys., 256*, 219-239, 1996.

Dove, P. M., The dissolution kinetics of quartz in sodium chloride solutions at 25 degrees to 300 degrees C, *Amer. J. of Sci., 294* (6), 665-712, 1994.

Dove, P. M., and S. F. Elston, Dissolution kinetics of quartz in sodium chloride solutions; analysis of existing data and a rate model for 25 degrees C, *Geochimica and Cosmochimica Acta*, *56* (12), 4147-4156, 1992.

Evans, B., and D. L. Kohlstedt, Rheology of rocks, *in Rock Physics and Phase Relations, A Handbook of Physical Constants, AGU Reference Shelf 3*, edited by T. J. Ahrens, 148-165, AGU, Washington, D.C., 1995.

Evans, J. P., and F. M. Chester, Fluid-rock interaction in faults of the San Andreas system; inferences from San Gabriel Fault rock geochemistry and microstructures, *J. Geophys. Res., 100*, 13007-13020, 1995.

Gates, R. S., S. M. Hsu, and E. E. Klaus, Tribochemical mechanism of alumina with water, *Tribology Trans., 32*, 357-363, 1989.

Geminard, J.–C., W. Losert, and J.P. Gollub, Frictional mechanics of wet granular material, *Phys. Rev. E, 59*, 5881-5890, 1990.

Halsey, T.C., and A. J. Levine, How sandcastles fall, *Physical Review Letters, 80* (14), 3141-3144, 1998.

Heslot, F., Baumberger, T., Perrin, B., Caroli, B., and C. Caroli, Creep, stick-slip, and dry-friction dynamics: experiments and a heuristic model. *Phys. Rev. E, 49*, 4973-88, 1994.

Hirth, J.P. and J.R. Rice, On the thermodynamics of adsorption at interfaces as it influences decohesion, *Metallurgical Trans. A 11*, 1501-1511, 1980.

Hornbaker, D. J., R. Albert, I. Albert, A.–L. Barabasi, and P. Schiffer, What keeps sandcastles standing?, *Nature, 387*, 765, 1997.

Iwamatsu, M., and K. Horii, Capillary condensation and adhesion of two wetter surfaces, *Journal of Colloid and Interface Science, 182*, 400-406, 1996.

Jaeger, H. M., S. R. Nagel, and R. P. Behringer, Granular solids, liquids and gases, *Reviews of Modern Physics, 68* (4), 1259-1273, 1996.

Jaoul, O., J. Tullis, and A. K. Kronenberg, The effect of varying water contents on creep behavior of Heavitree quartzite, *J. Geophys. Res., 89*, 4298-4312, 1984.

Karner, S. L., and Marone, C., Effects of loading rate and normal stress on stress drop and stick-slip recurrence interval, in *Geocomplexity and the Physics of Earthquakes*, edited by J. B. Rundle, D. L., Turcotte, and W. Klein, AGU Geophysical Monograph Series, *Vol. 120*, 187-198, 2000.

Karner, S. L., and Marone, C., Frictional restrengthening in simulated fault gouge: Effect of shear load perturbations, *J. Geophys. Res., 106*, 19319-19337, 2001.

Kronenberg, A. K., and J. Tullis, Flow strengths of quartz aggregates: Grain size and pressure effects due to hydrolytic weakening, *J. Geophys. Res.*, *89*, 4281-4297, 1984.

Mainprice, D. H., and M. S. Paterson, Experimental studies of the role of water in the plasticity of quartzites, *J. Geophys. Res.*, *89*, 4257-4270, 1984.

Mair, K., and C. Marone, Friction of simulated fault gouge for a wide variety of velocities and normal stresses, *J. Geophys. Res.*, *104*, 28899-28914, 1999.

Marone, C., Laboratory-derived friction laws and their application to seismic faulting, *Annu. Rev., Earth Planet. Sci.*, *26*, 696, 1998a.

Marone, C., The effect of loading rate on static friction and the rate of fault healing during the earthquake cycle, *Nature, 391,* 69-72, 1998b.

Marone, C., and B.D. Kilgore, Scaling of the critical slip distance for seismic faulting with shear strain in fault zones, *Nature*, *362*, 618-621, 1993.

Marone, C., Raleigh, C. B., and C. H. Scholz, Frictional behavior and constitutive modeling of simulated fault gouge, *J. Geophys. Res.*, *95*, 7007-7025, 1990.

Martin, R. J., and W. B. Durham, Mechanisms of crack growth in quartz, *J. Geophys. Res.*, *80*, 4837-4844, 1975.

Michalske, T. A., and E. R. Fuller, Jr., Closure and repropagation of healed cracks in silicate glass, *J. Amer. Ceramic Soc.*, *68*, 5586-5590, 1985.

Mora, P., and D. Place, Numerical simulation of earthquake faults with gouge: toward a comprehensive explanation for the heat flow paradox, *J. Geophys. Res.*, *103*, 21067-21089, 1998.

Morgan, J. K., Numerical simulations of granular shear zones using the distinct element method, 2: Effects of particle size distribution and interparticle friction on mechanical behavior, *J. Geophys. Res.*, *104*, 2721-2732, 1999.

Morgan, J. K., and M. S. Boettcher, Numerical simulations of granular shear zones using the distinct element method, 1: Shear zone kinematics and the micromechanics of localization, *J. Geophys. Res.*, *104*, 2703-2719, 1999.

Rabinowicz, E., The nature of static and kinetic coefficients of friction, *J. Appl. Phys. 22*, 1373-1379, 1951.

Rice, J.R., Hydrogen and interfacial cohesion, in *Effect of Hydrogen on Behavior of Materials*, ed. A.W. Thompson and I.M. Berstein, Metallurgical Society of AIME, New York, 455-466, 1976.

Richardson, E., and C. Marone, Effects of normal stress vibrations on frictional healing, *J. Geophys. Res.*, *104*, 28859-28878, 1999.

Ruina, A., Slip instability and state variable friction laws, *J. Geophys. Res.*, *88*, 10359-10370, 1983.

Sammis, C.G., G. King, and R. Biegel, The kinematics of gouge deformation, *Pure Appl. Geophys.*, *125*, 777-812, 1987.

Scholz, C.H., Earthquakes and friction laws, *Nature*, *391*, 37-42, 1998.

Scholz, C. H., and J. T. Engelder, The role of asperity indentation and ploughing in rock friction; I, Asperity creep and stick-slip, *International Journal of Rock Mechanics and Mining Sciences*, *13*, 149-154, 1976.

Segall, P., and J. R. Rice, Dilatancy, compaction, and slip instability of a fluid-infiltrated fault, *J. Geophys. Res.*, *100*, 22155-22171, 1995.

Sleep, N. H., E. Richardson, and C. Marone, Physics of friction and strain rate localization in simulated fault gouge, *J. Geophys. Res.*, *105*, 25875-25890, 2000.

Sleep, N. H., Application of a unified rate and state friction theory to the mechanics of fault zones with strain localization, *J. Geophys. Res.*, *102*, 2875-2895, 1997.

Teufel, L. W., and J. M. Logan, Effect of displacement rate on the real area of contact and temperatures generated during frictional sliding of Tennessee sandstone, *Pure Appl. Geophys.*, *116*, 840-865, 1977.

Thornton, C., Numerical simulations of deviatoric shear deformation of granular media, *Geotech., 50 (1),* 43-53, 2000.

Tullis, T. E., Rock friction constitutive behavior from laboratory experiments and its implications for an earthquake prediction field monitoring program, *Pure Appl. Geophys.*, *126*, 555-588, 1988.

Tullis, T. E., and J. D. Weeks, Constitutive behavior and stability of frictional sliding of granite, *Pure Appl. Geophys., 124*, 383-414, 1986.

Whalen , J.W., Thermodynamic properties of water adsorbed on quartz, *J. Phys. Chem., 65*, 1676-81, 1981.

Wong, T. -f., Y. Gu, T. Yanagidani, and Y. Zhao, Stabilization of faulting by cumulative slip, in *Fault mechanics and transport properties of rocks; a festschrift in honor of W. F. Brace*, Evans, B. and T. -f. Wong (editors), 119-143, 1992.

Table 2.1. Experiments from chapter 2. All experiments were performed at T=24° C (±1.5° C).

Experiment	*Material*	*Humidity*	*Saturating Solution*	σ_n *Oscillations (Double Amplitude)*
m304	quartz-powder	55%	—	—
m307	quartz-powder	5%	—	—
m308	quartz-powder	8%	—	—
m309	quartz-powder	25%	—	—
m310	quartz-powder	60%	—	—
m311	quartz-powder	10%	—	—
m312	quartz-powder	5%	—	—
m314	quartz-powder	4%→100%	DI water	—
m318	quartz-powder	45%	—	—
m321	quartz-powder	88%	—	—
m340	quartz-powder	45%	—	2A = 3.55 MPa
m341	quartz-powder	4%	—	2A = 3.53 MPa
m377	quartz-powder	100%	DI water	—
m378	quartz-powder	100%	1 M NaCl	—
m404	alumina-powder	25%	—	—
m424	alumina-powder	100%	tap water	—
m427	alumina-powder	75%	—	—
m430	alumina-powder	41%	—	—
m432	alumina-powder	45%	—	—
m434	alumina-powder	52%	—	—
m435	alumina-powder	86%	—	—
m436	alumina-powder	66%	—	—
m438	alumina-powder	5%	—	—
m450	alumina-powder	100%	DI water	—
m453	quartz-powder	100%	0.1 M NaCl	—

3. The effects of humidity and normal stress on the friction behavior of quartz powder and Westerly granite

Synopsis. We further investigate the processes that result in rate- and state-dependent friction behavior by examining the effect of humidity and normal stress on the friction behavior of heterogeneous materials and quartz powder. We perform slide-hold-slide (SHS) tests on clean Westerly granite surfaces and layers of Westerly granite powder at a range of relative humidities (5-100%) and normal stresses (5-45 MPa). We find that healing increases with increasing humidity, consistent with the idea of a chemically assisted contact junction aging mechanism. To investigate the normal stress dependence of this aging mechanism, we perform velocity stepping tests on quartz powder at different values of applied normal stress (5 to 45 MPa) after pre-conditioning at high normal stress (40 and 35 MPa). Velocity stepping tests require the use of a 2 state variable friction law to accurately model rate- and state-friction behavior for powders, and we find that the parameter b_1 decreases with increasing normal stress. We also perform SHS tests and observe humidity dependent healing at normal stresses down to 5 MPa. At a given humidity, time-dependent frictional healing decreases with increasing normal stress for quartz powder, granite powder, and granite blocks (over a limited normal stress range of 5 to 20 MPa), consistent with the rate and state friction parameters from velocity stepping tests.

3.1. Background

Rate- and state-dependent friction laws were developed to describe laboratory observations of time-dependent frictional strengthening and velocity-dependent sliding friction [*Dieterich*, 1972, 1978, 1979; *Ruina*, 1983; *Tullis and Weeks*, 1986; *Chester*, 1994; *Beeler et al.*, 1994; *Marone* 1998a]. These laws can describe the variety of friction behavior observed in natural fault zones and in the laboratory [see *Marone*, 1998a; *Scholz*, 1998], but the microphysical processes that result in rate- and state-dependent friction behavior for granular materials remain poorly understood. Laboratory studies indicate that asperity contact junctions strengthen with age [*Rabinowicz*, 1951], possibly through thermally activated mechanisms that increase the contact area [*Dieterich and Kilgore*, 1994; 1996;] or the contact bonding quality [*Rice*, 1976; *Hirth and Rice*, 1980]. Additionally, the friction behavior of granular materials is a function of shear localization, density changes, and particle characteristics [*Mair and Marone*, 1999; *Mair et al.*, 2002].

Dieterich and Conrad [1984] and *Frye and Marone* [2002] show that for quartzite blocks, quartz powder and alumina powder, friction behavior is dependent on relative humidity (RH). Time-dependent frictional healing is reduced or turned off at low RH, indicating that at least one of the mechanisms responsible for rate- and state-dependent friction is chemically assisted. In this paper we build upon earlier laboratory work [*Dieterich and Conrad*, 1984; *Tullis and Weeks*, 1986; *Blanpied et al.*, 1998; *Frye and Marone*, 2002] and report results from experiments performed at different applied normal stress to investigate whether the underlying water-assisted aging mechanisms are normal stress dependent. Further, we investigate the RH dependence of friction behavior for a heterogeneous material (Westerly granite). Finally, *Dieterich and Conrad* [1984] found that steady state sliding friction decreased with increasing

RH for quartzite blocks while the powders investigated by *Frye and Marone* [2002] exhibited no variation in sliding friction as a function of RH. We address this discrepancy by examining the steady-state sliding friction as a function of RH for powders and blocks made of the same material.

3.2 Experiment procedure

All laboratory experiments in this study were performed in a double-direct shear apparatus. In this configuration, two frictional surfaces are sheared simultaneously (Figure 3.1, inset). Shear load was applied as a vertical displacement or velocity boundary condition by servo-control with 0.1 μm resolution. The horizontal ram applied normal force in load-feedback mode with 0.1 kN resolution. Position and applied force are measured at each load point at a sampling rate of 1 to 10 kHz. The raw data is averaged and recorded at 1 to 10 samples/s.

3.2.1 Technique for powders

Test samples consisted of 3 mm-thick layers of quartz or Westerly granite powder sheared between grooved steel forcing blocks. The nominal area of contact was 10 cm x 10 cm. Gouge layers were constructed in a leveling jig to ensure uniform and reproducible layer thickness, as in chapter 2.

The quartz powder was subangular Ottawa sand, which is >99% SiO_2 as supplied by the US Silica Co. We used Natural Grain product F-110, which has an initial median particle size of 110 μm and a size range of 50-150 μm. The granite powder came from Westerly granite blocks (Westerly, RI) that were jaw-crushed and disk-milled to a size range of 10-150 μm, with a median size of ~25 μm. The powders were dried in a vacuum oven at 110° C to remove excess

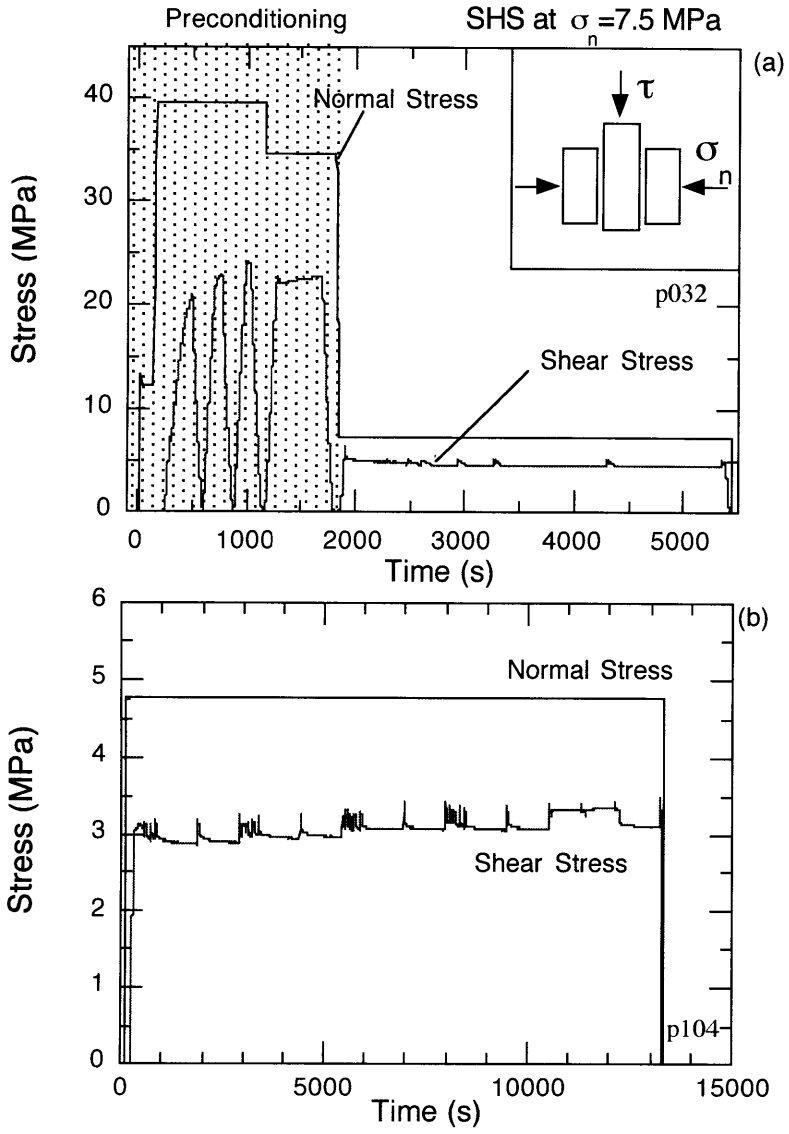

Figure 3.1. Shear stress and normal stress history for two experiments. (a) Gouge layers are subject to three shear load cycles at high normal stress (40 MPa) to create fresh surface area before velocity stepping tests are carried out at normal stress 35 MPa. In this experiment, normal stress is dropped to 7.5 MPa for slide-hold-slide tests after gouge layer preconditioning. (b) Bare surface test with Westerly granite blocks: normal stress is constant for the entire experiment.

surface water. *Brace* [1965] reported Westerly granite composition to be 28% quartz, 35% Potassium feldspar, 31% plagioclase feldspar, and 5% micas.

The test sample and loading system were isolated from room atmosphere with a flexible membrane and RH was varied from <5% to 100% (Table 3.1, end of chapter). To allow the granular layer to equilibrate at a given humidity, unsaturated samples were held in the controlled humidity environment for 12 hours before normal load was applied. 100% RH experiments were performed by applying water directly to the top of the samples until water flowed from the bottom of the samples.

It is not possible to reliably vary RH within a given experiment, so different experiments must be compared. To observe the effect of humidity on rate- and state- dependent friction behavior, we precondition the gouge at the beginning of experiments to help localize shear and create fresh surface area within the sample through comminution of grains. Each experiment started by raising normal stress σ_n to 40 MPa (Figure 3.1a). Three shear load cycles were performed to enhance grain crushing and produce new surface area *in situ* (Figure 3.2).

For Westerly granite powder experiments as a function of RH, normal stress was then reduced to 25 MPa and shearing was carried out at a rate of 10 μm/s. To further condition the gouge layers and establish a steady-state friction level, we performed velocity stepping experiments for the displacement range 5 to 9 mm. SHS tests were performed for the displacement interval 9 to 13 mm.

For granite and quartz powder experiments investigating the effect of normal stress, after load cycles at σ_n = 40 MPa, normal stress was reduced to 35 MPa and the sample was sheared to 9 mm net displacement. Shear stress was then removed and the normal stress was changed to a value between 5 and 45 MPa. The sample was sheared for 3 mm and SHS tests were performed.

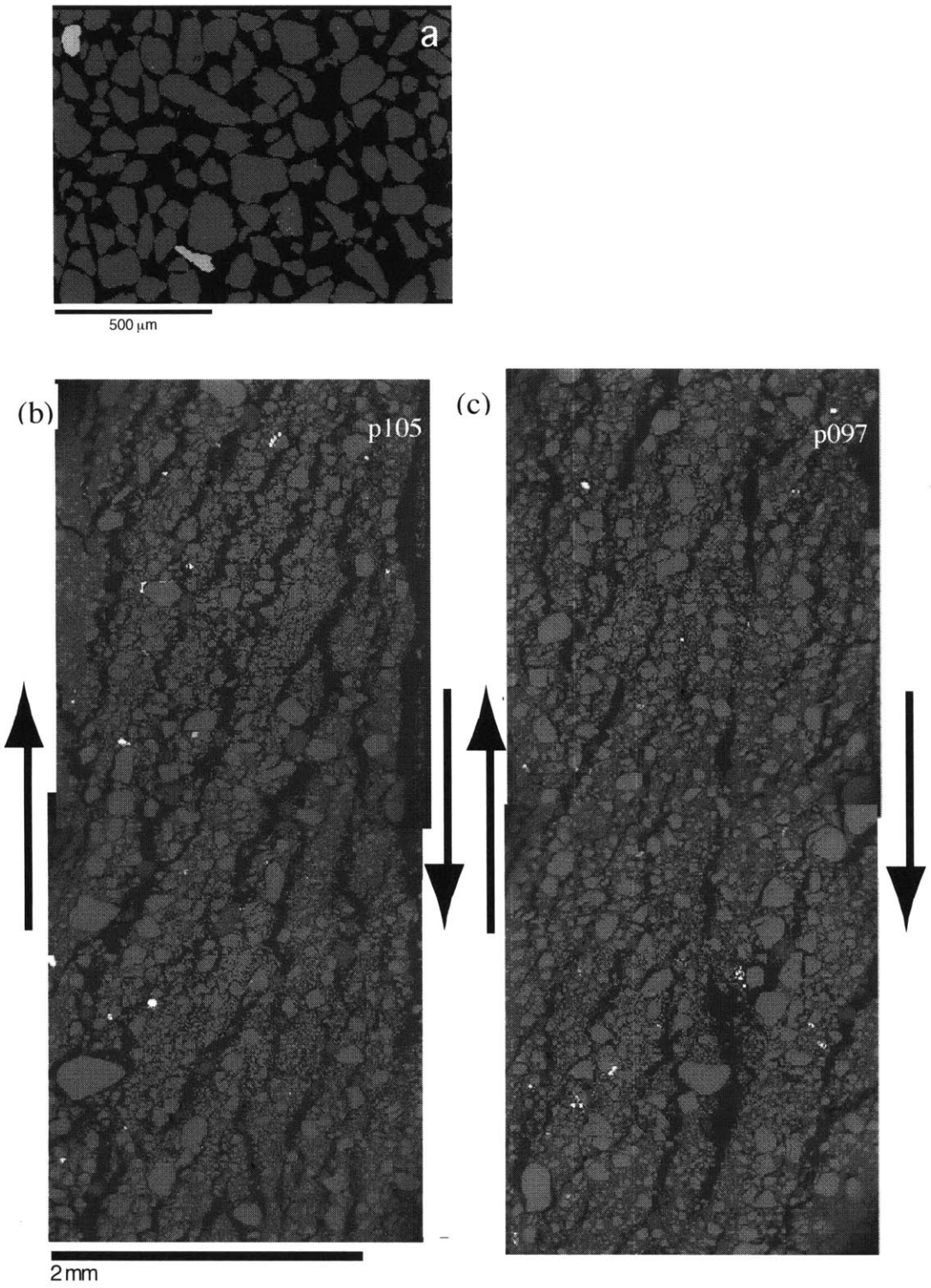

Figure 3.2. (a) Starting material for quartz powder experiments. (b) Quartz powder layer after preconditioning at σ_n = 40 MPa followed by velocity stepping at σ_n = 5 MPa. (c) Quartz powder layer after preconditioning and velocity stepping at 35 MPa. Both layers exhibit significant comminution of grains and epoxy-filled cracks formed during unloading.

3.2.2. Technique for bare surfaces

Blocks of Westerly granite with a nominal contact area of 10 cm x 10 cm were roughened by either shot-blasting or sandblasting. The blocks were dried in a vacuum oven at 110° C to remove excess surface water. Samples were assembled in a leveling jig to ensure proper alignment and allowed to equilibrate with the ambient humidity in the lab (8-36% RH) or with the air in the test chamber (75% RH). 100% RH experiments were achieved by adding water to the top of the sample interface throughout the experiment.

Normal stress was applied to the blocks (5-20 MPa), and shearing was begun. After 3 mm of shear displacement, SHS tests were performed (Figure 3.1b).

3.3. Results

3.3.1 Quartz powder

3.3.1.1. Normal stress effect on frictional healing

The time dependence of static friction is measured in the laboratory after slide-hold-slide (SHS) tests (Figure 3.3). The load point is stopped for periods of 3-1000 s after which loading resumes and a peak friction value is measured [after *Dieterich*, 1972; *Beeler et al.*, 1994; *Marone*, 1998b]. Because of the finite stiffness of the testing apparatus, frictional creep occurs during holds, accompanied by layer compaction in powders (Figure 3.3b). When loading resumes at the initial driving velocity, hardening occurs until the frictional yield strength is overcome and then friction returns to its steady state sliding value. The layer dilates to accommodate shearing. We define the difference between steady-state sliding friction and the peak friction value after a hold as healing ($\Delta\mu$).

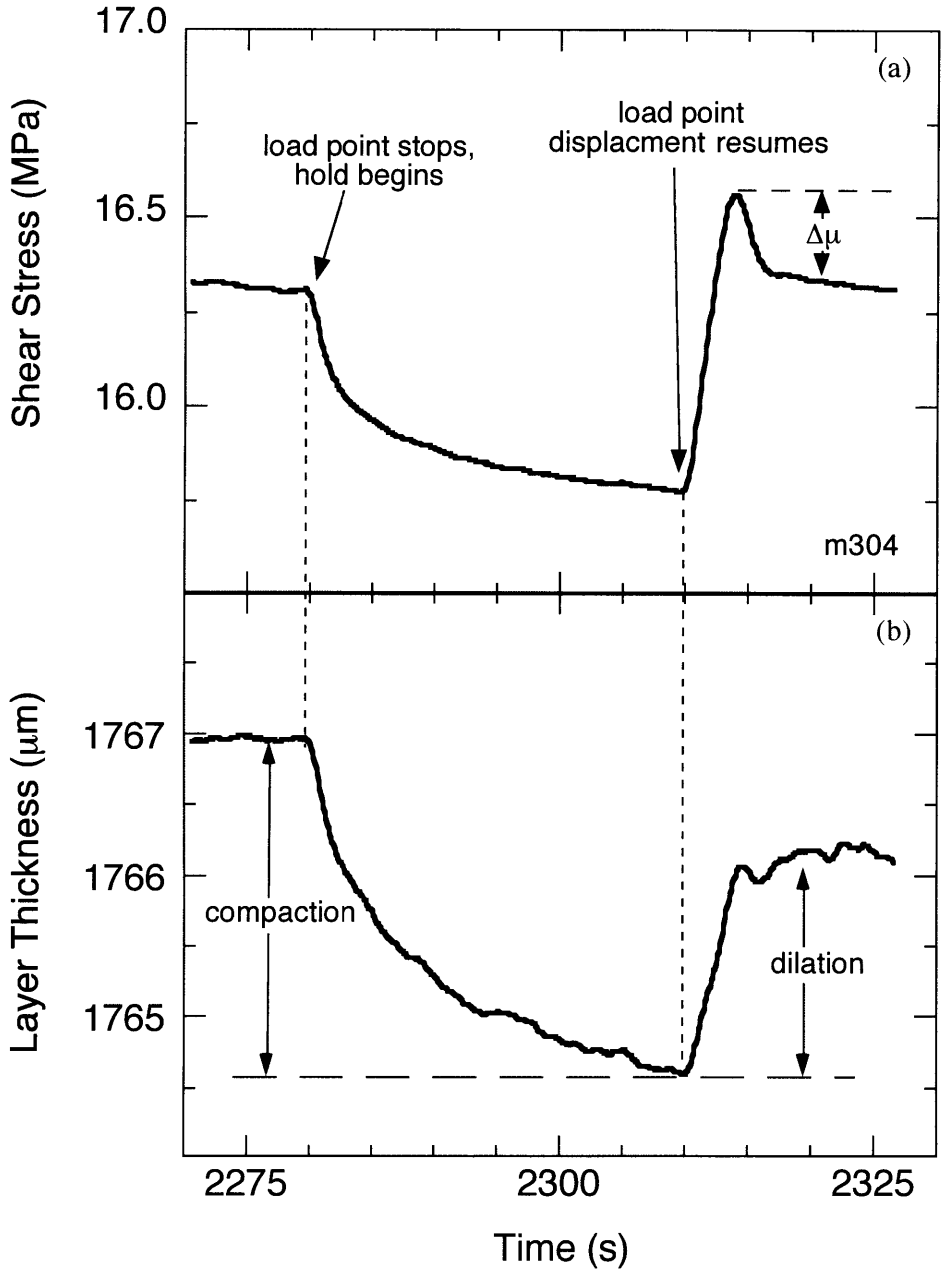

Figure 3.3. (a) A 30 s SHS test is shown with (b) corresponding layer thickness change. Compaction occurs during the hold as shear stress relaxation occurs. When loading resumes, the layer dilates to accommodate displacement.

We performed SHS tests for a range of RH and normal stress. Healing increases with increasing RH at all applied normal stresses over the range 5-45 MPa (Figure 3.4). Frictional healing for a given hold time is reduced or zero at low humidity, and increases with RH to 50-60% RH. At RH>60%, the approximate RH at which a monolayer of water exists on quartz surfaces [*Whalen*, 1981], the humidity effect saturates and healing values are approximately the same.

Figure 3.4 shows that healing at σ_n=35 MPa is less than healing observed at lower values of normal stress at a given humidity. A plot of frictional healing versus normal stress shows the normal stress dependence more clearly (Figure 3.5). At three values of RH, healing decreases with increasing applied normal stress. The normal stress dependence is most easily observed at 100% RH, where the healing signal is largest.

We are able to observe the normal stress dependence of healing because healing is defined in terms of friction. Expressed as change in shear stress after a quasi-static hold, the normal stress effect is very small (Figure 3.6), illustrating the subtlety of the healing signal. Figure 3.6b shows layer compaction and dilation associated with 1000 s SHS from σ_n=5 MPa to σ_n=45 MPa. The consistency of the layer thickness data as a function of normal stress may indicate that the shear zones developed during preconditioning are approximately the same width from experiment to experiment [*Karner and Marone*, 2001].

3.3.1.2 Normal stress effect on velocity dependence

The velocity dependence of sliding friction was measured during velocity stepping tests where the load point velocity was toggled between 10 and 1 μm/s. When velocity is decreased, friction initially decreases (direct effect). As displacement continues at the slower velocity,

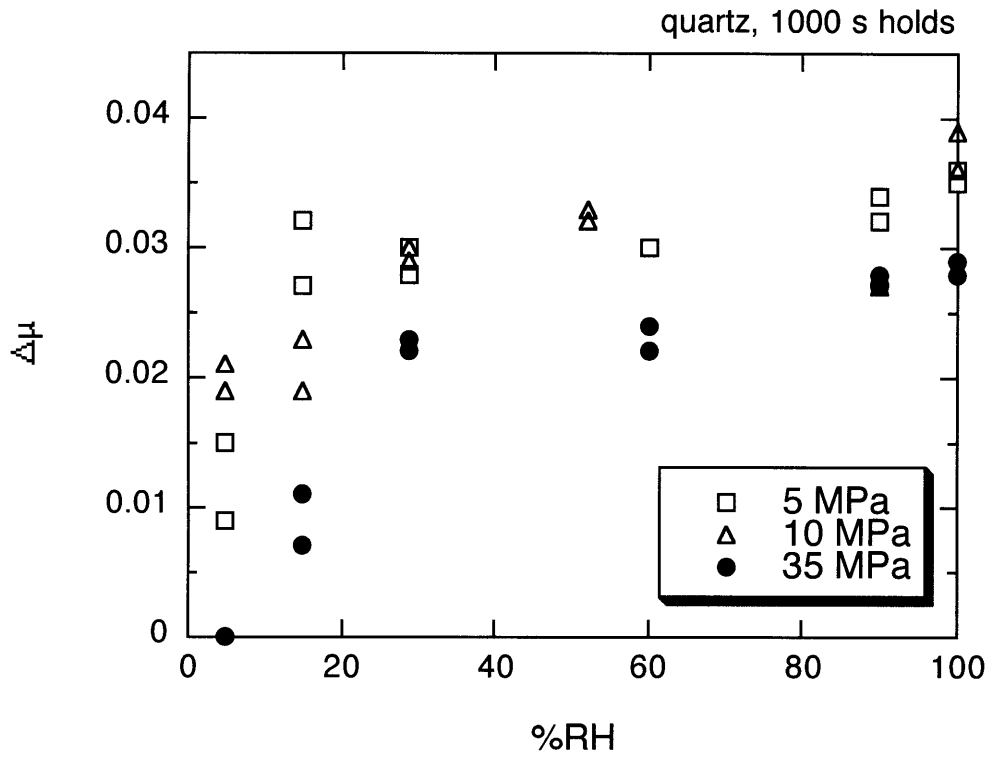

Figure 3.4. Healing versus humidity. Healing increases with %RH for tests performed at 5, 10, and 35 MPa applied normal stress. Healing at a given %RH value is reduced at 35 MPa.

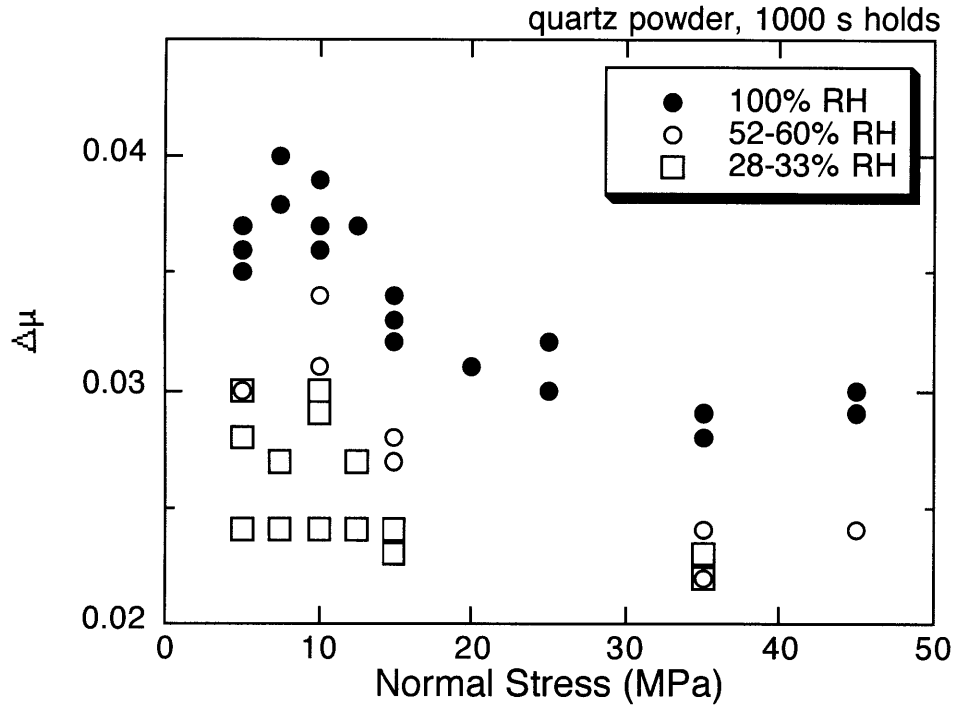

Figure 3.5. Healing versus normal stress for three different %RH ranges. Healing decreases with normal stress for quartz powder samples for any given humidity value. The trend is most clear in 100% RH samples.

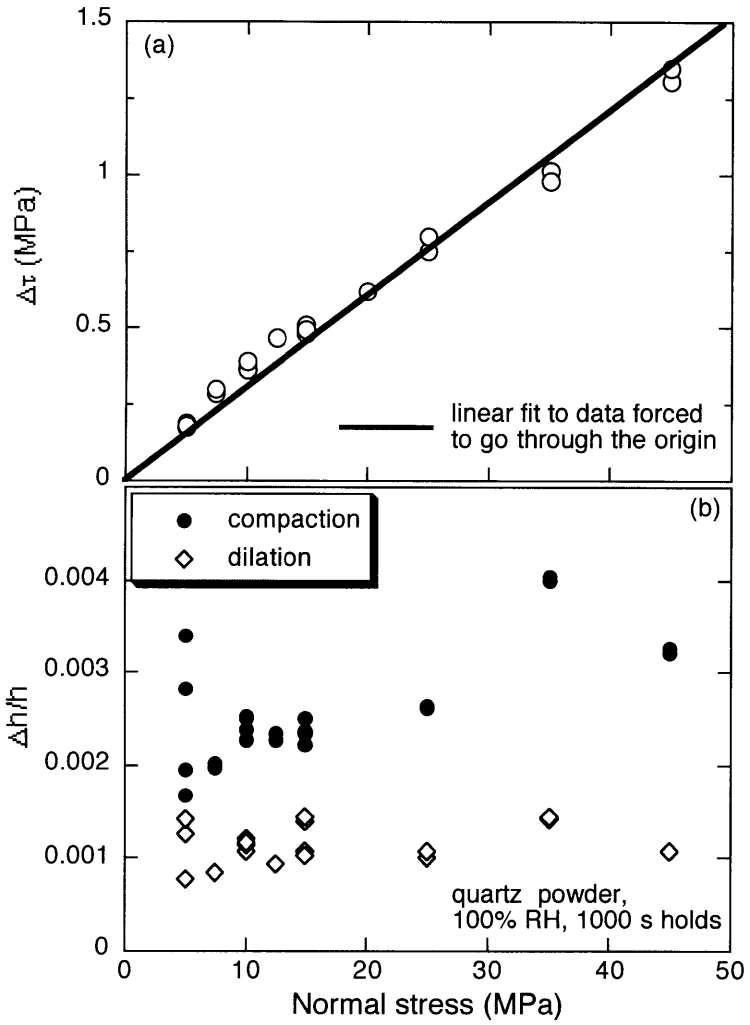

Figure 3.6. (a) Healing expressed as change in shear stress for 1000 s SHS tests of 100 % RH quartz powder. Normal stress dependence of healing is relatively small when plotted as change in shear stress. (b) Compaction and dilation data for 1000 s holds do not vary significantly with normal stress. After preconditioning, localized shear zones likely have similar widths for all tests.

friction evolves back to a steady state sliding value over a critical slip distance. In our velocity stepping tests performed after gouge preconditioning, the evolution effect occurs over two critical slip distances (Figure 3.7), necessitating the use of a two state variable rate- and state-dependent friction model [*Blanpied and Tullis*, 1986] such as:

$$\mu = \mu_0 + a\ln\left(\frac{V}{V_0}\right) + b_1\ln\left(\frac{V_0\theta_1}{D_{c1}}\right) + b_2\ln\left(\frac{V_0\theta_2}{D_{c2}}\right) \tag{3.1}$$

where μ is the new sliding friction at velocity V, μ_0 is friction at velocity V_0, D_{ci} is the critical slip distance, and θ_i is the state variable which evolves in the *Dieterich* [1978, 1979] formulation as:

$$\frac{d\theta_i}{dt} = 1 - \frac{V\theta_i}{D_{ci}} \tag{3.2}$$

Figure 3.7a illustrates why our velocity stepping tests at 10 MPa require the use of a two state variable model to fit the data. Friction decreases through the direct effect, evolves to a value significantly higher than sliding friction at 10 μm/s, and then evolves over a larger distance back down to ~0.675. The corresponding horizontal displacement data (Figure 3.7b) shows a decrease in layer thickness at the displacement where the velocity step occurs. The layer then dilates, which perturbs the friction level again. The effect of the second state variable is much more subdued at 35 MPa, and the layer thickness decreases with the decrease in velocity, consistent with *Mair and Marone* [1999].

The two state variable rate- and state- friction parameters are obtained by using an iterative, non-linear, least-squares inversion. The parameters a and b_1 decrease with normal stress, as does the absolute value of b_2 (Figure 3.8). The systematic variation of the parameters results in very little change in overall velocity dependence of steady-state friction (a-b_1-b_2). However, the parameters a and b_1 would affect the static friction peak after a SHS test more than

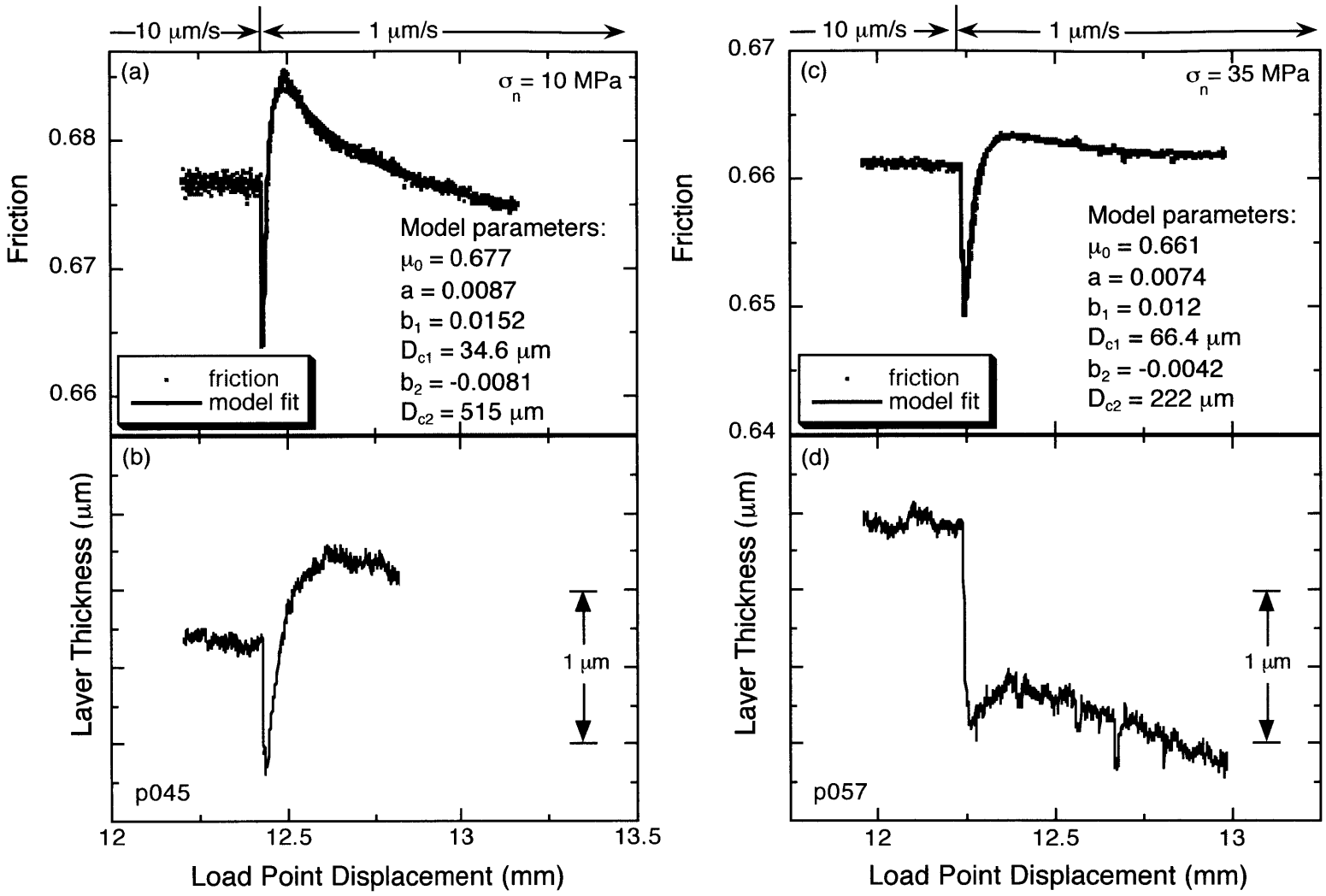

Figure 3.7. Velocity stepping tests performed at 10 MPa need a two state variable model to fit friction data (a). Layer thickness decreases with a step from 10 μm/s to 1 μm/s, then dilates (b). At 35 MPa (c), b_1 and the absolute value of b_2 are smaller than observed for low normal stress tests. (d) Layer thickness data from both experiments have been detrended to remove the effect of geometric thinning.

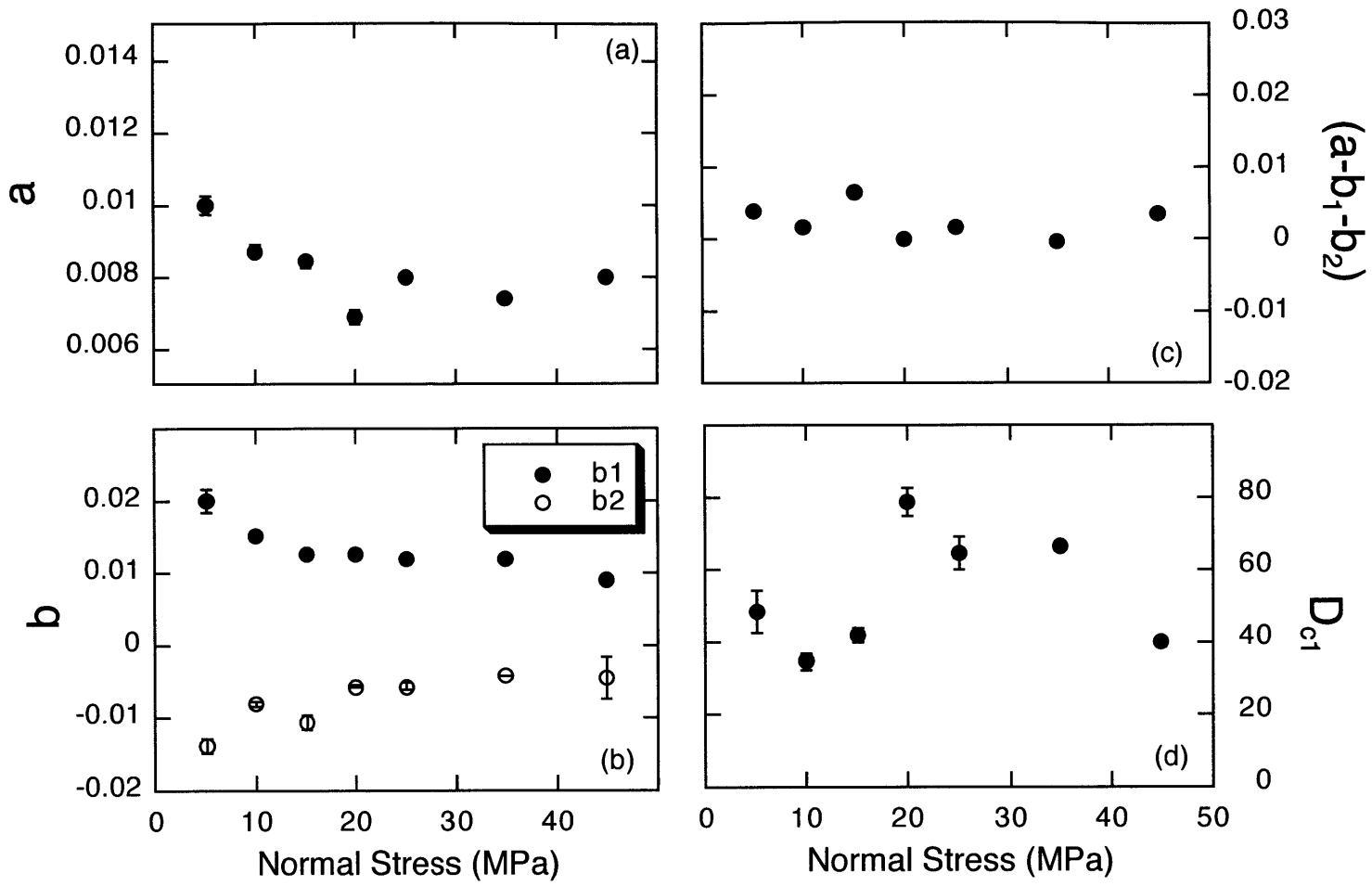

Figure 3.8. Rate and state friction parameters versus normal stress. (a) The parameter a decreases as a function of normal stress. (b) b_1 decreases with normal stress, consistent with healing data; b_2 increases with normal stress but remains negative. (c) $(a\text{-}b_1\text{-}b_2)$, the steady-state velocity dependence, is not a function of normal stress. (d) Variation of D_{c1} with normal stress is within the scatter.

the parameter b_2, which acts over a larger displacement. The normal stress dependence of a and b_1 is consistent with healing data from SHS tests (Figure 3.5).

3.3.2. Westerly granite powder and bare surfaces

3.3.2.1. Humidity effect on frictional healing and sliding friction

The frictional healing measured after SHS tests is a function of humidity for Westerly granite surfaces and powder (Figure 3.9). Healing is minimized at low RH, and reaches a maximum value at 100% RH (saturated conditions). The healing versus RH curve does not go to zero for granite powder, but for bare surfaces, healing remains zero up to 40% RH. At 100% RH healing for both powder and bare surfaces is the same. There is no systematic relationship between humidity and sliding friction for granite powder, but bare surfaces weaken with increasing humidity (Figure 3.10).

A relationship between frictional healing rate and displacement has been observed for bare surfaces and powders [*Wong et al.*, 1992; *Beeler et al.*, 1994; *Richardson and Marone*, 1999]. For powder experiments, SHS tests are performed at the same displacement in each experiment. For bare surfaces, all healing data come from the first 15 mm of displacement. There is very little gouge formed on the surfaces of granite blocks at these low displacements and there is little variation in healing over the first 15 mm of displacement (Figure 3.11).

3.3.2.2. Normal stress effect on frictional healing

Frictional healing of Westerly granite powder decreases with increasing normal stress (Figure 3.12a). The systematic variation of healing with normal stress is similar to that of quartz

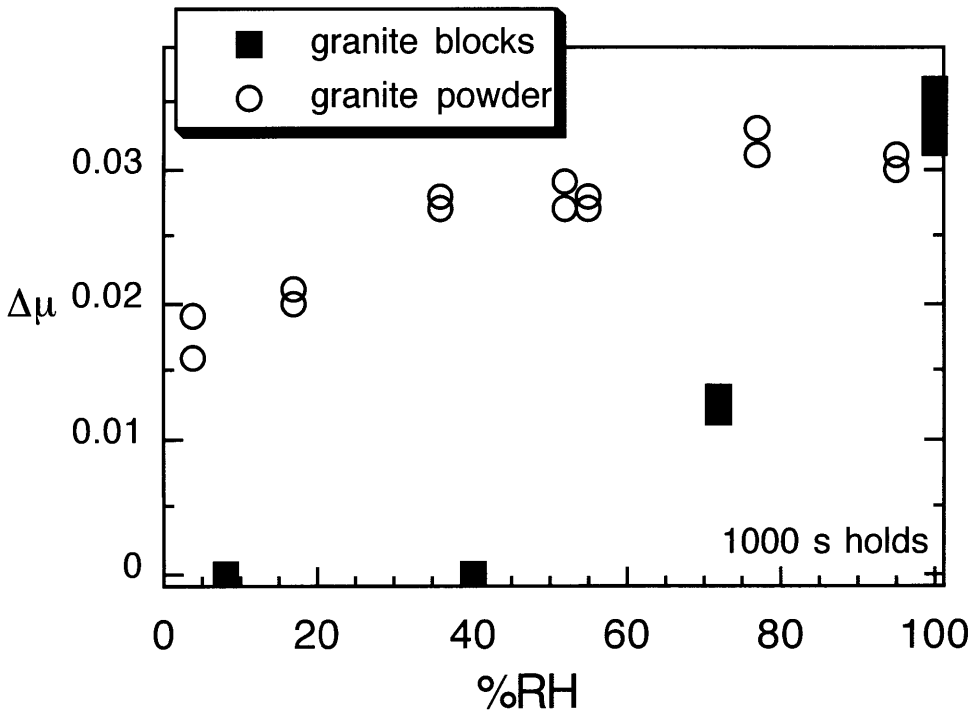

Figure 3.9. (a) Frictional healing for 1000 s holds increases with humidity for both bare surfaces and thick granular layers of Westerly granite powder. Healing goes to zero at low humidity for bare surfaces, but not for powder. At 100% RH, healing is the same for both types of granite samples.

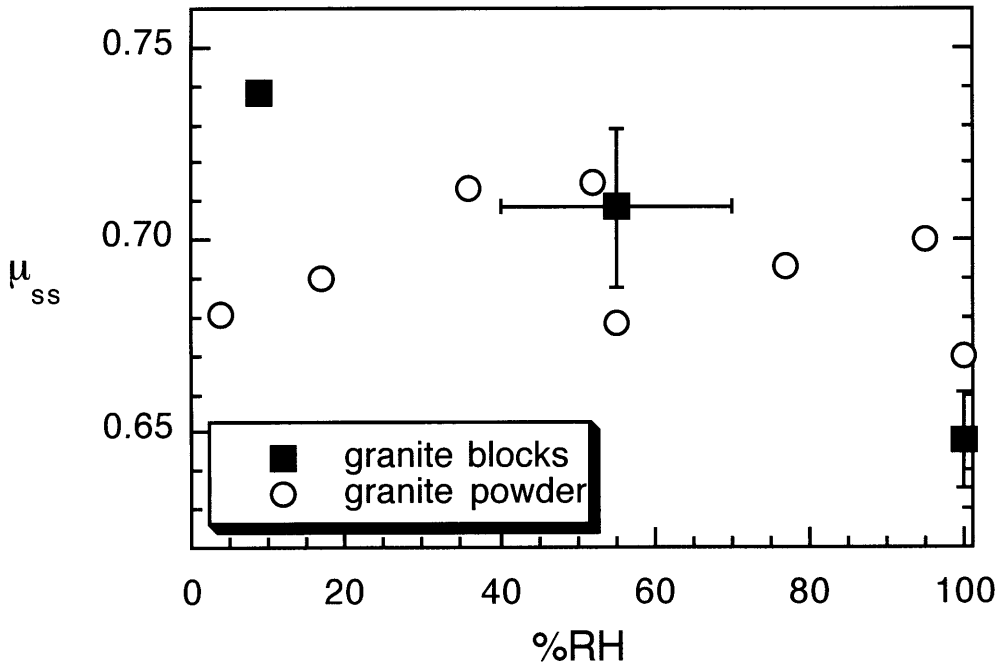

Figure 3.10. Steady-state sliding friction does not vary with humidity for granite powder. For bare surfaces, sliding friction is greater at low humidity than at high humidity, consistent with *Dieterich and Conrad* [1984]. There is large scatter in sliding friction values at intermediate humidity for bare surfaces.

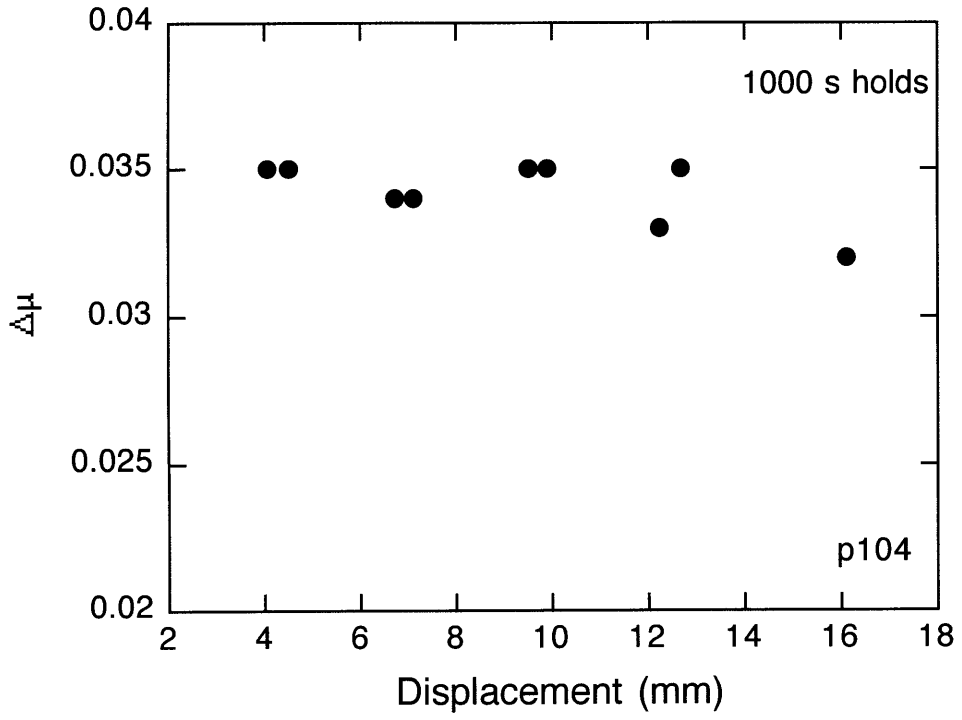

Figure 3.11. Healing vs. displacement for Westerly granite bare surfaces, 100% RH, 5 MPa normal stress.

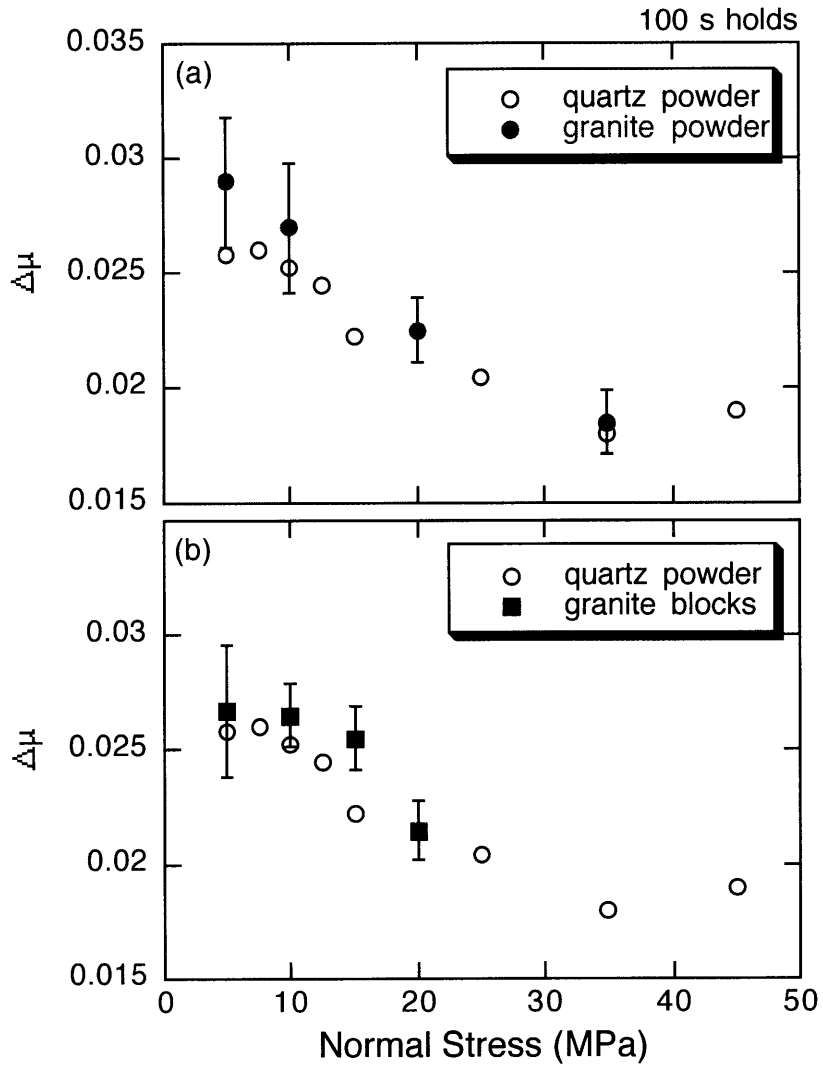

Figure 3.12. (a). Healing for Westerly granite powder as a function of normal stress. Healing decreases with increasing normal stress. Average values of healing for quartz powder plotted with open symbols. (b). Healing for Westerly granite blocks (bare surfaces) also decreases with normal stress. However, normal stress range is limited by block strength.

powder. The same trend is observed for bare granite surfaces (Figure 3.12b) up to 20 MPa. The normal stress range for bare surface experiments is limited by the strength of the granite blocks.

3.4 Discussion

3.4.1. RH dependence of friction behavior

Our observations show that time-dependent frictional healing can be reduced or eliminated at low RH for granite powder and bare surfaces (Figure 3.9). These observations suggest that there is a water-assisted healing mechanism operating at room temperature for granite as well as for quartz (Figure 3.4) [*Dieterich and Conrad*, 1984, *Frye and Marone*, 2002].

The coefficient of sliding friction is independent of humidity for quartz powder [*Frye and Marone*, 2002] and granite powder. However, for quartzite blocks [*Dieterich and Conrad*, 1984] and granite blocks, sliding friction decreases with humidity (Figure 3.10). These behaviors illustrate that the deformation of bare surfaces is different from the deformation of powders.

Numerical simulations indicate that the sliding friction of powders is nearly independent of interparticle friction [*Morgan*, 1999], possibly because grain rotation becomes more prevalent as grain-grain sliding resistance increases. With no gouge layer present, the sliding friction of the granite block surfaces is controlled asperity-asperity contacts and influenced by asperity deformation, indentation, breakage, and ploughing [*Scholz*, 1976]. Friction could be reduced by the presence of a boundary lubricant, or, because the friction observed during steady-state sliding of blocks is much more dependent on asperity strength, hydrolytic weakening of the block surfaces could reduce macroscopic sliding friction.

3.4.2. Normal stress dependence of friction behavior

Humidity dependent healing mechanisms operate over a range of applied normal stresses from 5 to 45 MPa (Figures 3.4, 3.5). Healing decreases with increasing normal stress at a given humidity for quartz powder, granite powder, and granite blocks (Figures 3.5, 3.12). The rate- and state-dependent friction parameters taken from velocity stepping tests for 100% RH preconditioned quartz powder are also a function of normal stress. The parameters a and b_1 decrease with increasing normal stress, consistent with the results of SHS tests for quartz powder, granite powder, and granite blocks.

We interpret the relationship between time-dependent healing and normal stress to be the result of chemically assisted mechanisms that strengthen contact junctions. If asperities are in a state of incipient plastic flow [*Bowden and Tabor*, 1964], stress at contact junctions is limited by the strength of the material and should be independent of the applied normal stress. The *load* supported by contact junctions, however, may increase with increasing applied normal stress.

Load-dependent contact junction strengthening could be due to a low-temperature plasticity mechanism that increases real area of contact, and therefore adhesion and frictional healing, during holds [*Dieterich and Kilgore*, 1994; 1996]. When quartz is exposed to water, there is evidence of the formation of a weak surface layer of 0.2 to 3 μm thickness [*Westbrook and Jorgensen*, 1968; *Clark et al.*, 1978]. At low applied normal stress, the loads at contact junctions could be supported by the weaker, visco-plastically deforming surface layer (Figure 3.13a), the strength of which would be determined by the quantity of water present [*Blacic and Christie,* 1984; *Jaoul et al.,* 1984; *Mainprice and Paterson,* 1984; *Kronenberg and Tullis,* 1984; *Evans and Kohlstedt,* 1995]. At higher normal stress, the greater loads at contact junctions would be supported in part by the stronger material below the surface layer [*Liu*, 1950;

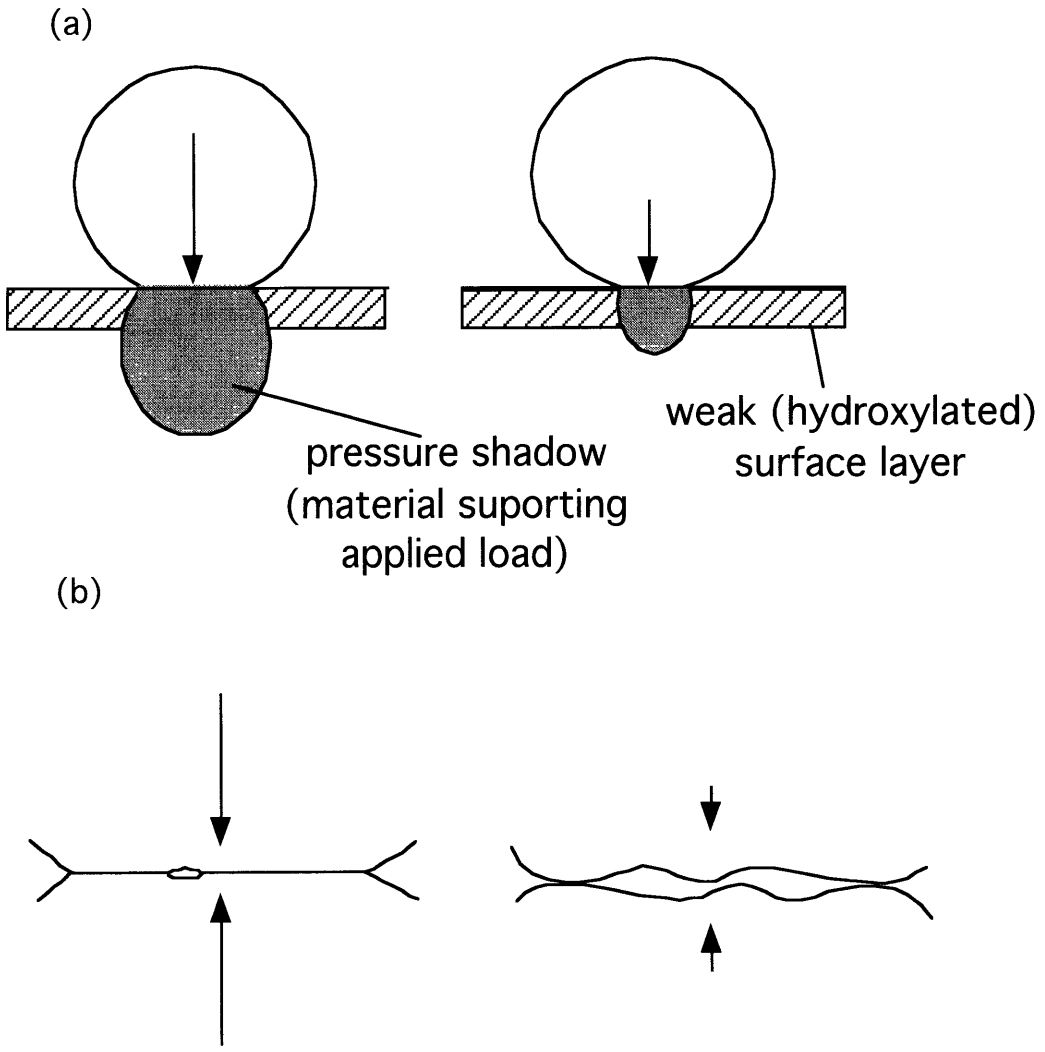

Figure 3.13. A schematic representation of a stressed contact junction. (a) High loads at contact junctions may be supported in part by visco-plastic deformation of the surface layer and elastic deformation of the stronger substrate. (b) Higher loads at contact points may close off pathways for water desorption/adsorption, reducing the efficiency of that strengthening mechanism.

Westbrook and Jorgensen, 1968; *Hardy et al.*, 1971], effectively increasing the mineral hardness and reducing surface deformation and adhesion per unit load.

Another possible mechanism for humidity dependent healing is desorption of surface water between two contacts and subsequent increase in bonding strength [*Hirth and Rice*, 1980]. This mechanism could be dependent on normal stress (Figure 3.13b) as larger contact junctions at higher loads could lengthen paths for water desorption/adsorption, making that strengthening mechanism less efficient.

Preconditioning the gouge layer with high normal stress load cycles ensures that shear localization [*Yund et al.*, 1990; *Logan et al.*, 1992; *Sleep*, 1997, *Sleep et al.*, 2000] begins at the same stage in each experiment (Figures 3.1, 3.6). However, velocity stepping performed at low normal stress requires the use of a second state variable (Equations 3.1 and 3.2) to properly model the velocity stepping data. The rate- and state- dependent friction parameters that best correspond with time dependent healing (a and b_1) decrease with increasing normal stress (Figure 3.8). The absolute value of b_2 also decreases. The layer thickness response to velocity perturbations at low normal stress may be due to the preconditioning of the layer. Typically the response of layer thickness to a decrease in sliding velocity is compaction of the layer (e.g. Figures 3.7c and 3.7d, or *Mair and Marone*, [1999]). For low normal stress tests in this study, the layer compacts in response to a decrease in velocity and then dilates. If the layers are over-compacted during preconditioning, perhaps large changes in layer thickness are difficult to maintain during velocity stepping tests. At normal stresses greater than 15 MPa, the layer thickness responds in a typical manner to a velocity step, the second state variable becomes less important and the magnitude of the parameter b_2 decreases. Because a and b_1 are consistent with healing data from SHS tests on granite blocks with no gouge layer, we interpret those parameters

to be representative of contact junction processes, while b_2 and the second state variable we attribute to microstructural mechanisms such as layer density change.

3.5. Conclusions

We have shown that humidity has a significant effect on frictional healing for quartz powder, granite powder, and granite blocks at room temperature. Frictional healing is negligible at low humidity and increases with increasing RH for quartz powder and granite blocks. Frictional healing is reduced at low RH for granite powder, but does not go to zero, possibly due to higher water content in powders with smaller initial grain sizes.

The coefficient of sliding friction is independent of humidity for powders, but sliding friction decreases with humidity for the bare surface granite blocks. While particles in thick gouge layers are allowed to rotate during deformation, elastic-brittle asperity deformation and/or asperity ploughing controls the sliding friction of the granite block surfaces [*Scholz*, 1976]. Therefore, hydrolytic weakening of the block surfaces could reduce macroscopic sliding friction. Alternatively, water could act as a boundary lubricant and reduce sliding resistance at the contact points.

We observe that chemically assisted frictional healing mechanisms are active at applied normal stress as low as to 5 MPa. Healing rate decreases with increasing normal stress for quartz powder, granite powder, and granite blocks over a range of RH.

Preconditioning the powders adds complexity to the velocity-dependence of granular fiction, requiring a two state variable model to fit the data. However, the parameters a and b_1 taken from the velocity-stepping tests are consistent with the time-dependent healing data from powders and granite blocks with *no gouge layer*. Therefore, we propose that micro-structural

effects are observed in the parameter b_2, and that the normal stress dependence of a, b_1, and time-dependent healing is primarily caused by load dependent contact junction processes. We posit that both low temperature plasticity and water adsorption/desorption at contact junctions could result in time-dependent strengthening of a frictional interface, as both mechanisms may be less efficient at higher contact loads.

3.6. References for chapter 3:

Beeler, N. M., T. E. Tullis, and J. D. Weeks, The roles of time and displacement in evolution effect in rock friction, *Geophys. Res. Lett.*, *21*, 1987-1990, 1994.

Blacic, J. D., and J. M. Christie, Plasticity and hydrolytic weakening of quartz single crystals, *J. Geophys. Res.*, *89*, 4223-4240, 1984.

Blanpied, M.L., and T.E. Tullis, The stability and behavior of a frictional system with a two state variable constitutive law, *Pure Appl. Geophys.*, *124*, 43-73, 1986.

Blanpied, M.L., J.D. Weeks, and T.E. Tullis, Effects of slip, slip rate, and shear heating on the friction of granite, *J. Geophys. Res.*, *103*, 489-511, 1998.

Bowden, F. P. and D. Tabor, The friction and lubrication of solids. Part II. Oxford: Clarenden Press, 1964.

Brace, W.F., Some new measurements of linear compressibility of rocks, *J. Geophys. Res. 70*, 391-398, 1965.

Chester F.M. Effects of temperature on friction: constitutive equations and experiments with quartz gouge, *J. Geophys. Res.* 99, 7247-61, 1994.

Clark, G.J., C.W. White, D.D. Alfred, B.R. Appleton, and I.S.T. Tsong, Hydrogen concentration profiles in quartz determined by a nuclear reaction technique, *Phys. Chem. Miner. 3*, 199-211, 1978.

Dieterich, J. H., Time-dependent friction in rocks, *J. Geophys. Res., 77*, 3690-3697, 1972.

Dieterich, J. H., Time-dependent friction and the mechanics of stick-slip, *Pure Appl. Geophys., 116*, 790-805, 1978.

Dieterich, J. H., Modeling of rock friction: 1. Experimental results and constitutive equations, *J. Geophys. Res., 84,* 2161-2168, 1979.

Dieterich, J. H., and G. Conrad, Effect of humidity on time and velocity-dependent friction in rocks, *J. Geophys. Res., 89,* 4196-4202, 1984.

Dieterich, J. H., and B. Kilgore, Direct observation of frictional contacts: new insights for state-dependent properties, *Pure Appl. Geophys., 143*, 283-302, 1994.

Dieterich, J. H., and B. Kilgore, Imaging surface contacts: power law contact distributions and stresses in quartz, calcite, glass and acrylic plastic, *Tectonophys., 256*, 219-239, 1996.

Evans, B., and D. L. Kohlstedt, Rheology of rocks, *in Rock Physics and Phase Relations, A Handbook of Physical Constants, AGU Reference Shelf 3*, edited by T. J. Ahrens, 148-165, AGU, Washington, D.C., 1995.

Frye, K.M. and C. Marone, The effect of humidity on granular friction at room temperature, *J. Geophys. Res., in press*, 2002.

Hardy, C., C.N. Baronet and G.V. Tordion, The elasto-plastic indentation of a half-space by a rigid sphere, *Int. J. Num. Meth. Eng. 3*, 451-462, 1971.

Hirth, J.P. and J.R. Rice, On the thermodynamics of adsorption at interfaces as it influences decohesion, *Metallurgical Trans. A 11*, 1501-1511, 1980.

Jaoul, O., J. Tullis, and A. K. Kronenberg, The effect of varying water contents on creep behavior of Heavitree quartzite, *J. Geophys. Res.*, *89*, 4298-4312, 1984.

Karner, S. L., and Marone, C., Frictional restrengthening in simulated fault gouge: Effect of shear load perturbations, *J. Geophys. Res.*, *106*, 19319-19337, 2001.

Kronenberg, A. K., and J. Tullis, Flow strengths of quartz aggregates: Grain size and pressure effects due to hydrolytic weakening, *J. Geophys. Res.*, *89*, 4281-4297, 1984.

Liu, C.K., Stresses and deformations due to tangential and normal loads on an elastic solid with applications to contact stresses, Ph.D. thesis, U. of Illinois, 1950.

Logan, J.M., C.A. Dengo, N.G. Higgs, and Z.Z. Wang, Fabrics of experimental fault zones: their development and relationship to mechanical behavior, in *Fault Mechanics and Transport Properties of Rocks*, ed. B. Evans and T.F. Wong, London Academic, 33-67, 1992.

Mainprice, D. H., and M. S. Paterson, Experimental studies of the role of water in the plasticity of quartzites, *J. Geophys. Res.*, *89*, 4257-4270, 1984.

Mair, K., and C. Marone, Friction of simulated fault gouge for a wide variety of velocities and normal stresses, *J. Geophys. Res.*, *104*, 28899-28914, 1999.

Marone, C., Laboratory-derived friction laws and their application to seismic faulting, *Annu. Rev., Earth Planet. Sci.*, *26*, 696, 1998a.

Marone, C., The effect of loading rate on static friction and the rate of fault healing during the earthquake cycle, *Nature, 391,* 69-72, 1998b.

Morgan, J. K., Numerical simulations of granular shear zones using the distinct element method, 2: Effects of particle size distribution and interparticle friction on mechanical behavior, *J. Geophys. Res.*, *104*, 2721-2732, 1999.

Rabinowicz, E., The nature of static and kinetic coefficients of friction, *J. Appl. Phys. 22*, 1373-1379, 1951.

Rice, J.R., Hydrogen and interfacial cohesion, in *Effect of Hydrogen on Behavior of Materials*, ed. A.W. Thompson and I.M. Berstein, Metallurgical Society of AIME, New York, 455-466, 1976.

Richardson, E., and C. Marone, Effects of normal stress vibrations on frictional healing, *J. Geophys. Res., 104*, 28859-28878, 1999.

Ruina, A., Slip instability and state variable friction laws, *J. Geophys. Res., 88*, 10359-10370, 1983.

Scholz, C.H., Earthquakes and friction laws, *Nature, 391*, 37-42, 1998.

Scholz, C. H., and J. T. Engelder, The role of asperity indentation and ploughing in rock friction; I, Asperity creep and stick-slip, *International Journal of Rock Mechanics and Mining Sciences, 13*, 149-154, 1976.

Sleep, N. H., E. Richardson, and C. Marone, Physics of friction and strain rate localization in simulated fault gouge, *J. Geophys. Res., 105*, 25875-25890, 2000.

Sleep, N. H., Application of a unified rate and state friction theory to the mechanics of fault zones with strain localization, *J. Geophys. Res., 102*, 2875-2895, 1997.

Tullis, T. E., and J. D. Weeks, Constitutive behavior and stability of frictional sliding of granite, *Pure Appl. Geophys., 124*, 383-414, 1986.

Westbrook, J.H., and P.J. Jorgensen, Effects of water desorption on indentation microhardness anisotropy in minerals, *Am. Mineral., 53*, 1899-1909, 1968.

Whalen, J.W., Thermodynamic properties of water adsorbed on quartz, *J. Phys. Chem., 65*, 1676-81, 1981.

Wong, T. -f., Y. Gu, T. Yanagidani, and Y. Zhao, Stabilization of faulting by cumulative slip, in *Fault mechanics and transport properties of rocks; a festschrift in honor of W. F. Brace*, Evans, B. and T. -f. Wong (editors), 119-143, 1992.

Yund, R. A., M.L. Blanpied, J.D. Weeks, and T.E. Tullis, 1990, Observation and interpretation of microstructures in experimental fault gouges, *J. Geophys. Res., 95*,15589-15602.

Table 3.1. Experiments from chapter 3. All experiments performed at room temperature.

Experiment Name	Material	*Normal Stress*	*Relative Humidity*
m488	quartz powder	15 MPa, 35 MPa	< 5%
m492	quartz powder	35 MPa	15%
m493	quartz powder	5 MPa	15-20%
m496	quartz powder	35 MPa	63%
m497	quartz powder	5 MPa	63%
m499	quartz powder	5 MPa	5%
m501	quartz powder	10 MPa	12%
m529	quartz powder	10 MPa	< 5%
m530	quartz powder	5 MPa	29%
m531	quartz powder	35 MPa	29%
m532	quartz powder	10 MPa	29%
p007	quartz powder	10 MPa	52%
p008	quartz powder	5 MPa	90%
p009	quartz powder	15 MPa	57%
p010	quartz powder	10 MPa	88%
p011	quartz powder	5 MPa	100%
p012	quartz powder	15 MPa	90%
p013	quartz powder	10 MPa	100%
p014	quartz powder	35 MPa	90%
p015	quartz powder	15 MPa	100%
p016	quartz powder	35 MPa	100%
p017	quartz powder	45 MPa	60%
p021	quartz powder	15 MPa	33%
p022	quartz powder	12.5 MPa	33%
p023	quartz powder	10 MPa	33%
p024	quartz powder	7.5 MPa	33%
p025	quartz powder	5 MPa	33%
p026	quartz powder	5 MPa	100%
p027	quartz powder	10 MPa	100%
p028	quartz powder	15 MPa	100%
p029	quartz powder	25 MPa	100%
p030	quartz powder	12.5 MPa	100%
p031	quartz powder	45 MPa	100%
p032	quartz powder	7.5 MPa	100%
p043	quartz powder	5 MPa	100%
p044	quartz powder	45 MPa	100%
p045	quartz powder	10 MPa	100%
p055	quartz powder	15 MPa	100%
p056	quartz powder	25 MPa	100%
p057	quartz powder	35 MPa	100%
p058	quartz powder	20 MPa	100%
p095	quartz powder	5 MPa	100%
p097	quartz powder	35 MPa	20%
p105	quartz powder	5 MPa	10%

Table 3.1. *cont.*

Experiment Name	Material	*Normal Stress*	*Relative Humidity*
p002	West. granite powder	25 MPa	52%
p003	West. granite powder	25 MPa	95%
p004	West. granite powder	25 MPa	77%
p005	West. granite powder	25 MPa	55%
p006	West. granite powder	25 MPa	100%
p019	West. granite powder	25 MPa	36%
p059	West. granite powder	25 MPa	17%
p060	West. granite powder	25 MPa	< 5%
p106	West. granite powder	25 MPa	11%
p119	West. granite powder	5 MPa	100%
p120	West. granite powder	10 MPa	100%
p121	West. granite powder	20 MPa	100%
p122	West. granite powder	35 MPa	100%
p073	West. granite blocks	5 MPa	16 to 100 %
p074	West. granite blocks	5, 10, 15, 5 MPa	100%
p075	West. granite blocks	5 MPa	12%
p076	West. granite blocks	5, 10, 15 MPa	8%
p077	West. granite blocks	10 MPa	10%
p101	West. granite blocks	5 MPa	38-43%
p102	West. granite blocks	5 MPa	72%
p104	West. granite blocks	5 MPa	100%
p129	West. granite blocks	20 MPa	100%

4. Influence of grain characteristics on the friction of granular shear zones[2]

Synopsis. Numerical models of granular shear show lower friction and a greater tendency for stick slip than laboratory studies designed to investigate fault mechanics. Here we report on laboratory experiments designed to reproduce the conditions of numerical models and test the role that grain characteristics play in controlling frictional behavior. Friction and microstructural data are compared for direct shear experiments on thin layers (2-3 mm) of angular quartz sand and spherical glass beads. We study the effect of grain shape, roughness, size distribution, and comminution. In a non-fracture loading regime, sliding friction for smooth spherical particles ($\mu \sim 0.45$) is measurably lower than for angular particles ($\mu \sim 0.6$). A narrow particle size distribution (PSD) of spherical beads (105-149 μm) exhibits unstable stick-slip behavior, whereas a wide PSD of spheres (1-800 μm), and the angular gouge, display stable sliding. At higher stress, where grain fracture is promoted, initially spherical particles become stable with accumulated slip and friction increases to the level observed for angular gouge. We find that frictional strength and stability of a granular shear zone are sensitive to grain shape, PSD, and their evolution. We suggest that a low friction translation mechanism, such as grain rolling, operates in gouge composed of smooth particles. Our results show that the first order disparities between laboratory and numerical studies of granular shear can be explained by differences in grain characteristics and loading conditions. Since natural faults predominantly contain angular gouge we find no evidence for a fault weakening mechanism associated with the presence of gouge.

---

[2] This chapter is *in press* as Mair, K., K.M. Frye, and C. Marone, Influence of grain characteristics on friction of granular shear zones, *J. Geophys. Res.*, 2002.

4.1. Introduction

Earthquakes occur on active faults in the brittle crust that are often perceived as discrete discontinuities (or seams) between intact country rock. However, natural faults commonly contain significant accumulations of granular wear material (gouge) making them mechanically and physically distinct from the surrounding rock. The nature and evolution of this granular wear material significantly affects mechanical strength, frictional stability and the potential for seismic slip. To understand the mechanics of earthquakes and faulting, it is therefore essential to understand the behavior of gouge-filled fault zones.

In this paper we investigate the dynamics of gouge-filled fault zones by studying shear in thin granular layers constrained within rigid boundaries. Many similar laboratory studies have been carried out and much is known about the general frictional properties of gouge under geophysically-relevant conditions [see *Marone,* 1998; *Scholz,* 1998, for recent summaries]. However, much of this work has focused on the effects of net shear displacement and shear localization, and relatively little is known about how specific grain characteristics influence the bulk frictional strength. A key problem is that the experimental configurations, designed to achieve high stresses, do not allow direct observation of the strain rate field during deformation. Thus, the connection between frictional behavior and particle dynamics including rotation, translation, and fracture has to be inferred indirectly or from 'post-experiment' microstructural observations.

Numerical simulations offer the possibility of improving our understanding of the dynamics and kinematics of granular shear [*Pisarenko and Mora*, 1994; *Mora and Place,* 1994, 1998, 1999; *Scott,* 1996; *Morgan,* 1999; *Morgan and Boettcher,* 1999; *Aharonov and Sparks,* 1999]. These studies show that complex dynamics can arise from simple particle-particle

interactions when large numbers of grains are considered. However, many of the existing numerical studies yield significantly different results than corresponding laboratory studies. In particular, numerical studies show lower frictional strength and a greater tendency for instability than laboratory studies. In one class of numerical simulations, the observation of low friction has been linked to rolling in particles of simulated fault gouge [*Mora and Place*, 1999]. It has been suggested that these results may explain the apparent weakness of major faults, such as the San Andreas in California.

There are several key differences between the numerical and laboratory studies. In particular, numerical shear zones are typically composed of idealized circular (2-D) particles that do not evolve, or evolve very little during shear, whereas laboratory experiments are carried out on highly angular (3-D) particles undergoing pervasive fracture and comminution [*Sammis et al.*, 1987; *Marone and Scholz* 1989]. We suggest that the apparent disparity between observations from laboratory and numerical studies of granular shear zones may be a consequence of these distinct differences in the nature of gouge and the deformation regimes imposed in both cases. For example it is unclear whether idealized spherical particles typical in numerical models [*Mora and Place*, 1998, 1999; *Morgan and Boettcher*, 1999; *Morgan* 1999; *Aharonov and Sparks*, 1999] and angular gouge used in laboratory experiments have a similar or distinct frictional response. Few laboratory studies have investigated the effect of grain shape on the behavior of sheared granular materials [but see *Mueth et al.*, 2000].

The purpose of this paper is to investigate the influence of grain shape, roughness, and particle size distribution (PSD) on the frictional strength and stability of sheared granular layers. We carry out experiments at a range of normal stresses chosen to investigate both minimal and pervasive grain fracturing. Loading conditions are designed to reproduce both numerical

modeling conditions and standard geophysical laboratory conditions. We observe systematic differences in the friction of angular and spherical granular materials. Our results are simple and indicate that much if not all of the first order differences between numerical and laboratory experiments can be explained by differences in physical characteristics of gouge particles.

4.2. Experimental method

We shear granular layers between roughened steel blocks using a servo-hydraulic controlled direct shear apparatus (Figure 4.1). Extensive work has been done using this geometry [*Dieterich,* 1978, 1979; *Marone,* 1998] that we use in this study. We use granular material to simulate wear products (gouge) commonly found in exhumed natural faults. The roughened boundary surfaces approximate the roughness of real faults and help promote shear throughout the layer rather than at the boundary. We apply and maintain constant normal force to the side blocks, then drive the center block at a specified load point velocity to initiate shear within the granular layer. Layers compact and dilate during shear reflecting the dynamic gouge re-organization required to accommodate shear. Layer thickness changes are continuously monitored together with shear and normal stresses. The coefficient of friction is defined as shear stress divided by normal stress. Additional experimental details are given in *Karner and Marone* [1998] and *Mair and Marone* [1999].

To investigate the influence of grain characteristics on sliding friction we conducted identical direct shear experiments on 3 mm thick layers of different simulated fault gouges. These gouges consisted of: a) angular Ottawa sand; and b) spherical soda-lime glass beads (Figure 4.2). The Ottawa sand is a pure > 99% quartz obtained from the US silica Company, Ottawa, Illinois and

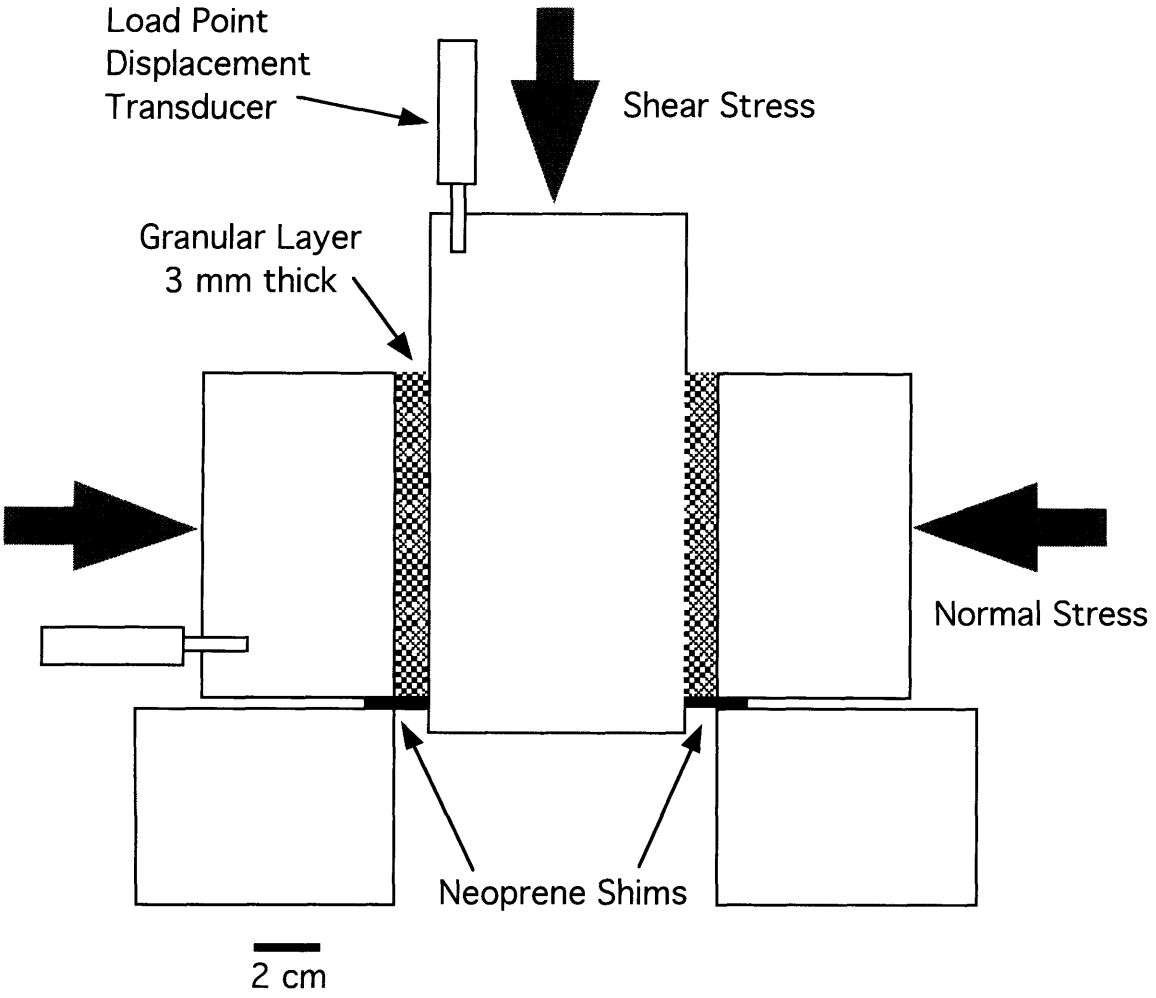

Figure 4.1. Schematic diagram of direct shear apparatus showing the 100x100 mm, 3 mm thick granular layers sandwiched between rough steel bocks. The orientations of shear stress, normal stress and load point displacement transducers are indicated.

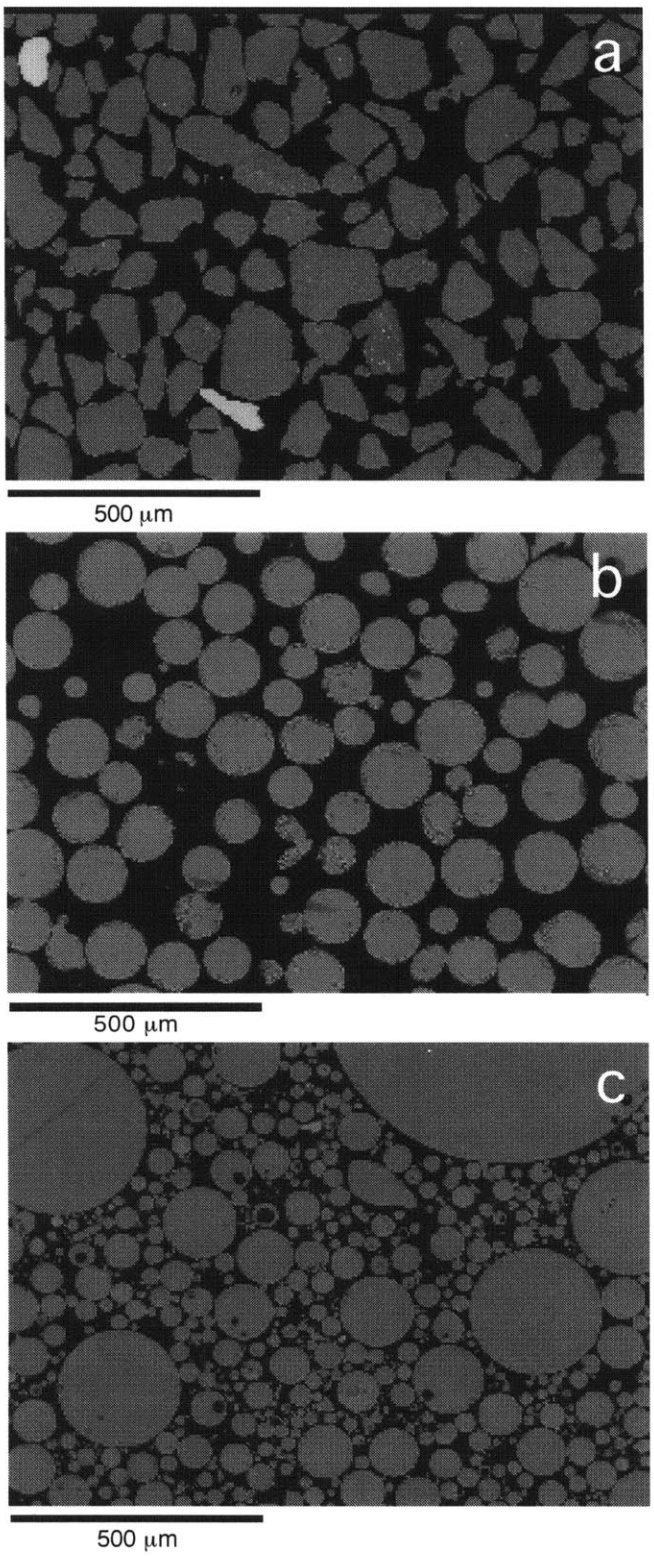

Figure 4.2. SEM photomicrographs of undeformed gouge: a) angular grains; b) spherical grains. The materials have a size range of 50-150 μm and 105-149 μm (grain diameter) respectively and means of ~110 μm and ~120 μm. c) Spherical grains with a size range 1-800 μm (grain diameter) and a log-normal size distribution by weight with peak grain size at ~100 μm.

has been used in previous laboratory studies of friction [*Karner and Marone,* 1998*; Richardson and Marone,* 1999*; Mair and Marone,* 1999]. We acquired precision glass spheres from Mo-Sci Corporation, Rolla, Missouri. Importantly, the particle size distribution (PSD) and mean grain size of the undeformed sand (Figure 4.2a) and spheres (narrow PSD, Figure 4.2b) are comparable, as are the compressive strengths of individual grains, hence the main difference between the gouges is the grain shape (Figure 4.2). A third gouge (Figure 4.2c) composed of spheres with a wide PSD was used to investigate the influence of grain size distribution (section 4.3.3.) for constant spherical shape. This material had a log-normal PSD by weight in order to represent the PSD of a mature shear band [*An and Sammis*, 1994]. Experiments were carried out under a range of normal stresses (σ_n = 5 – 50 MPa) corresponding to regimes where previous work has indicated grain fracture to be minimal and pervasive respectively [*Mair and Marone,* 2000]. Minimal grain fracture corresponds to the non-fracture regime generally invoked in numerical simulations, whereas a pervasive fracture regime is comparable to previous laboratory friction tests and potentially more applicable to natural conditions. Load point velocity ranged between 0.1 μm/s and 5000 μm/s. All experiments were carried out at room temperature and humidity. Other experimental conditions are presented in Table 4.1 at the end of the chapter.

Deformed gouge layers were impregnated with epoxy resin and thin sections were prepared for microstructural analysis. Spherical beads required higher stresses to undergo pervasive fracture than angular quartz. This is perhaps due to a larger number of flaws in the quartz or to stress concentrations at grain irregularities. Grain fracture was recognized by significant audible cracking upon loading, and subsequent microstructural analysis. At a normal stress of σ_n = 25 MPa few spherical grains fractured. Therefore the normal stress conditions used to achieve non-fracture and fracture of the two materials were as follows. Non-fracture regime: angular

particles σ_n < 10MPa; spherical particles σ_n < 30 MPa. Fracture regime: angular particles σ_n >10MPa; spherical particles σ_n > 30 MPa.

4.3. Results

4.3.1. Friction in angular and spherical gouge

4.3.1.1. Low stress (non-fracture regime)

Initial shearing experiments were carried out at low normal stress (σ_n = 5 MPa) in the regime where grain fracture is minimal [*Mair and Marone,* 2000]. The friction coefficients for angular (Figure 4.2a) and spherical (Figure 4.2b) gouge material are plotted as a function of shear displacement in Figure 4.3. The main observation is that the coefficient of friction is markedly lower for the spherical gouge ($\mu \sim 0.45$) than the angular gouge ($\mu \sim 0.6$). In addition, the angular gouge exhibits stable sliding throughout whereas the spherical gouge exhibits unstable stick-slip. The angular gouge shown here was sheared at a constant load point velocity of V=5 mm/s throughout. Previous work on the angular gouge showed that the base level of friction was comparable (~ 0.6) for 4 orders of magnitude range in load point velocity [*Mair and Marone,* 1999].

We sheared spherical gouge at 10 μm/s initially and then changed velocity over several orders of magnitude to determine whether the instability observed was velocity dependent. Figure 4.4 shows details of the periodic saw-tooth fluctuations in shear stress, typical of stick-slip cycles. The regular stick slip events are characterized by a slow (elastic) increase in stress, a small inelastic rollover and rapid dynamic stress drop that is accompanied by audible acoustic energy release. Figure 4.4 shows stick slip cycles for two sliding velocities (V = 10 μm/s and 100 μm/s). Stress drop (τ_{max} - τ_{min}) decreases with increasing sliding velocity. Figure 4.5 shows

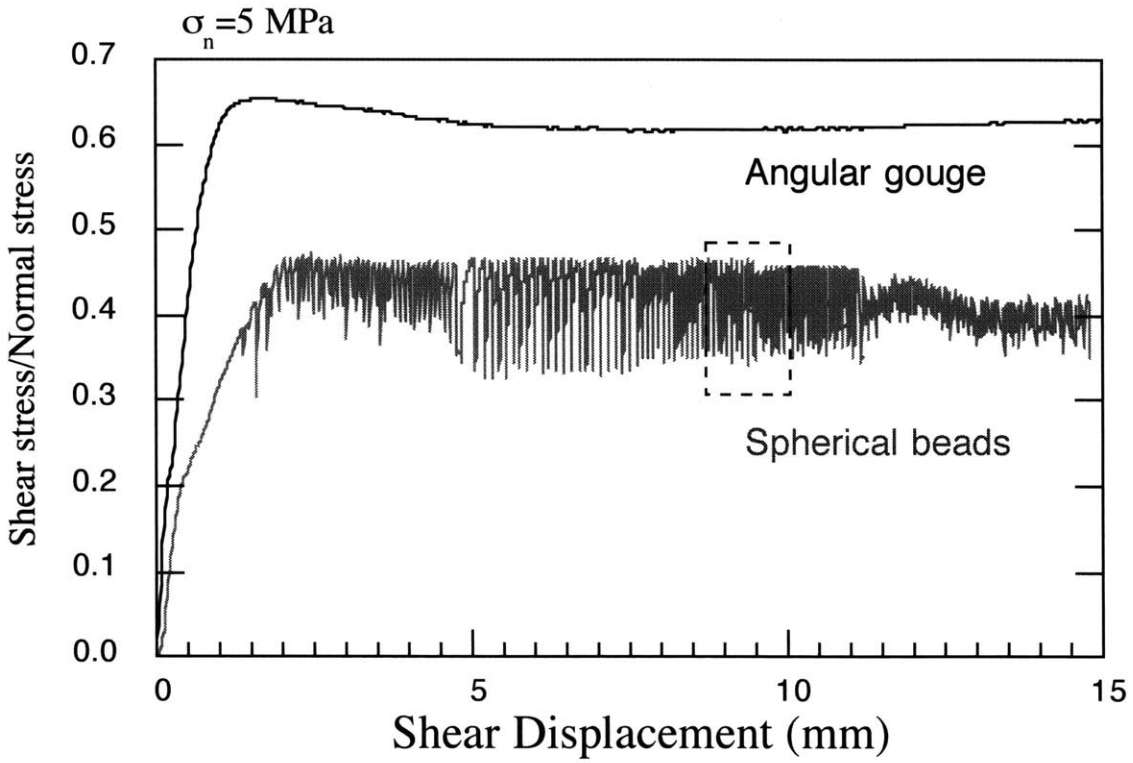

Figure 4.3. Friction as a function of shear displacement for angular and spherical grains at $\sigma_n = 5$ MPa. Grain fracture is minimal at this stress for both materials. Spherical grains show a lower value of friction coefficient and exhibit stick slip behavior whereas angular gouge slides stably with higher friction. Boxed region is enlarged in Figure 4.

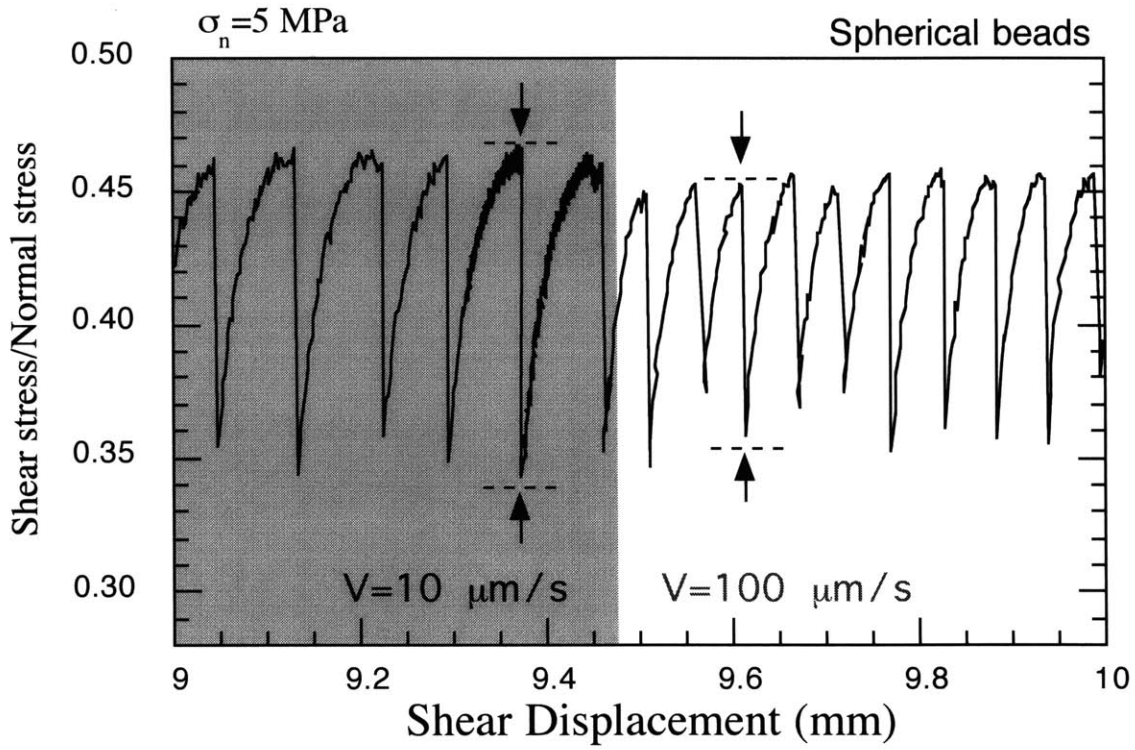

Figure 4.4. Enlargement of boxed region from Figure 3 illustrates details of stick slip behavior for spherical gouge. Shaded and unshaded parts indicate slip rates of 10 μm/s and 100 μm/s respectively. The stress drop (τ_{max} - τ_{min}) decreases with increased sliding velocity.

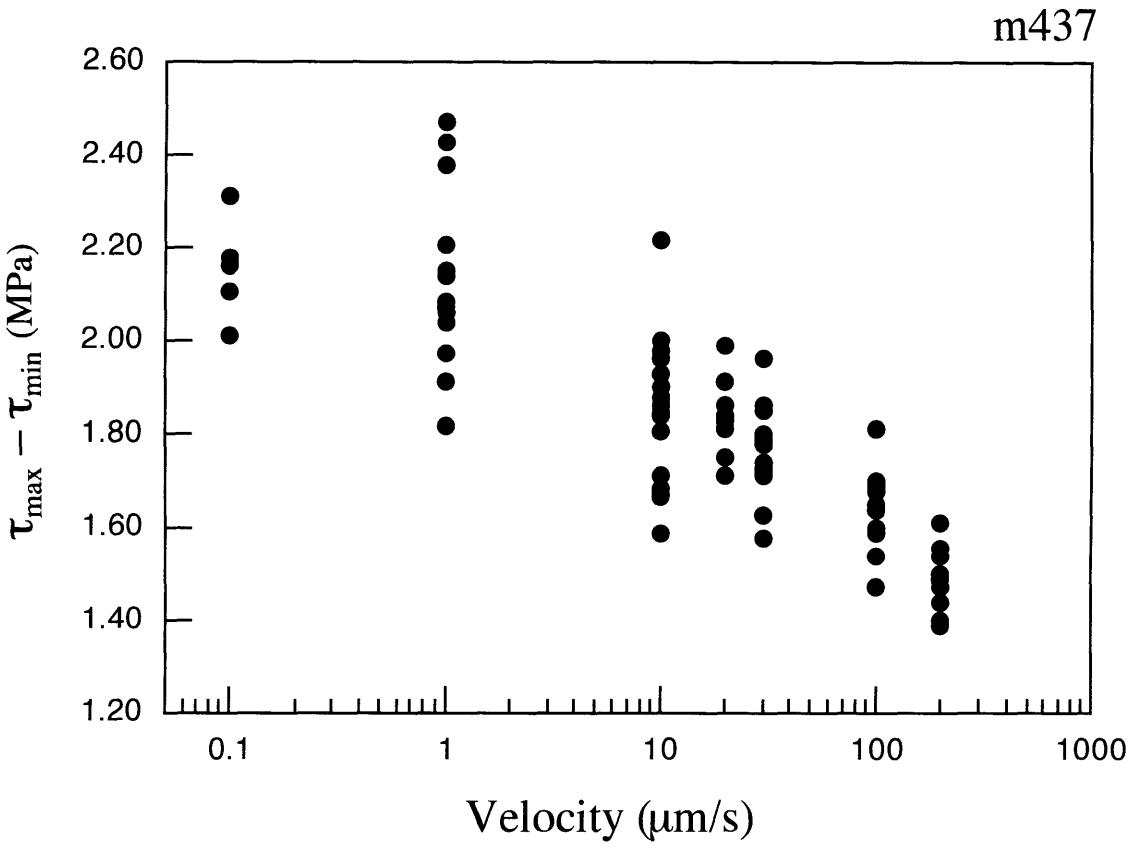

Figure 4.5. Stress drop (τ_{max} - τ_{min}) as a function of sliding velocity for spherical particles (σ_n = 25 MPa). Stress drop magnitude decreases with increasing sliding velocity.

stress drop measurements for many individual stick slip events at a range of sliding velocities. The data are consistent with increased static yield strength due to the longer stick-slip recurrence interval at lower velocity. Our observations agree with previous work on gouge [*Wong and Zhao,* 1990] and mineral and rock surfaces [*Berman et al.,* 1996; *Karner and Marone*, 2000].

4.3.1.2. High stress (fracture regime)

Figure 4.6 shows friction versus shear displacement for angular and spherical gouge at higher normal stresses (σ_n = 25 MPa and σ_n = 40 MPa respectively) in the regime where grain fracture is important. As noted above, the stress required for the onset of pervasive fracture is slightly higher in spherical beads than angular gouge. Apart from comminution effects, we believe that the differences in nominal stress yield do not cause differences in frictional behavior. The angular gouge has a stable steady state friction level of 0.6, comparable to lower normal stress tests (Figure 4.3). Initially, the spherical material has low friction ($\mu \sim 0.45$) and shows stick slip behavior but with increasing shear, frictional strength increases and sliding stabilizes. After an engineering shear strain of ~8, (15 mm shear displacement), frictional strength is the same for angular and initially spherical particles.

4.3.2. Microstructural development in angular and spherical gouge

Shear zone microstructures were investigated using SEM. Figure 4.7 shows photomicrographs of angular gouge deformed to 20 mm slip under normal stress of a) σ_n = 5 MPa and b) σ_n = 50 MPa. The granular layers were initially identical (Figure 4.2a). Note the lack of grain fracture and the homogeneous texture at σ_n = 5 MPa (Figure 4.7a) compared with

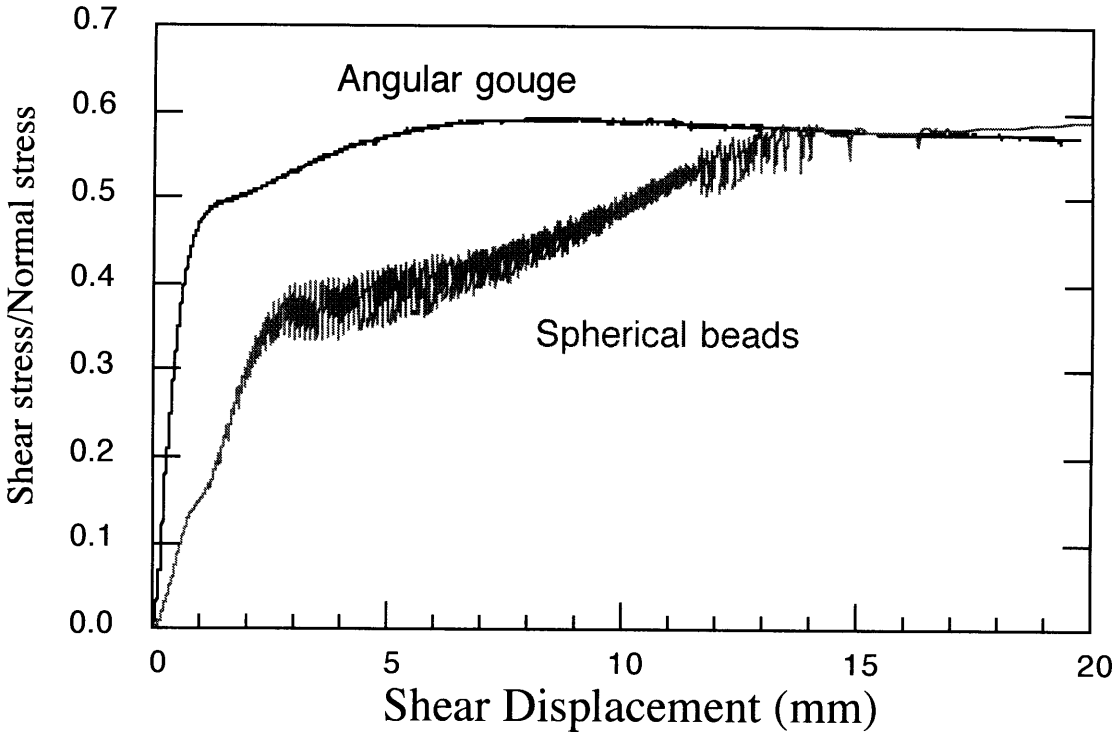

Figure 4.6. Friction versus shear displacement for angular and spherical gouge (initially 105-149 μm) deformed at σ_n = 25 MPa and σ_n = 40 MPa respectively. Grain fracture is pervasive at these conditions in each material. With increasing slip, the spherical granular material undergoes a transition from stick slip to stable sliding and its frictional strength increases. Angular gouge exhibits stable shear throughout. Both tests are initially loaded at V=10 μm/s, the spherical gouge includes subsequent changes in slip rate. A decrease in slip rate at 11 mm slip alters the stress drop amplitude and frequency of the instabilities.

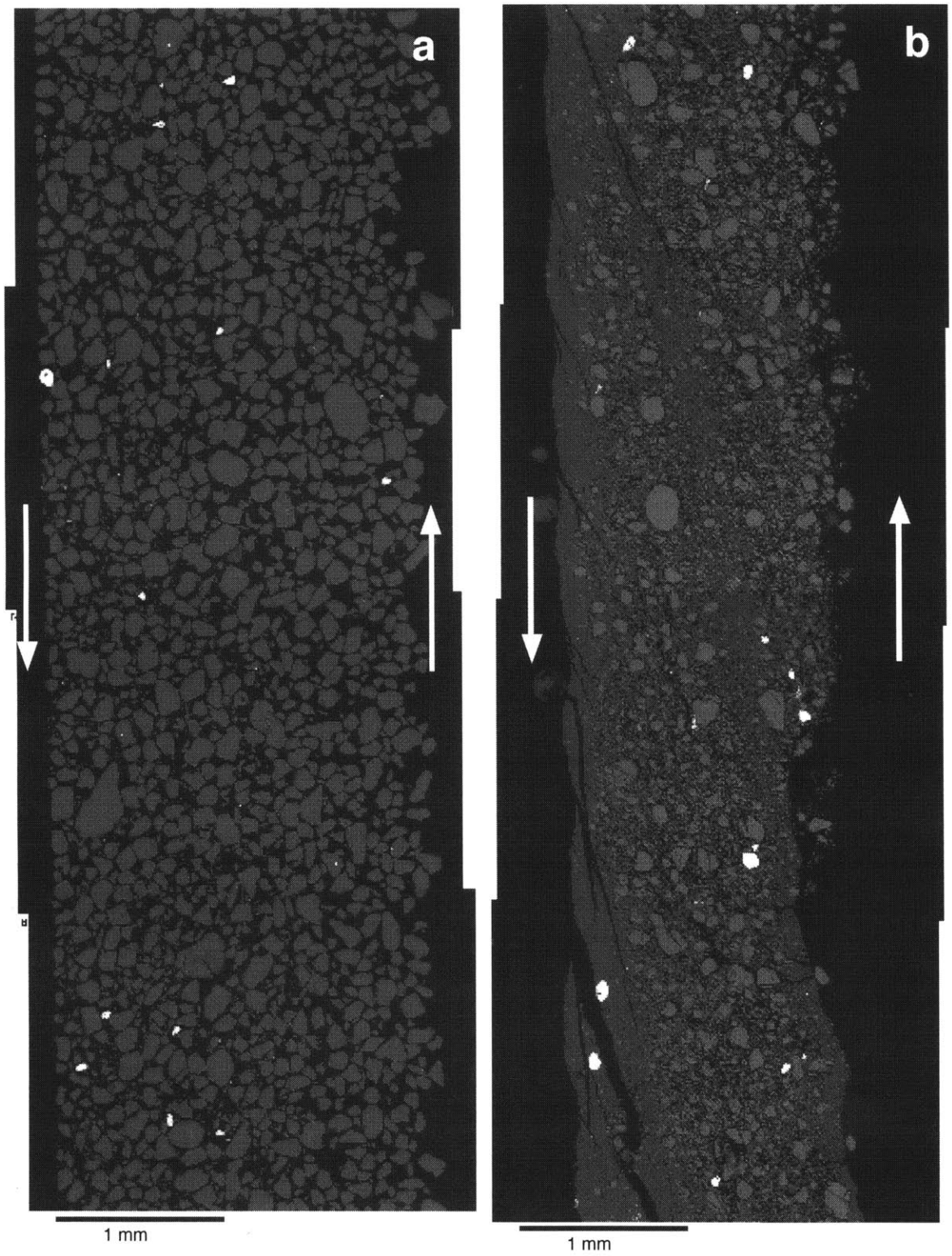

Figure 4.7. SEM photomicrograph of angular gouge deformed at: a) σ_n = 5 MPa; b) σ_n = 50 MPa [redrawn after *Mair and Marone,* 2000]. In both cases, slip = 20 mm. Arrows indicate the sense of shear. Note the development of a distinct fabric in b) not seen in a).

the distinct fabric developed at higher stress (Figure 4.7b). The structures in Figure 7b are typical of those observed in all tests conducted at $\sigma_n > 25$ MPa.

SEM photomicrographs of initially narrow PSD spherical particles (Figure 4.2b) deformed at normal stresses of σ_n = 25 MPa and σ_n = 40 MPa are presented in Figure 4.8 a) and b), respectively. Similar to Figure 4.7, the low normal stress test indicates little grain fracture and no fabric evolution whereas the higher normal stress test exhibits a well developed fabric. This fabric is highlighted by differences in grain size distributions and although some relic spherical grains survive intact, many grains are no longer spherical.

In both gouges at low normal stress (Figure 4.7a, 4.8a) grain size is representative of the undeformed material (Figure 4.2a and b respectively). No clear microstructural signature of shearing is preserved, even after shear strains of ~12 (20 mm shear displacement). This indicates that few grains fracture and that non-destructive processes such as grain rolling and sliding accommodate the majority of deformation under these conditions. In contrast, significant fracture and grain size reduction clearly occurs at higher stress (Figure 4.7b, 4.8b). The resulting fabric is characterized by linear zones of intense comminution in boundary and Riedel orientation separated by relic zones of less deformed survivor grains. These features are characteristic of natural fault zones [*Logan et al.*, 1979; *Sammis et al.*, 1986; *An and Sammis*, 1994] and the comminution fabrics are interpreted as zones of concentrated shear. Previous laboratory work on angular gouge [*Marone and Scholz*, 1989] and field observations [*Sammis et al.*, 1986, 1987; *An and Sammis*, 1994] indicate that a wide fractal PSD typically develops in these localized shear zones. In the next section we isolate and consider the influence of PSD on friction for a constant grain shape.

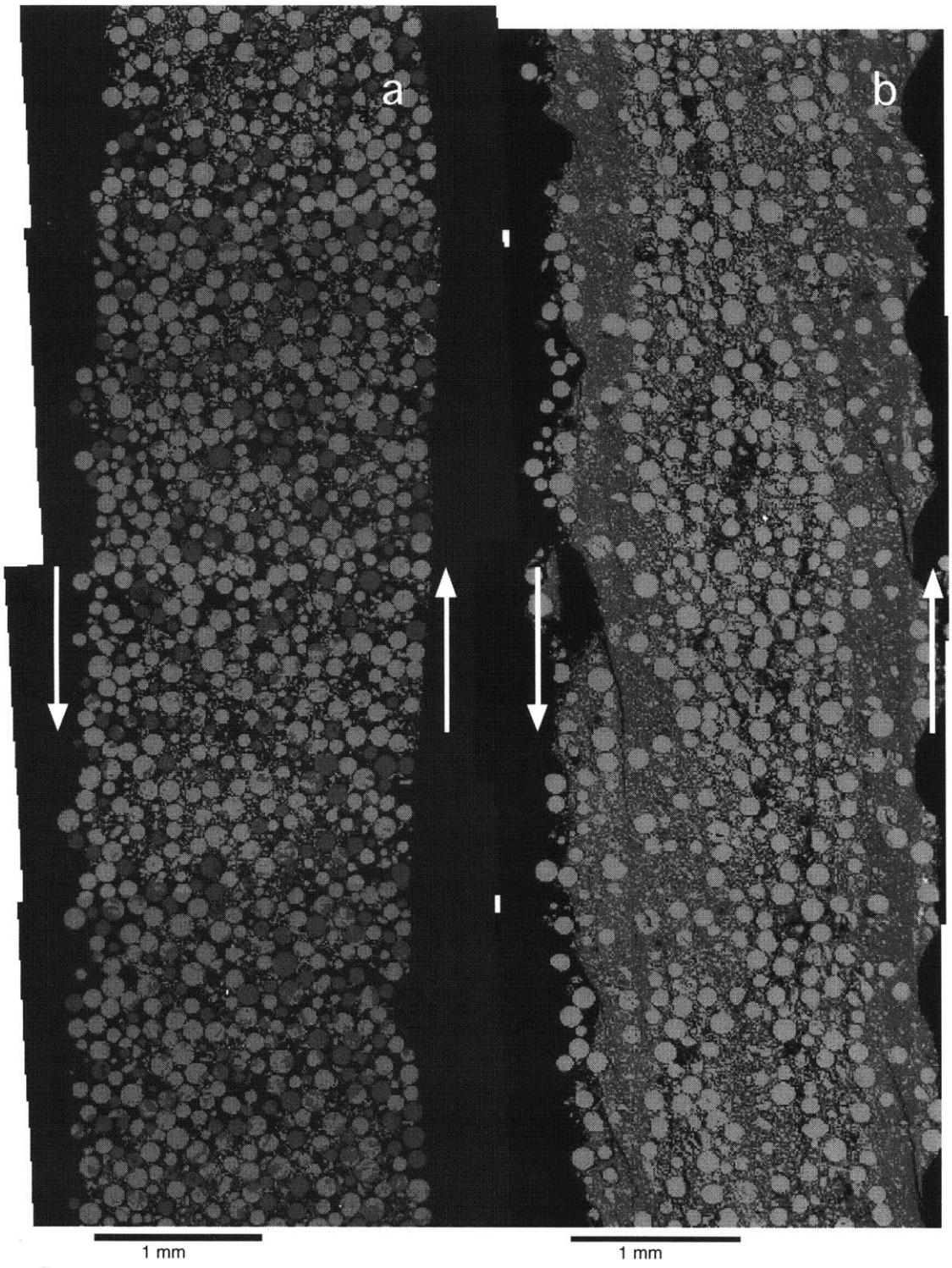

Figure 4.8. SEM photomicrograph of spherical gouge deformed at a) σ_n = 25 MPa and b) σ_n = 40 MPa. Slip = 20 mm in both cases and the sense of shear is indicated by arrows. Note the development of a fabric in b) comparable to Figure 7b).

4.3.3. Influence of particle size distribution

Our data show that spherical grains are markedly different than angular grains, exhibiting both lower friction and unstable stick-slip behavior (Figure 4.3). However, initially spherical material becomes stable and strengthens, approaching the behavior of an angular gouge as grain fracture and strain localization become significant. It is important to understand the processes responsible for this evolution. Candidate processes include: 1) changes in grain size distribution due to comminution; 2) particle roughening as spherical grains become more angular; or 3) the development of a strain localization fabric.

We test these process by changing the initial PSD for spherical particles. We use a log normal PSD, which is intended to approach the PSD of a well developed shear band [after *An and Sammis,* 1994] (Figure 4.2c). To isolate the influence of PSD, we deform this material at low stress where grains do not fracture; hence grain shape is constant throughout the test. If grain roughening due to comminution is the key factor, independent of PSD, we expect the wide PSD gouge will show the same frictional behavior as the narrow PSD gouge. If PSD is the important factor then we expect to see strain hardening and stabilization in the wide PSD gouge.

Our results (Figure 4.9) show that the coefficients of sliding friction for narrow and wide PSD spherical material are identical and measurably lower than that for angular gouge (Figure 4.3). Unlike the narrow PSD spherical particles, frictional sliding of wide PSD spheres is stable (Figure 4.9). This indicates that PSD is critical in achieving stable sliding but that angular grains are necessary to reach typical laboratory friction values of $\mu \sim 0.6$. We now discuss possible mechanisms for these observations.

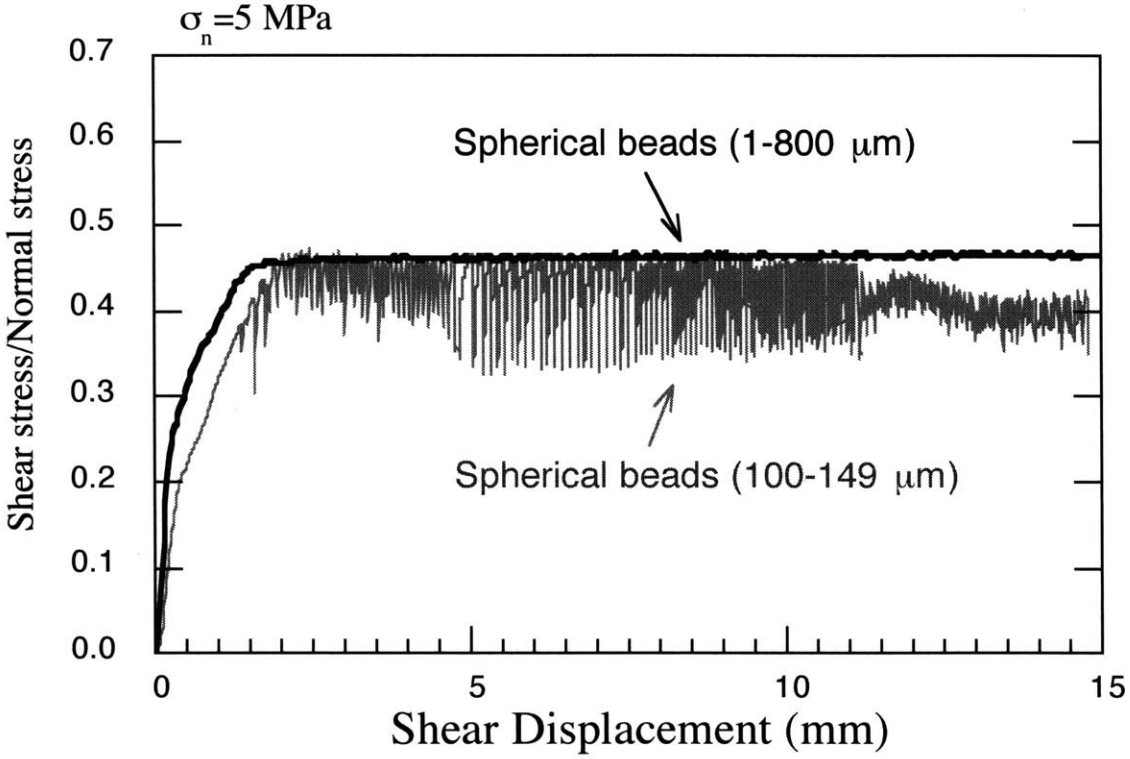

Figure 4.9. Friction versus shear displacement for two spherical gouges of narrow and wide size distributions deformed at σ_n = 5 MPa. A wide PSD promotes stable sliding at a level of μ~0.45 whereas gouge composed of a narrow PSD exhibits stick slip sliding. Note that the peak frictional strength during stick-slip (narrow PSD) is equal to the stable frictional strength of the wide PSD gouge.

4.4. Discussion

4.4.1. Frictional strength

The macroscopic frictional strength we measure for angular quartz sand ($\mu \sim 0.6$) is comparable to that obtained in previous laboratory experiments. One of our most interesting observations, however, is that the friction level of a granular material composed of spherical grains is significantly lower than this ($\mu \sim 0.45$). The friction levels of spherical beads with both a narrow and broad particle size distribution are identical.

This suggests that the kinematics of the angular and spherical particles are distinct. One explanation is that spherical grains accommodate strain preferentially by rolling, a highly efficient translation mechanism, leading to reduced macroscopic friction. Rolling is inhibited in angular grains and thus translation must be accommodated by sliding and dilation. Our data indicate that spherical gouge is significantly weaker than angular gouge, but that macroscopic friction is still greater than 0.4.

Interparticle friction (μ_p) of individual grains influences macroscopic sliding friction [*Morgan,* 1999]. It is tempting to account for the dramatic differences we observe in friction by invoking differences in μ_p of the angular and spherical material; however, this alone is inadequate to explain our observations. We reason that the interparticle friction for spherical particles that survive intact (Figure 4.8a) and those that fracture at higher normal stress (Figure 4.8b) is essentially comparable and would lead to a similar macroscopic friction level if grain sliding alone were operating. However, Figure 6 indicates that the macroscopic friction level of spherical particles increases as grain comminution ensues, suggesting that an increase in angularity of the grains is a stronger effect. We suggest that as shape evolves due to comminution, the proportion of rolling to sliding decreases leading to higher friction. In

addition, over the range studied, particle size distribution of spheres does not appear to influence frictional strength. Hence our observation of increased friction with progressive grain comminution is not due to evolution of PSD. Thus, frictional strength appears to be a strong function of grain shape but not PSD during the shear of granular materials.

4.4.2. Frictional stability

For the stiffness of our shearing apparatus, angular gouge slides stably in all experiments, consistent with previous studies under similar conditions. We show that a narrow PSD of spherical material is unstable exhibiting repetitive stick slip whereas angular gouge and spherical material with a wider PSD are stable. In addition, stabilization of initially spherical (unstable) gouge occurs with grain comminution.

We suggest that frictional stability is related to the nature of stress accommodation across a granular layer undergoing shear (Figure 4.10). We invoke the concept that stress chains or grain bridges preferentially support load in a sheared granular material [*Sammis et al.,* 1987; *Cates et al.*, 1998]. This model has recently proved useful in explaining observations from numerical modeling [*Morgan,* 1999] and laboratory experiments [*Karner and Marone,* 2001]. We propose that stress can alternatively be supported by diffuse webs of load bearing particles, each particle carrying low to moderate stress; or sets of highly localized particle chains where fewer particles are involved but each experience much higher local contact stresses (Figure 4.10a). Importantly, both features are transient and persist only while they are favorably orientated (Figure 4.10 b, c, d).

Our data can be explained by a model in which stress chains fail when they deviate beyond a critical angle (ϕ_c). Macroscopic boundary stresses are supported by systems of stress chains,

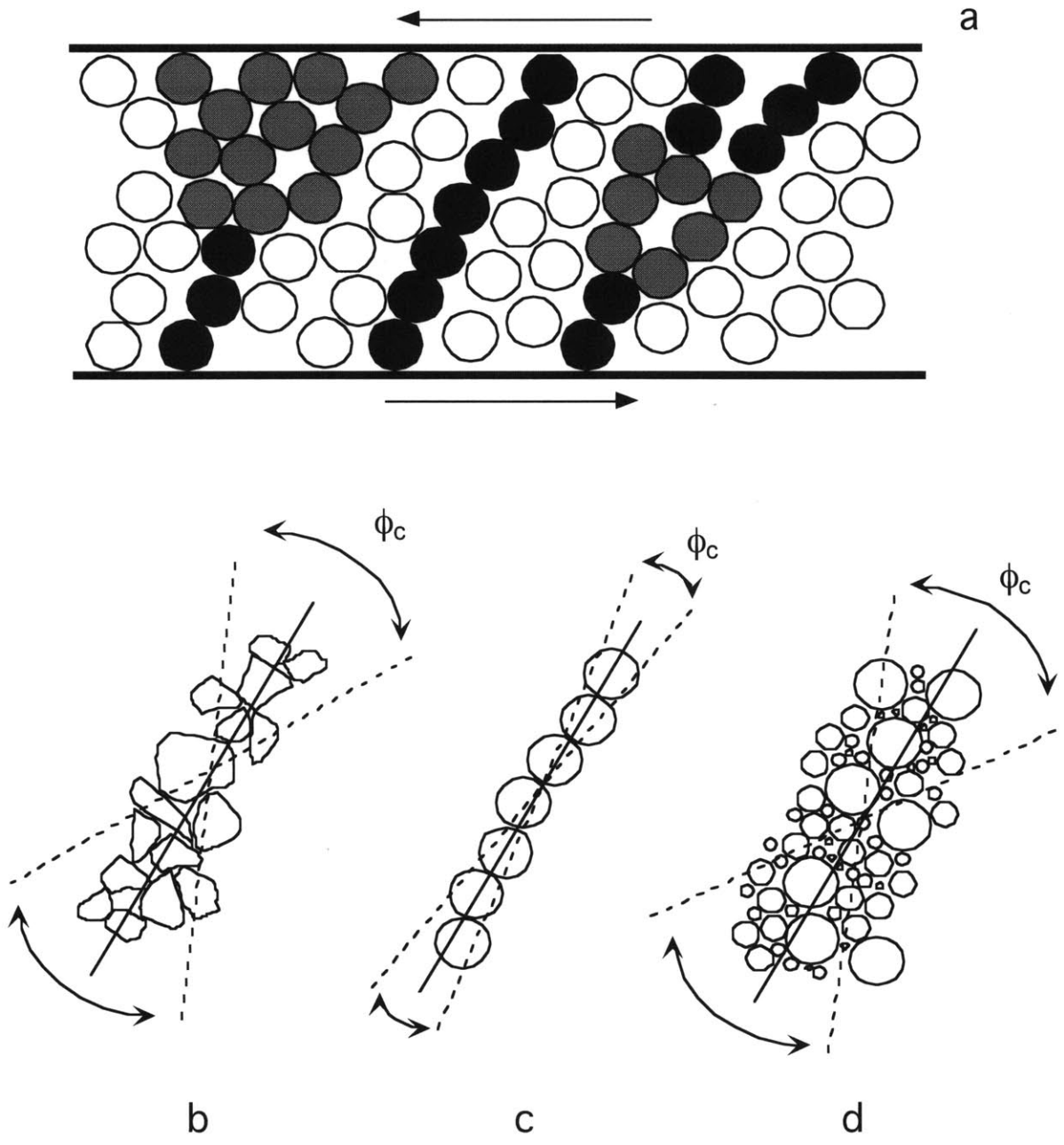

Figure 4.10: (a) Illustration of possible force chain geometries for a granular layer under shear. Black indicates particles bearing high load; gray indicates low to moderate load; and white indicates spectator particles not bearing appreciable load [redrawn after *Cates et al.*, 1998]. Note that stress can be supported by sets of localized chains of highly stressed particles (middle) or by diffuse webs of particles under lower stress (left, right). Examples of stress chains are shown for (b) angular gouge; (c) narrow PSD spherical particles; and (d) wide PSD spherical particles. Solid line indicates optimal chain orientation and dotted lines demark range of possible stable orientations. ϕ_c defines a critical angle for stress chains; outside this range stress chains fail by interparticle slip or rolling. Note that (b) and (d) have larger ϕ_c than (c). In addition, contact stresses are highest for (c).

which fail and reform repeatedly during shear. We posit that the critical angle (ϕ_c) is greater for diffuse stress chains than localized stress chains (Figure 4.10). A population of coexisting diffuse stress chains (Figure 4.10 b and d) can have a range of orientations within ϕ_c. In contrast, for localized chains, critical angle (ϕ_c) is much smaller (Figure 4.10c) so a population of coexisting stress chains have very similar orientations. These chains are likely to collapse under approximately the same shear displacement giving synchronous failure and a macroscopic stress drop.

The nature of stress chains depends on grain characteristics and interactions such as co-ordination number Z (i.e. the number of other grains contacting each particle). Large Z implies diffuse stress chains (each particle carrying moderate load) whereas small Z corresponds to localized stress chains (comprised of highly stressed particles). Numerical simulations [*Morgan,* 1999] indicate that co-ordination number increases and average contact force decreases with increasing fractal dimension (i.e. wider PSD) of gouge. We suggest that in our experiments angular gouge and wide PSD spherical particles have large Z and develop diffuse stress chains (Figure 4.10b and d) whereas narrow PSD spherical particles have small Z and therefore develop highly concentrated stress chains (Figure 4.10c). When the narrow PSD gouge is sheared, these localized stress chains fail catastrophically due to geometric incompatibility, leading to dynamic stress drop and unstable stick-slip sliding.

Our ideas are consistent with those of *Sammis et al.* [1987] who showed that similar sized neighboring particles (e.g. our narrow PSD gouge) have high probability of failure due to high individual contact stresses. In contrast, gouge with a range of particle sizes (e.g. our wide PSD gouge) can successfully distribute load over many particles, reducing stresses at individual contacts, in effect cushioning large particles and making failure less likely. In addition,

instability is more likely for highly stressed particle chains since for a given local stiffness stick-slip is favored by higher normal stress [*Dieterich*, 1978].

4.4.3. Comparison with numerical models:

Spherical particles show lower friction than identical experiments on angular gouge. Our results agree qualitatively with the numerical experiments of *Mora and Place* [1999] where grain shape is changed by bonding particles together. They also report that rougher particles exhibit higher macroscopic friction. The friction levels we report for spherical material (μ ~0.45) approach the levels often observed in numerical simulations where idealized circular particles are modeled [*Morgan,* 1999; *Aharonov and Sparks*, 1999; *Mora and Place,* 1998, 1999]. However, in the numerical models friction is often 0.2 to 0.3, which is well below our observations. This may be a consequence of numerical work generally being done in 2-D rather than 3-D [*Morgan,* 1999].

Morgan [1999, Figure 4.2] shows that an increase in fractal dimension D (i.e. wider PSD) promotes stable sliding whereas low D (i.e. narrow PSD) has more numerous and larger stress drops. Our results are consistent, the stress drops we observe being greater with narrower PSD and in fact absent for wider PSD gouge (Figure 4.9).

4.5. Conclusions

Grain characteristics significantly affect the macroscopic friction of a granular material under shear. Gouge composed of smooth spherical particles has markedly lower frictional strength than angular particles. Frictional stability is sensitive to the geometry of stress distribution throughout sheared layers and depends on particle size distribution and angularity. We show that

the first order discrepancies between laboratory and numerical studies may be explained by the differences in initial grain shape and loading regime. Our results indicate that gouges in natural faults may be significantly stronger than those predicted by numerical models using idealized smooth particles.

4.6. References for chapter 4

Aharonov, E., and D. Sparks, Rigidity phase transition in granular packings, *Phys. Rev. E, 60,* 6890-6896, 1999.

An, L-J., and C.G. Sammis, Particle size distribution of cataclastic fault materials from Southern California: A 3-D study, *Pure Appl. Geophys., 143*, 203-227, 1994.

Berman, A.D., W.A. Ducker, and J.N. Israelachvili, Experimental and theoretical investigations of stick-slip friction mechanisms, *in Physics of Sliding Friction,* edited by B.N.J. Persson and E. Tosttati, pp. 51-67, Kluwer, Dordrecht, 1996.

Cates, M.E., J.P. Wittmer, J-P. Bouchaud, and P. Claudin, Jamming, force chains, and fragile matter, *Phys. Rev. Lett., 81*, 1841-1844, 1998.

Dieterich, J.H., Modeling of rock friction: 1. Experimental results and constitutive equations, *J. Geophys. Res., 84*, 2161-2168, 1979.

Dieterich, J.H., Time-dependent friction and the mechanics of stick-slip, *Pure Appl. Geophys., 116*, 790-805, 1978.

Karner, S.L., and C. Marone, Frictional restrengthening in simulated fault gouge: Effect of shear load perturbations, *J. Geophys. Res., 106,* 19319-19337, 2001.

Karner, S.L., and C. Marone, Effects of loading rate and normal stress on stress drop and stick-slip recurrence interval, *in Geocomplexity and the Physics of Earthquakes*, edited by J.B.

Rundle, D.L. Turcotte, and W. Klein, AGU Geophysical Monograph Series, Vol. 120, pp. 187-198, 2000.

Karner, S.L., and C. Marone, The effect of shear load on frictional healing in simulated fault gouge, *Geophys. Res. Lett., 25,* 4561-4564, 1998.

Logan, J.M., M. Friedman, N. Higgs, C. Dengo, and T. Shimamoto, Experimental studies of simulated gouge and their application to studies of natural fault zones, *Proc. Conf. VIII, Analysis of Actual Fault Zones in Bedrock, National Earthquake Hazards Reduction Program, April 1-5, Menlo Park, Ca.*, pp. 305-343, 1979.

Mair, K. and C. Marone, Shear heating in granular layers, *Pure Appl. Geophys., 157,* 1847-1866, 2000.

Mair, K. and C. Marone, Friction of simulated fault gouge for a wide range of velocities and normal stresses, *J. Geophys. Res.,* 28899-28914, 1999.

Marone, C., Laboratory-derived friction laws and their application to seismic faulting, *Annu. Rev. Earth Planet. Sci., 26,* 643-696, 1998.

Marone, C., and C.H. Scholz, Particle-size distribution and microstructures within simulated fault gouge, *J. Struct. Geology, 11,* 799-814, 1989.

Mora, P., and D. Place, The weakness of earthquake faults, *Geophys. Res. Lett., 26,* 123-126, 1999.

Mora, P., and D. Place, Numerical simulation of earthquake faults with gouge: toward a comprehensive explanation for the heat flow paradox, *J. Geophys. Res., 103,* 21067-21089, 1998.

Mora, P., and D. Place, Simulation of the frictional stick-slip instability, *Pure Appl. Geophys., 143,* 61-87, 1994.

Morgan, J.K., Numerical simulations of granular shear zones using the distinct element method: I Shear zone kinematics and the micromechanics of localization, *J. Geophys. Res., 104,* 2703-2719, 1999.

Morgan, J.K., and M.S. Boettcher, Numerical simulations of granular shear zones using the distinct element method: II Effects of particle size distribution and interparticle friction on mechanical behavior, *J. Geophys. Res., 104,* 2721-2732, 1999.

Mueth, D.M., G.F. Debregeas, G.S. Karczmar, P.J. Eng, S.R. Nagel and H.M. Jaeger, Signatures of granular microstructure in dense shear flows, *Nature, 406*, 385-388, 2000.

Pisarenko, D., and P. Mora, Velocity weakening in a dynamical model of friction, *Pure Appl. Geophys., 142*, 447-466, 1994

Richardson, E. and C. Marone, Effects of normal force vibrations on frictional healing, *J. Geophys. Res., 104*, 28859-28878, 1999.

Sammis, C.G., G. King, and R. Biegel, The kinematics of gouge deformation, *Pure Appl. Geophys., 125*, 777-812, 1987.

Sammis, C.G., R.H. Osborne, J.L. Anderson, M. Banerdt and P. White, Self-similar cataclasis in the formation of fault gouge, *Pure Appl. Geophys., 124*, 51-77, 1986.

Scholz C.H., Earthquakes and friction laws, *Nature, 391,* 37-42, 1998.

Scott, D.R., Seismicity and stress rotation in a granular model of the brittle crust, *Nature, 381*, 592-595, 1996.

Wong, Tf., Y. Zhao, 1990, Effects of load point velocity on frictional instability behavior, *Tectonophysics, 175,* 177-195.

Table 4.1. Experiments

Experiment	Grain shape	Grain diameter μm	σ_n MPa	V range μm/s	Sliding
		Non-fracture regime			
m290	Ang	50-150	5	5000	stable
m302	Ang	50-150	5	5000	stable
m349	Sph	105-149	5	0.1-300	stick slip
m425	Sph	105-149	5	10-1000	stick slip
m428	Sph	105-149	5	10-1000	stick slip
m433	Sph	105-149	5	0.1-10	stick slip
m429	Sph	105-149	25	10-1000	stick slip
m431	Sph	105-149	25	10-1000	stick slip
m437	Sph	105-149	25	0.1-100	stick slip
m439	Sph	105-149	25	0.1-200	stick slip / stable
m351	Sph	105-149	25	10	stick slip
m446	Sph	1-800	5	10	stable
m444	Sph	1-800	5	1-20	stable (1 stress drop)
m445	Sph	1-800	5	10-20	stable (1 stress drop)
		Fracture regime			
m268	Ang	50-150	25	1000	stable
m490	Ang	50-150	40	10	stable
m291	Ang	50-150	50	500	stable
m426	Sph	105-149	40	10-1000	stick slip / stable
m357	Sph	105-149	(40) 25	10	stick slip / stable

Initial gouge layer thickness 3 mm.
σ_n = Normal stress, V = Velocity.

5. The effect of particle dimensionality on granular friction in laboratory shear zones

Synopsis: To match the boundary conditions of numerical models and to examine the effect of particle dimensionality on granular friction, we conducted laboratory experiments on fused quartz glass and pasta rods sheared in 1-D and 2-D configurations, soda lime glass beads (3-D), and angular quartz sand (rough 3-D). Applied normal stress was below the particle crushing strength. We find that friction varies systematically as a function of granular particle dimension. The coefficient of friction during stable sliding for 1-D, 2-D, smooth 3-D, and rough 3-D particles is approximately 0.15, 0.3, 0.45, and 0.6, respectively. Frictional strength of 2-D layers exceeds 1-D friction by an amount associated with dilatancy and rolling in 2-D. For smooth, non-breaking particles we show that 3-D granular friction exceeds 2-D friction by the amount of interparticle friction on the out-of-plane particle contacts that do not exist in 2-D. Data from our 2-D experiments are remarkably similar to numerical results based on 2-D particle dynamic simulations. Our data indicate that granular friction scales with particle dimensionality and that application of numerical models of granular friction to tectonic faults and fault gouge will require computations involving rough, 3-D particles.

5.1. Background

Numerical models provide unique insight into the micro-mechanics of granular shear deformation and offer great potential for bridging the gap between laboratory conditions and scales and those of tectonic faults. However, existing numerical and laboratory studies of granular friction show significant discrepancies [e.g., *Mora and Place*, 1999]. Numerical works show lower frictional strength, larger variations in friction with strain, and lower heat production than laboratory experiments. These differences need to be understood before numerical and laboratory results can be combined and applied to a wider range of conditions.

Few studies have been conducted to investigate the effects of initial and boundary conditions on granular friction. Most numerical studies have used smooth 2-D particles [e.g., *Mora and Place*, 1998, 1999; *Morgan,* 1999; *Morgan and Boettcher,* 1999; *Aharonov and Sparks*, 1999], whereas laboratory experiments have focused on natural materials composed of rough, sub-angular particles such as found in natural fault gouge [e.g., *Sammis et al.*, 1986]. Laboratory studies show that particle shape, roughness, and fracture have important effects on granular friction [e.g., *Sammis et al.*, 1987; *Losert et al.*, 2000; *Mair et al. 2002*]. At present, these factors have not been studied in numerical models due to computational limitations.

In this paper we report on laboratory experiments designed to match the boundary conditions of numerical models. We investigate the effect of particle dimensionality and shape using direct shear experiments. We find that friction varies systematically with particle dimension and that the discrepancy between numerical and laboratory studies may be explained by differences in initial and boundary conditions.

5.2. Experimental Methods

All experiments reported in this study were performed in a double-direct shear apparatus in which two layers are sheared simultaneously between three rough, steel forcing blocks (Figure 5.1). Normal stress was maintained constant by servo-control. The main set of experiments was carried out at low normal stresses σ_n (1 MPa for rods, 5 MPa for beads and sand) so that particle fracture was minimal (Table 5.1, end of chapter). Additional experiments were performed in the fracture regime at σ_n of 25-40 MPa. Shear load was applied to the center block by imposing a constant displacement rate. Stresses and displacements were all recorded at 10 kHz and averaged to 10 samples/s. Measurement resolution was ±0.01 MPa and ±0.1 μm.

Test samples consisted of fused-quartz glass rods, dried strands of standard semolina pasta (Ronzoni #12 Angel Hair), soda-lime glass beads, and angular quartz powder (Table 5.1). Both types of rods and the glass beads are smooth at the particle scale. The quartz was sub-angular Ottawa sand, which is > 99% SiO_2 as supplied by the US Silica Co. We used Natural Grain product F-110, which has median particle size of 110 μm. Soda-lime glass beads had median particle size of 110 μm and two size ranges were studied (Table 5.1). The quartz and pasta rods were 1 mm in diameter. Nominal friction contact dimension was 10 cm x 10 cm in all experiments (Figure 5.1).

Layers of particles were constructed in a leveling jig to ensure reproducible layer thickness. Sand and glass bead layers were constructed to be 3 mm thick, and layers of rods were 7 mm thick. The rods were arranged in two configurations (Figure 5.1). Rods with the long axis perpendicular to shear were used to simulate 2-D granular shear. In this configuration, shear involves two degrees of freedom: motion in the shear direction and motion perpendicular to the shear plane causing layer dilation or compaction. Rods were also

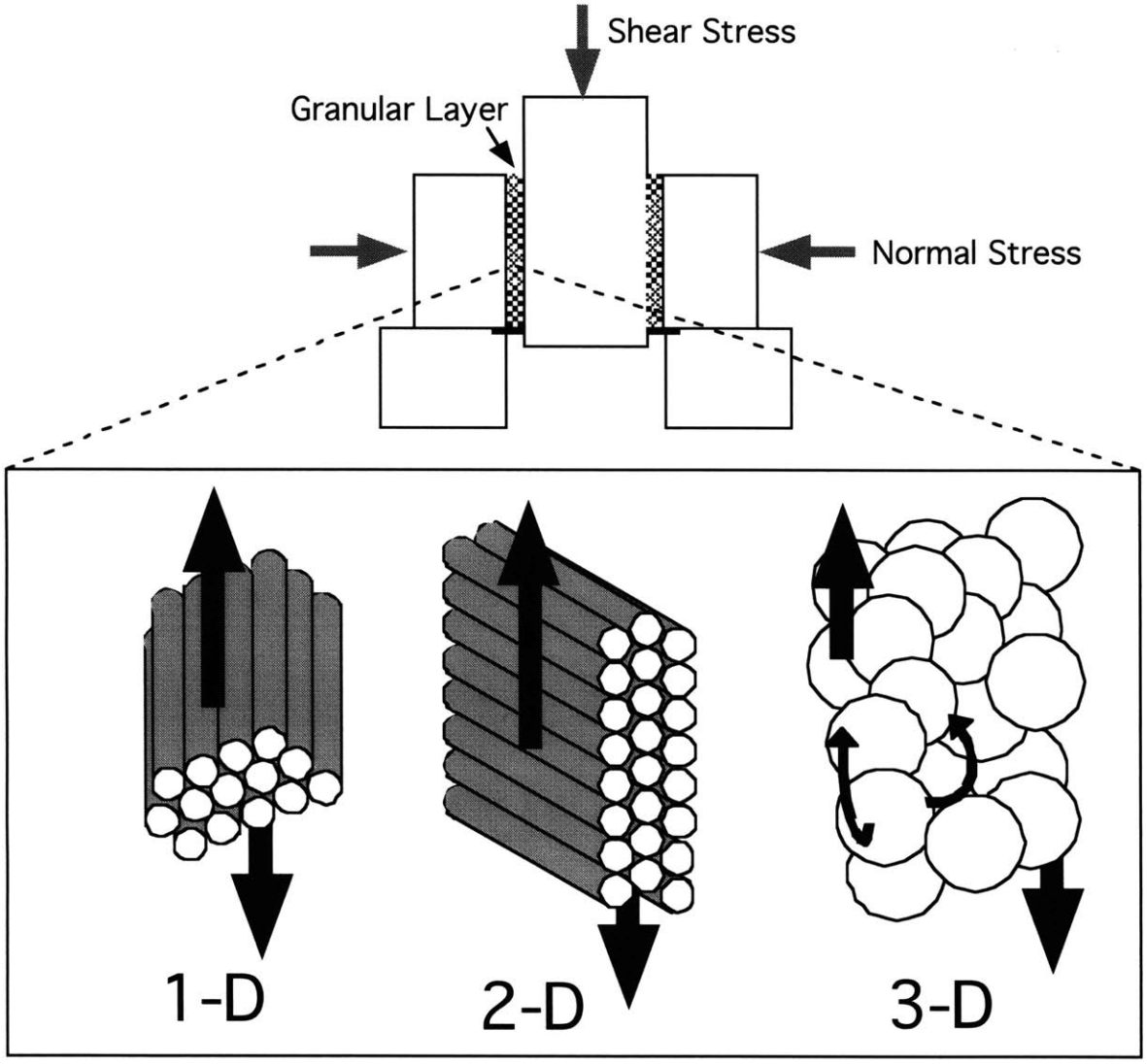

Figure 5.1. Laboratory configuration to study the role of particle dimensionality in granular friction. Biaxial shear apparatus (top) provides controlled deformation under applied normal stress. Rods and spheres are oriented to produce 1-D, 2-D, or 3-D conditions in double direct shear. In the 1-D case, shear is accommodated by grain boundary slip parallel to the shear direction. For a 2-D granular layer, shear occurs by rolling or sliding and dilation (or compaction) perpendicular to the shear direction. In the 3-D case particles have components of motion in all 3 directions. Note that 2-D shear involves rolling or sliding along the entire length of a rod, whereas in 3-D rolling or sliding must occur simultaneously on in-plane and out-of-plane contacts.

sheared parallel to their axes to create a 1-D granular case (Figure 5.1). 1-D shear involves only one degree of freedom: grain boundary sliding in the direction of shear. Motion perpendicular to shear is not excluded, but dilation or compaction is not required for shear. The 1-D rods were cut longer than the side blocks to ensure that the nominal area of frictional contact remained constant as the rod layer was sheared. For each configuration of particles, we report the mean sliding friction for a load point velocity of 10 μm/s (Table 5.1). For the 2D configuration, we include the standard deviation of sliding friction.

5.3. Experimental Results

We found that the frictional strength of 3-D particles ranged from 0.45 for smooth beads to 0.6 for angular sand (Table 5.1), in agreement with previous work [*Mair et al.*, 2002]. In the 2-D shear configuration, both pasta and quartz rods exhibited stable sliding and large fluctuations in friction with shear (Figure 5.2a). We report mean sliding friction μ_{ss} over the displacement interval 6-10 mm and, for the 2-D layers, the standard deviation of friction fluctuations in that interval (Table 5.1). Sliding friction for 2-D layers of quartz rods fluctuated in the range 0.14 to 0.36 after initial loading (Figure 5.2a). The amplitude of friction variations for 2-D pasta rods was smaller, with friction ranging from 0.25 to 0.31. In both cases, the dominant wavelength of friction fluctuations was roughly 2 mm, or twice the rod diameter. In contrast, angular quartz sand exhibited a constant coefficient of sliding friction of 0.63.

We compared the natural variations in 2-D friction to time-dependent changes associated with healing and static recovery [e.g., *Marone*, 1998]. Figure 5.2a shows two slide-hold-slide tests in which holds of 100 s duration were imposed. Time-dependent

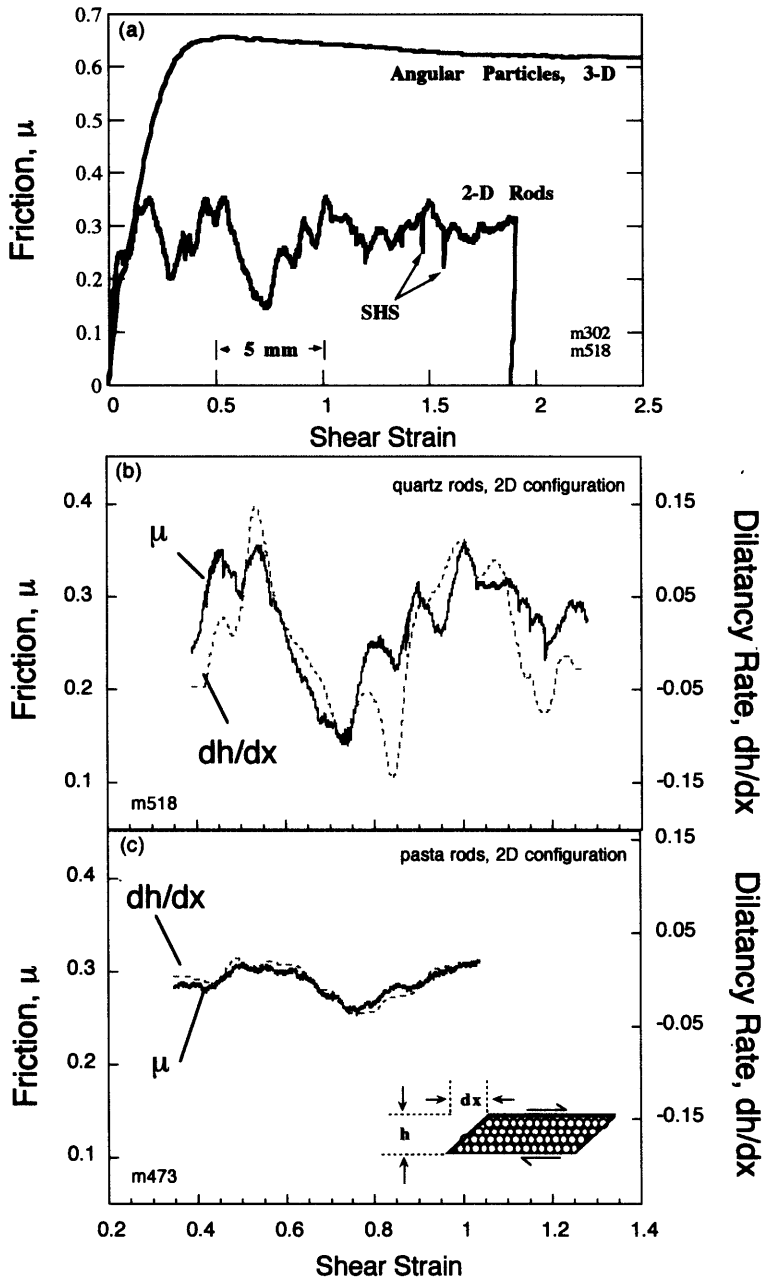

Figure 5.2. (a) Laboratory friction data for granular layers composed of fused quartz glass rods (2-D) and granular quartz (3-D). The coefficient of sliding friction is higher in 3-D than in 2-D and layers of 3-D particles shear at a constant frictional strength, whereas 2-D shear involves large fluctuations in friction with shear. Arrows labeled SHS denote time dependent healing tests (100 s hold periods were imposed followed by continued shear) and show that natural fluctuations in 2-D friction are large compared to rate/state friction effects. (b) 2-D quartz rod and (c) pasta friction data are compared with measurements of the rate of layer thickness change with displacement. Positive values of dh/dx indicate layer dilation (see inset). Note the high degree of correlation between frictional strength and dh/dx, consistent with the importance of volumetric work in the total energy budget for 2-D granular shear.

frictional healing is measured by the increase in peak frictional strength after shear resumes relative to initial sliding friction. We find that healing is small compared to the natural variations of friction for non-breaking rods in the 2-D configuration.

Measurements of layer thickness show that 2-D friction variations correlate strongly with dilatancy rate *dh/dx* (Figure 5.2b, 5.2c). A positive dilatancy rate corresponds to an increase in layer thickness and negative *dh/dx* indicates compaction. We determined dilatancy rate using a least squares best fit in a moving window. Window sizes from 100 to 500 points (shear strain of 0.015 to 0.085) yield correlation coefficients of 0.72-0.76 during steady-state shearing for quartz rods (Figure 5.2b) and 0.90 to 0.95 for pasta (Figure 5.2c). Since our 2-D particles do not fracture, layers must dilate or compact against the applied normal stress to accommodate shearing. The macroscopic frictional strength τ of a granular material depends linearly on the sum of work to overcome interparticle friction μ_p (this includes sliding and rolling at constant volume on all planes of contact) and work of volume strain [*e.g., Mead,* 1925; *Bishop*, 1954; *Marone et al.*, 1990; *Geminard et al,* 1999],

$$\tau = \sigma\left(\mu_p + d\theta / d\gamma\right) \tag{5.1}$$

where is θ volume strain, γ is shear strain, and σ is effective normal stress. Taking $d\theta = dV/V$ and $d\gamma = dx/h$, where V is layer volume given by thickness h and area A, and assuming that volume change in the plane of the layer is negligible, Equation 5.1 reduces to:

$$\tau = \sigma\left(\mu_p + dh / dx\right). \tag{5.2}$$

Since the measured frictional strength in our experiments is τ/σ, Equation (5.2) predicts that friction and dilatancy rate will correlate strongly, as we observe for 2-D friction (Figure 5.2b, 5.2c). We find that variations in friction and dilatancy rate have the same amplitude, which

suggests that the observed variations in shear strength $\tau(\gamma)$ are attributable to variations in $dh/dx(\gamma)$.

Shear of 2-D particles can be accommodated by grain boundary slip or rolling operating in concert with dilation or compaction. We isolated the mechanism of grain boundary sliding by conducting 1-D granular shear experiments on smooth rods. Friction is significantly lower in 1-D than in 2-D (Figure 5.3). Measurements of layer thickness show that 1-D shear occurs at constant volume, with dh=0 throughout sliding.

The frictional strength of 1-D particles is 0.14-0.19 and is significantly less variable during shear than 2-D particles (Figure 5.3). The frictional strength of smooth glass beads is intermediate between the 2-D case and the angular particles of quartz sand. The large friction fluctuations in 2-D are not present in the 1-D or 3-D cases. Our data show that sliding friction varies systematically with granular particle dimension (Figure 5.3b). The effect of particle roughness is shown by the relationship between sand and glass beads. For smooth, non-breaking particles there is a linear dependence of macroscopic frictional strength on granular particle dimension (Figure 5.3b).

We compare the friction data from our 2-D experiments with the numerical results obtained by *Morgan* [1999], who used the particle dynamics method and 2-D particles (Figure 5.4). The similarity between the laboratory and numerical results is remarkable. Both data sets show that friction fluctuates about 0.3 and fluctuations correlate strongly with changes in positive (dilation) and negative (compaction) changes in dilatancy rate (e.g., Figure 5.2b).

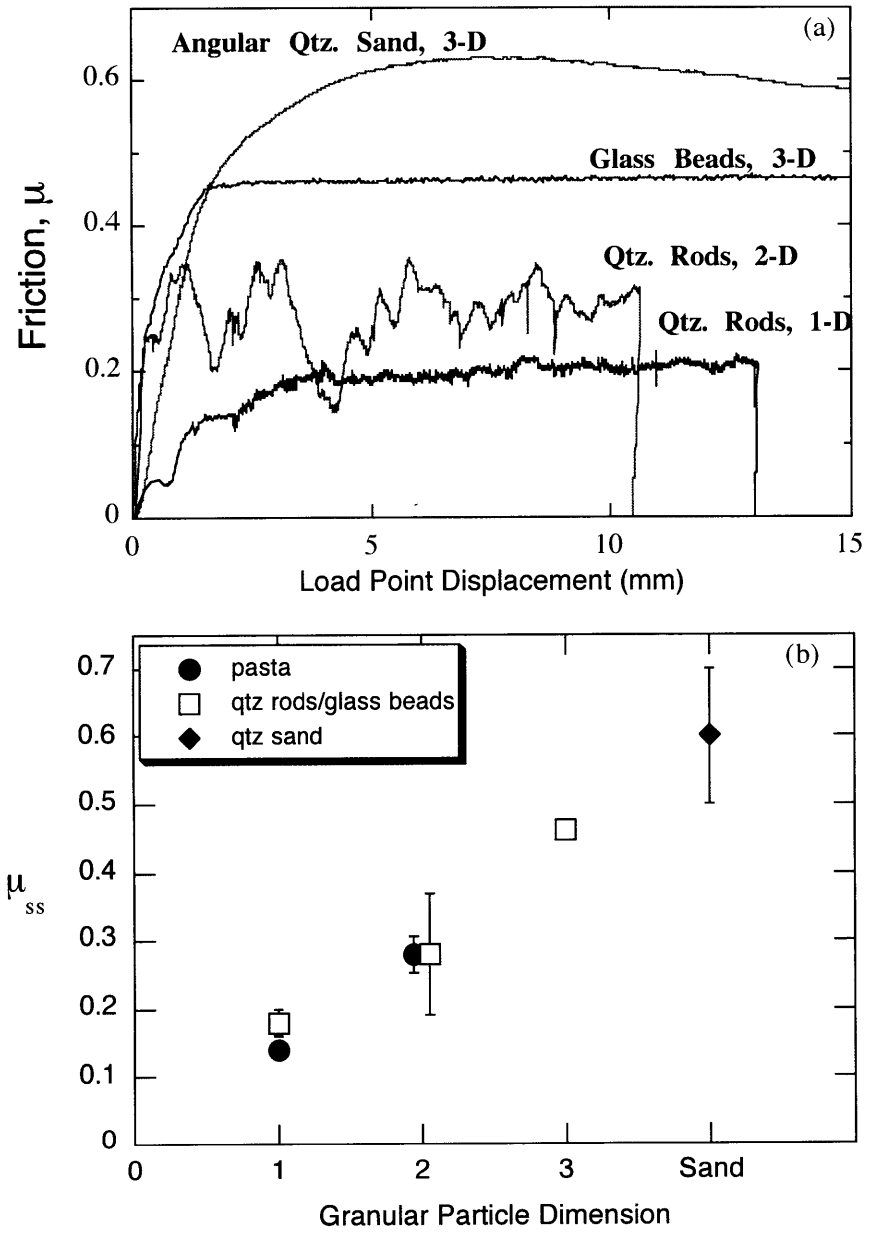

Figure 5.3. (a) Friction data for four types of granular layers. The coefficient of sliding friction is highest for angular particles and decreases systematically for smooth particles (glass beads) and rods sheared in the 2-D and 1-D configurations. (b) The average value of stable sliding friction is plotted against particle dimension, with vertical bars representing friction fluctuations for the 2-D case and a range of observed friction values for sand. Friction decreases systematically as a function of granular particle dimension. We posit that 3-D granular friction exceeds 2-D friction by the amount necessary for interparticle slip and rolling on the out-of-plane particle contacts that do not exist in 2-D. Rolling and grain boundary sliding are inhibited by particle roughness, increasing the frictional strength of angular sand particles compared to smooth 3-D beads.

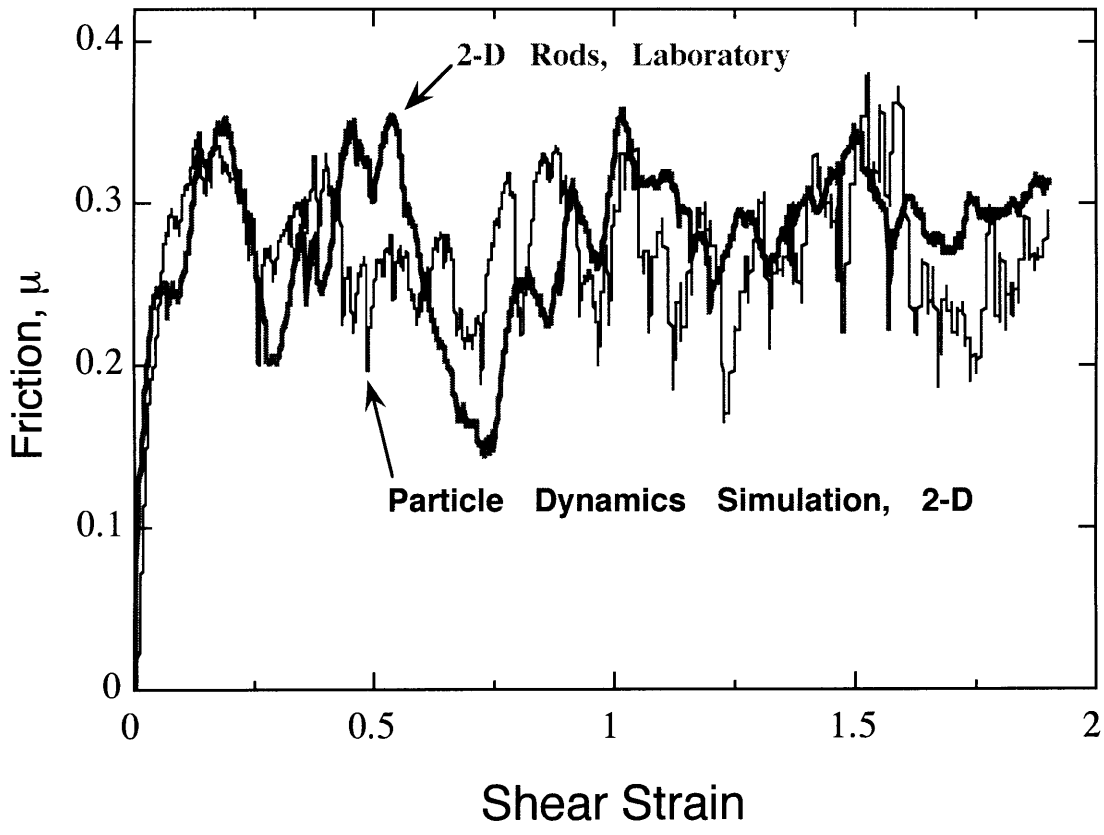

Figure 5.4. Comparison of laboratory data for shear of rods in the 2-D configuration and numerical results for 2-D granular friction. Friction strength and its variation with shear are nearly identical. Simulation results from *Morgan* [1999].

5.4. Discussion and Implications

We observe a linear relationship between particle dimension and the frictional strength of sheared granular layers (Figure 5.3b). This suggests a simple scaling between macroscopic frictional strength and granular degree of freedom.

Our 1-D experiments provide an estimate of interparticle friction of 0.15-0.19, which is consistent with sliding friction for smooth, unlubricated surfaces at low normal stress [*Rabinowicz*, 1995]. We take the low end of this range, $\mu_p = 0.15$, for combined sliding and rolling to account for a reduction in friction due to rolling and because a slight degree of hardening very likely occurs in our experiments due to small amounts of grain fracture during shear. Using this value for μ_p and accounting for interparticle friction on both sets of contact surfaces in 2-D (e.g., surfaces parallel to the shear plane and surfaces perpendicular to the shear direction upon which rolling or sliding must occur to accommodate shear in an extended 2-D assembly) yields an expected average friction value of 0.3, which is quite close to the experimentally measured value of 0.28.

The observed fluctuations in friction for 2-D layers can be explained quantitatively using Equation (5.2) and the measured dilatancy rate. The maximum dilatancy rate averages 0.08 for quartz rods (Figure 5.2) and 0.03 for pasta rods. Therefore, the expected peak friction of 2-D particles is 0.38 for quartz and 0.33 for pasta, which has a contribution of 0.3 from interparticle friction in each case. These values are in good agreement with our experimental measurements, which show maximum friction of 0.37 for quartz rods and 0.31 for pasta rods.

The above reasoning may be extended to 3-D by accounting for interparticle friction on each of the contact planes, including the lateral contacts parallel to the shear direction and

perpendicular to the shear plane. Using the μ_p value of 0.15 yields an expected friction value of 0.45, which is in good agreement with our experimental measurements of 0.45-0.47 (Table 5.1). We posit that for smooth particles, granular friction of 3-D particles exceeds friction of 2-D particles by the amount of interparticle friction on the out-of-plane contacts that do not exist in 2-D.

Data from our 2-D experiments are remarkably similar to numerical results based on 2-D particle dynamic simulations. In both cases, friction fluctuates with a dominant wavelength equal to twice the particle diameter and these fluctuations are much greater than rate/state friction effects (Figure 5.2a). Our data show that discrepancies reported in recent works are due to differences in initial conditions (rough versus smooth particles) and particle dimensionality (2-D versus 3-D granular particles). Although particle fracture is an important effect in granular shear, our data together with the results of *Mair et al.* [2002], who showed that friction of 3-D glass beads increases to the level of angular sand as particles fracture, indicate that the primary strengthening effect of fracture is associated with grain roughness and angularity.

It has been proposed that grain rolling reduces macroscopic frictional strength in numerical models and that this effect may be important in explaining anomalously weak tectonic fault zones [e.g., *Mora and Place*, 1998, 1999]. These numerical studies used 2-D, smooth particles that did not fracture or fractured into smaller particles that were smooth. Our data suggest that the reduced friction found in these studies is a function of particle dimensionality and roughness. Since natural faults are composed of angular, 3-D particles that undergo fracture, we find no evidence for a weakening mechanism associated with the presence of fault gouge.

Our data show that discrepancies between numerical and laboratory results reported in earlier works can be explained by differences in experimental conditions. When the laboratory and numerical experiments are carried out under the same conditions the results are nearly identical.

References for Chapter 5

Aharonov, E., and D. Sparks, Rigidity phase transition in granular packings, *Phys. Rev. E, 60,* 6890-6896, 1999.

Bishop, A.W., Correspondence, *Geotech. 4*, 43-45, 1954.

Geminard, J.-C., W. Losert, and J.P. Gollub, Frictional mechanics of wet granular material, *Phys. Rev. E, 59*, 5881, 1999.

Losert, W, J.-C. Geminard, S. Nasuno, and J.P. Gollub, Mechanisms for slow strengthening in granular materials, *Phys. Rev. E, 61*, 4060, 2000.

Mair, K. and C. Marone, Friction of simulated fault gouge for a wide range of velocities and normal stresses, *J. Geophys. Res.,* 28899-28914, 1999.

Mair, K., K.M. Frye, and C. Marone, Influence of grain characteristics on the friction of granular shear zones, *J. Geophys. Res., in press*, 2002.

Marone, C., Laboratory-derived friction laws and their application to seismic faulting, *Annu. Rev. Earth Planet. Sci., 26,* 643-696, 1998.

Marone, C., C.B. Raleigh and C.H. Scholz, Frictional behavior and constitutive modeling of simulated fault gouge, *J. Geophys. Res. 95*, 7007-7025, 1990.

Mead, W.J., The geologic role of dilatancy, *J. Geol. 33*, 685-698, 1925.

Mora, P., and D. Place, The weakness of earthquake faults, *Geophys. Res. Lett., 26,* 123-126, 1999.

Mora, P., and D. Place, Numerical simulation of earthquake faults with gouge: toward a comprehensive explanation for the heat flow paradox, *J. Geophys. Res., 103,* 21067-21089, 1998.

Morgan, J.K., Numerical simulations of granular shear zones using the distinct element method: I Shear zone kinematics and the micromechanics of localization, *J. Geophys. Res., 104,* 2703-2719, 1999.

Morgan, J.K., and M.S. Boettcher, Numerical simulations of granular shear zones using the distinct element method: II Effects of particle size distribution and interparticle friction on mechanical behavior, *J. Geophys. Res., 104,* 2721-2732, 1999.

Rabinowicz E., *Friction and wear of materials*, John Wiley & Sons, pp. 315, 1995.

Sammis, C.G., G. King, and R. Biegel, The kinematics of gouge deformation, *Pure Appl. Geophys., 125*, 777-812, 1987.

Sammis, C.G., R.H. Osborne, J.L. Anderson, M. Banerdt and P. White, Self-similar cataclasis in the formation of fault gouge, *Pure Appl. Geophys., 124*, 51-77, 1986.

Table 5.1.

Experiment	Type	Material	Particle size, μm	σ_n, MPa	μ_{ss} avg. (± 1 std. dev.)
m290	3-D	Ottawa sand	50-150	5	0.63
m302	3-D	Ottawa sand	50-150	5	0.63
m490	3-D	Ottawa sand	50-150	40	0.58
m429	3-D	Glass beads	105-149	25	0.44 w/stress drops
m349	3-D	Glass beads	105-149	5	0.47 w/stress drops
m444	3-D	Glass beads	1-800	5	0.45
m445	3-D	Glass beads	1-800	5	0.45
m446	3-D	Glass beads	1-800	5	0.46
m518	2-D	Qtz. glass rods	1000	1	0.27 (±0.11)
m473	2-D	Pasta rods	1000	1	0.28 (±0.03)
m524	1-D	Qtz. glass rods	1000	1	0.16
m525	1-D	Qtz. glass rods	1000	1	0.19
m474	1-D	Pasta rods	1000	1	0.14

Appendix A: The layer thickness parameter alpha and humidity

Velocity stepping tests were performed (e.g. section 2.3.4) to determine the friction velocity dependence for quartz powder and alumina powder. Changes in friction in response to imposed velocity changes are accompanied by changes in dilatancy rate in the layer thickness data (Figure A.1). The layer thickness changes can be parameterized as α:

$$\alpha = \frac{dh}{d\log V}, \tag{A.1}$$

where h is layer thickness and V is velocity.

α is interpreted as an indication of shear band width [*Marone and Kilgore*, 1993]. For quartz powders over the relative humidity (RH) range of 5-100%, little variation is seen in α, suggesting that the development of shear localization is independent of humidity (Figure A.2a). For tests with alumina powder, the low RH test (5%) has a significantly higher α value than that measured at higher RH (Figure A.2b). This data point may indicate that some coupling may occur between chemically assisted contact junction mechanisms and the development of microstructure.

Reference for appendix A:

Marone, C., and B.D. Kilgore, Scaling of the critical slip distance for seismic faulting with shear strain in fault zones, *Nature*, *362*, 618-621, 1993.

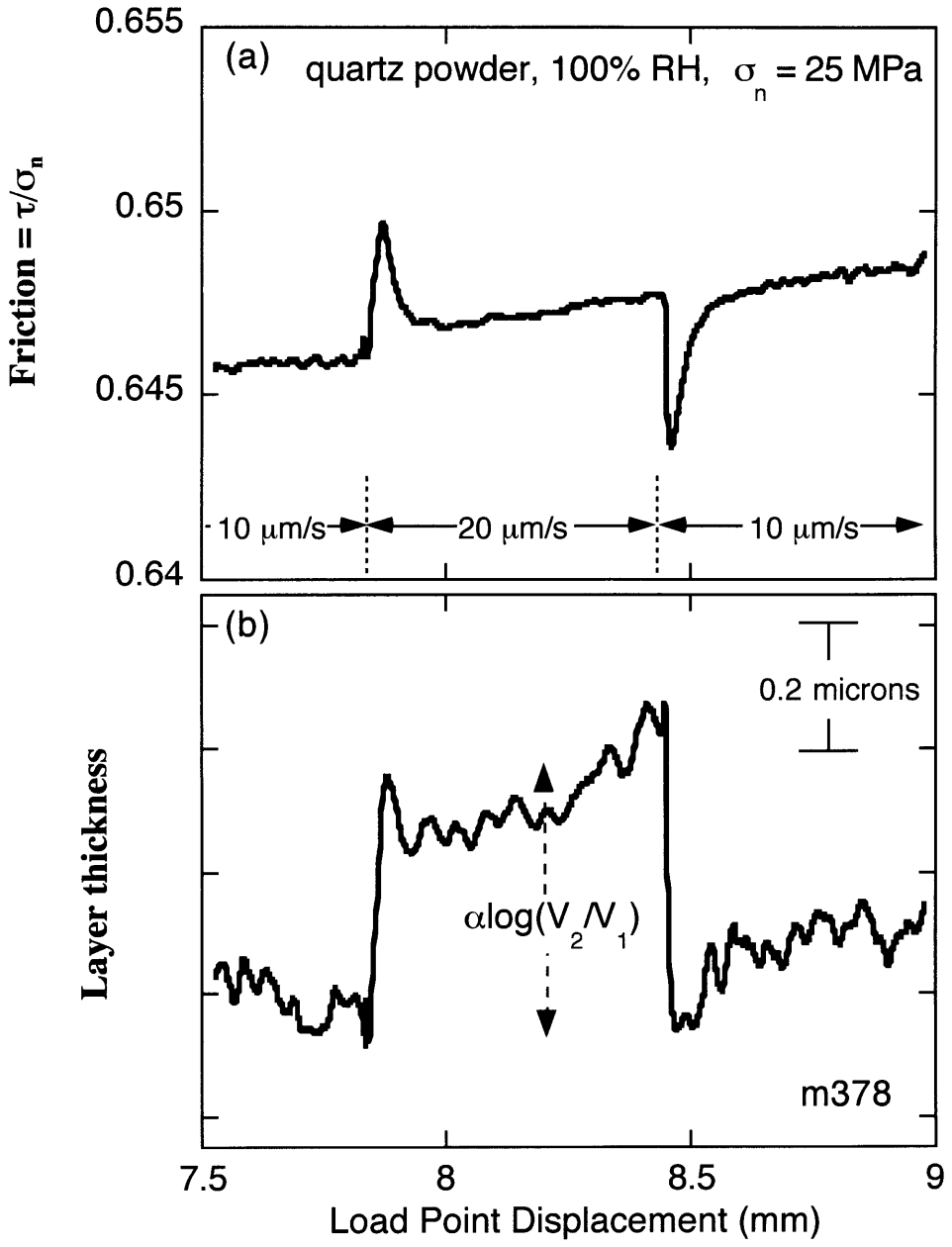

Figure A.1. (a) Friction data from a quartz powder, 100% RH test showing a series of velocity steps. The corresponding layer thickness data, detrended to remove an overall thinning trend, demonstrate layer dilation corresponding with velocity change (b). The layer thickness change associated with velocity steps may be parameterized by α as shown.

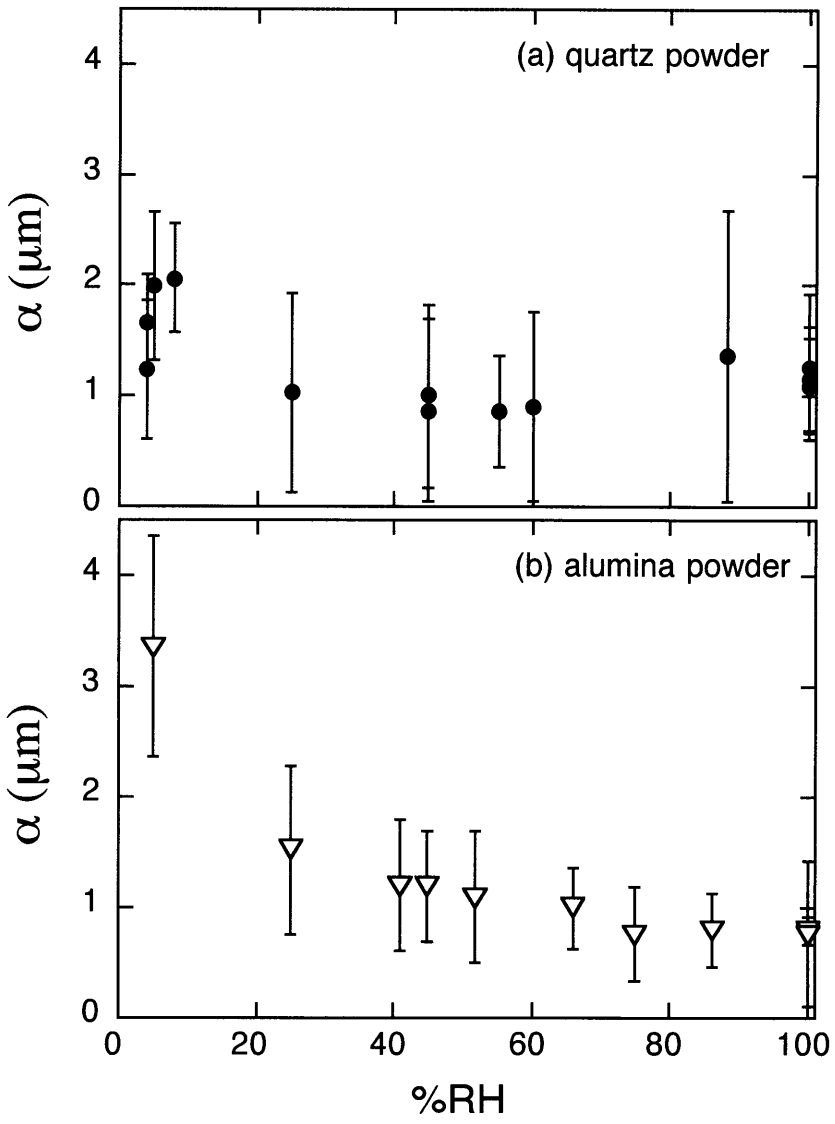

Figure A.2. The layer thickness change α associated with a change in velocity from 10 to 20 μm/s for quartz powder (a) and alumina powder (b). Variation of α with RH is within the scatter (2σ error bars shown) with the exception of the low RH alumina powder test.

Appendix B: Additional photographs and micrographs of sample material

For comparison to the micrographs of undeformed quartz powder and glass beads (Figure 4.2), I include a photograph of the glass rods (Figure B.1) used for 2D experiments (chapter 5) and micrographs of undeformed (Figure B.2) and deformed Westerly granite powder (Figure B.3).

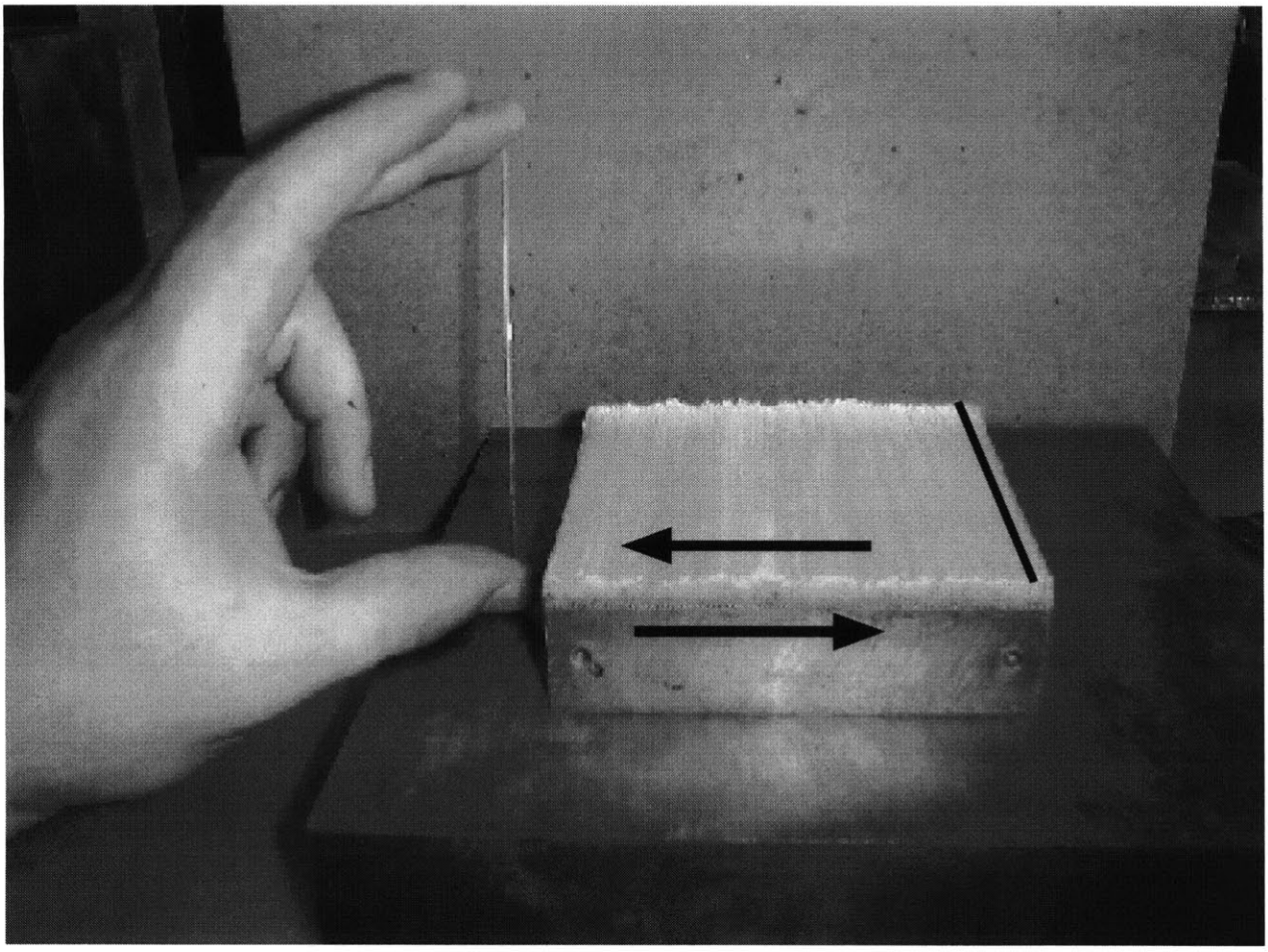

Figure B.1. 1 mm diameter glass rods of 100 mm length. This sample is in the 2D configuration and produced the data shown in Figure 5.2. The sense of shear is indicated by the arrows and the black line indicates rod orientation on the sample block.

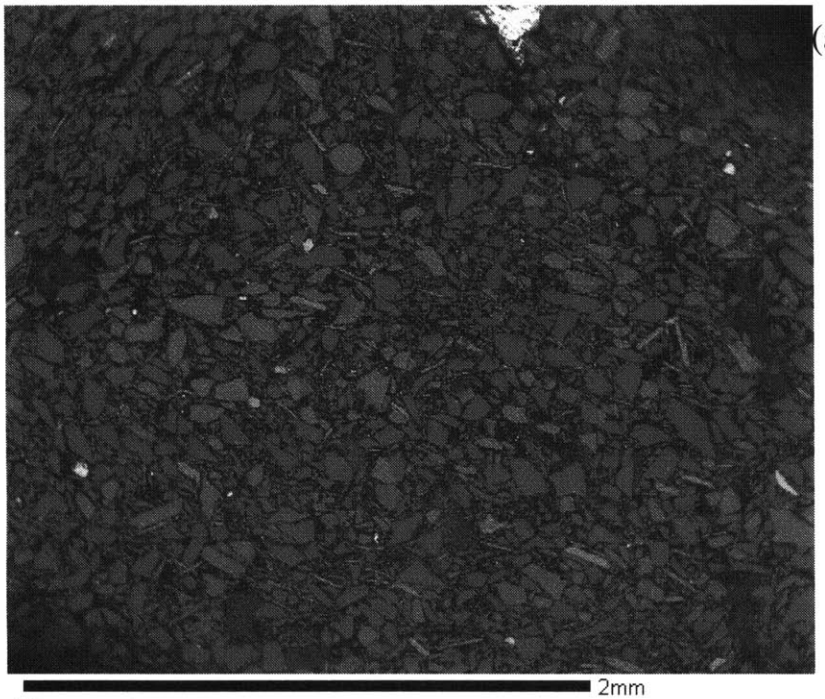

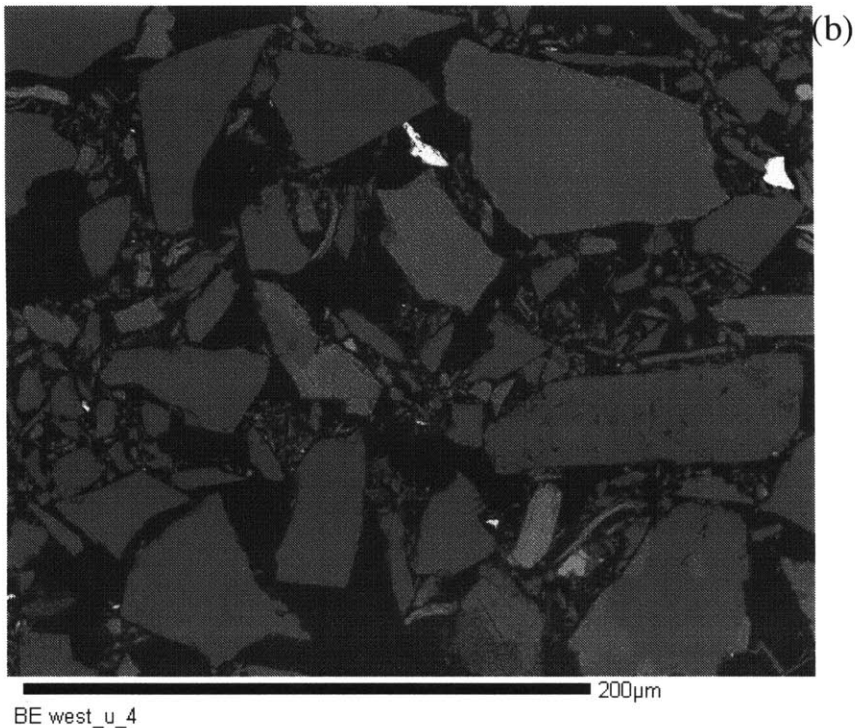

Figure B.2. Undeformed Westerly granite powder at 40x (a) and 400x (b) magnification. Grains are angular and average grain size is smaller than that of the Ottawa (quartz) sand (Figure 4.2).

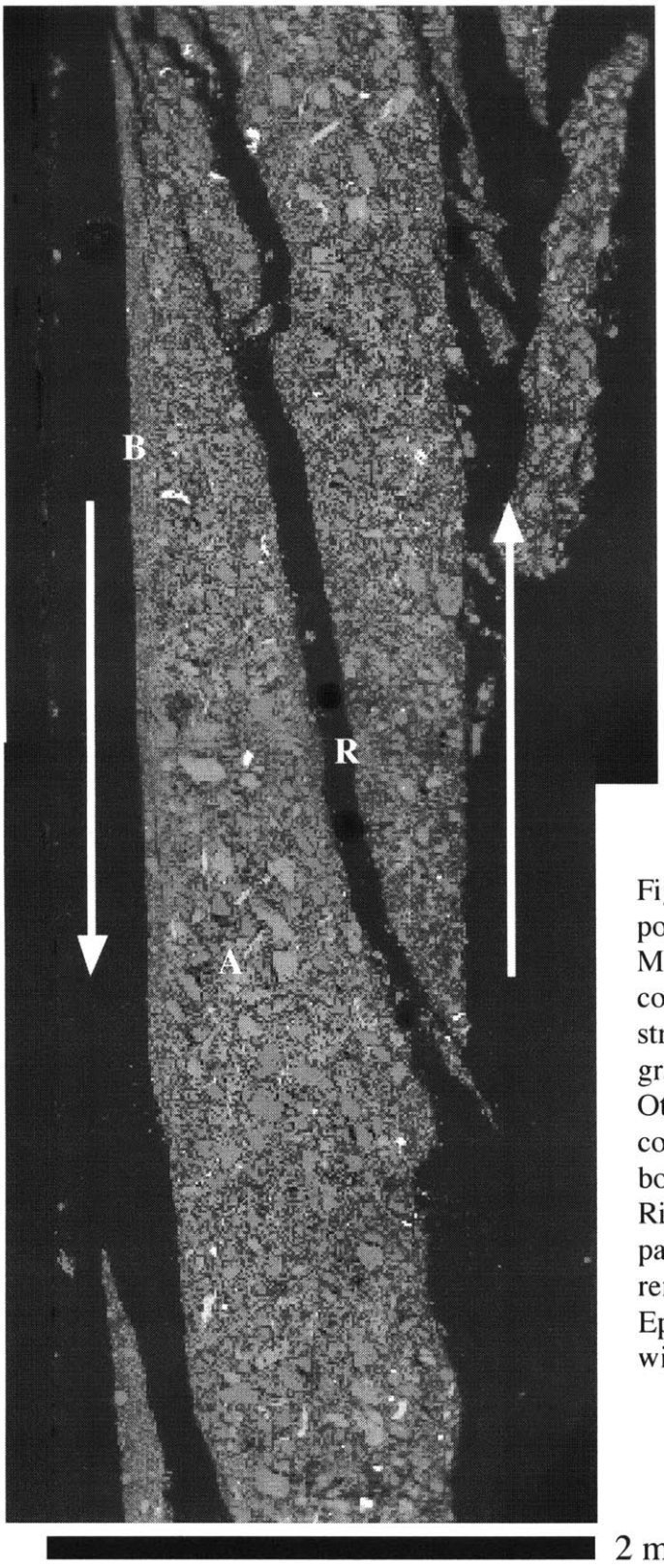

Figure B.3. Westerly granite powder sheared for 10 mm at 25 MPa normal stress after pre-conditioning at 40 MPa normal stress. Although initial mean grain size is smaller than that of Ottawa sand, significant comminution occurs in boundary shear zones (B) and Riedel shear zones (R), while particles in other areas (A) remain relatively undisturbed. Epoxy filled cracks correspond with Riedel shear fabric.